POLITECNICO DI MILANO

School of industrial and information engineering
Department of Chemistry, Materials and Chemical engineering "Giulio Natta"

Master of Science in Materials Engineering and Nanotechnology

PO LI TE CNICO

MILANO 1863

TOMSK POLYTECHNIC UNIVERSITY

Cr coatings deposited by electroplating and magnetron sputtering onto Zr-1Nb alloys for nuclear reactor claddings for protection against high-temperature corrosion.

Supervisor: Prof. Massimiliano Bestetti

Co-supervisor: Prof. Dmitrii Vladimirovich Sidelev

Master Thesis Candidate:

Cristiano Poltronieri   ID. 917706

Academic Year 2019/2020

TABLE OF CONTENTS

LIST OF FIGURES

11

14

LIST OF TABLES

RIASSUNTO

La crescita della domanda di elettricità e del tasso di consumo di combustibili fossili, con la necessità di gestione di gas serra, portano ad una richiesta di generazione di elettricità più sostenibile dal punto di vista ambientale. L'energia nucleare è un'alternativa ai combustibili fossili.

I materiali nel nocciolo del reattore sono esposti a un ambiente aggressivo a causa di campi termo-meccanici e di radiazione e refrigerante chimicamente aggressivo. I rivestimenti del combustibile nucleare sono uno dei componenti più importanti per l'integrità e la sicurezza del combustibile. L'uso di leghe di Zr per i claddings è dovuto alla loro sezione trasversale a basso assorbimento di neutroni termici, a ragionevoli prestazioni di corrosione durante il normale funzionamento e buone proprietà meccaniche sotto irradiazione di neutroni.

I rivestimenti in leghe di Zr soffrono grave corrosione se esposti a vapore ad alta temperatura. Questo è un problema molto importante, che influisce sulla sicurezza di una centrale nucleare. Le possibili soluzioni potrebbero essere la modifica del combustibile, l'utilizzo di rivestimenti protettivi sui claddings in lega di Zr o la loro realizzazione in materiali diversi.

I claddings rivestiti sono l'alternativa più promettente, in quanto potrebbero essere una soluzione a breve termine poiché non è necessario alcun arricchimento del combustibile. Potrebbero migliorare le prestazioni di un impianto, in caso di incidente che in condizioni normali. Questa soluzione potrebbe aumentare l'efficienza delle centrali nucleari, rendendole più competitive nel campo della produzione di energia elettrica.

In questo lavoro verrà analizzata la capacità di protezione di rivestimenti in Cr su Zr-1Nb, depositati per elettrodeposizione e magnetron sputtering. Verrà esaminata l'influenza dello spessore di Cr. Verranno effettuati test di ossidazione (in atmosfera e LOCA) e i campioni saranno analizzati mediante XRD, SEM, microscopia ottica e GDOES per verificare la struttura cristallografica, microstruttura e profilo elementare. Inoltre, saranno effettuati test gravimetrici per valutare la protezione dall'ossidazione del Cr depositato.

ABSTRACT

The growth in electricity demand and in the consumption rate of fossil fuels, together with the need of managing atmospheric greenhouse gas emissions, drive for a more environmentally sustainable electricity generation. Nuclear energy is an alternative to fossil fuels.

The materials in the reactor core are exposed to an aggressive environment, due to thermo-mechanical and radiation fields, and chemically aggressive coolant. Nuclear fuel claddings are one of the most important components for fuel integrity and safety. The use of Zr alloys as fuel claddings is due to their low thermal neutron absorption cross-section, reasonable corrosion performance under normal operation, and good mechanical properties under neutron irradiation.

Zr alloys claddings are subjected to severe corrosion if exposed to high-temperature steam. This is a very important problem, which strongly affects the safety of a nuclear plant. Possible solutions could come by modifying the fuel (microencapsulated in a non-fissionable ceramic matrix), by using either protective coatings on Zr alloy claddings, or claddings made in different materials (such as FeCrAl or SiC).

The coated claddings are the most promising alternative as they could be a short-term solution since no fuel enrichment is needed (like for ferrous claddings). They could improve the performance of a plant, under accident and normal conditions. This technical solution could increase the efficiency of nuclear plants, making them more competitive in the field of production of electrical energy.

Protection capability of Cr coatings onto Zr-1Nb, deposited by electroplating and magnetron sputtering, will be analyzed in this work. The influence of the thickness of Cr coatings will be examined. Oxidation tests (in atmosphere and LOCA condition) will be carried out and the samples will be analyzed by XRD, SEM, optical microscopy and GDOES to check the crystallographic structure, the microstructure and elemental depth profile of the coatings. Moreover, gravimetric tests will be done to evaluate the oxidation protection of the deposited Cr.

INTRODUCTION

Electricity is a primary need in the modern world and the current development of society depends on its production. The conventional fossil fuels, renewable sources and nuclear are the principal ways to produce electrical energy. Fossil fuels are the most dominant: the coal is the most used as source of energy, it represents the 38% of the world electricity generation in 2017. Natural gas remains second as it is used 23.2%. Hydroelectricity is another important source for production of electricity (15.9%) [1].

Nuclear energy was the 11% of the world electricity generated in 2017 and, currently, there are 450 nuclear reactors in operation in 30 countries around the world. The nuclear power plant market was sized at around 30 billion US dollars in 2011 and is expected to exceed 50 billion US dollars by 2030. In 2018, 362 GW have been produced, while in 2050, global nuclear power capacity is predicted to reach 516 GW [2].

The main public concern regarding nuclear energy is "safety": well-known nuclear accidents are Chernobyl (USSR, 1986) and Three Mile Island (USA, 1979). These accidents helped the nuclear industry to build safer nuclear plants and to organize suitable emergency procedures in case of accident [3].

A severe nuclear accident occurred in March 2011 at the Fukushima Daiichi Nuclear Power Plant (Japan): a great earthquake of magnitude 9.0 with a subsequent 15 m tsunami seriously damaged the reactors and disabled the emergency power supply, leading to the loss of active coolant from the primary circuit. This caused a rapid temperature increase in the core and converted the coolant water from liquid into steam. Zr-based alloy claddings underwent severe degradation due to the rapid reaction with high-temperature steam accompanied by the generation of a large amount of heat and hydrogen.

$$Zr + 2H_2O(g) \rightarrow ZrO_2 + 2H_2(g) \qquad \Delta H^0 = -584.5 \text{ kJ/mol (1200°C) [1]}$$

The heat from Zr oxidation accelerated the rise of the temperature and the meltdown of the core. The hydrogen gas damaged the containment buildings through detonations, with the release of highly radioactive fission products into the environment [4].

The events that followed at the Fukushima accident led to a global interest in the research on claddings with enhanced performance during accidents. Accident-tolerant fuel (ATF) development programs were started in many research institutions and industrial companies worldwide.

Also during normal operation, in Pressurized Water Reactors (PWRs) and Boiling Water Reactors (BWRs), the temperatures (in PWRs and BWRs are approximately 330°C and 288°C, respectively) cause Zr corrosion and the associated hydrogen evolution, but careful design of the cladding alloy could minimize these phenomena.

An additional concern, associated with Zr-based alloys in normal operations, is absorption of hydrogen produced both by the cladding corrosion and the radiolysis of the water. Hydrogen ions can penetrate the oxide scale and dissolve in the metallic matrix, precipitating as brittle hydrides (ZrH_x), leading to the reduction of ductility and toughness of the cladding tube. This effect can significantly reduce the cladding performance during accident circumstances [5].

By improving the fuel or the cladding material, or by developing a coating for the claddings, the risk of releasing radioactive material in case of accident could be controlled.

The main accidents in a nuclear reactor are reactivity-initiated accident (RIA), loss-of-coolant accident (LOCA) and station blackout (SBO):

- Reactivity Initiated Accident (RIA): the fast removal of control rods or blades from the core increases rapidly the power generation in the nearby fuel rods. This causes a thermal expansion of pellets which can touch and strain the cladding material. This pellet-cladding mechanical interaction can cause the cladding failure and expulsion of the fuel that can damage the reactor vessel.

21

- Loss of Coolant Accident (LOCA): significant loss of coolant in the core. Ballooning and burst of fuel rods are observed at 800-1000°C, and during the high temperature exothermic oxidation of Zr with steam, the core can reach temperature up to 1200°C.
- Station Blackout (SBO): loss of offsite power, failure of the redundant emergency generators, the eventual degradation of the reactor coolant pump (RCP) resulting in a long-term loss of coolant.
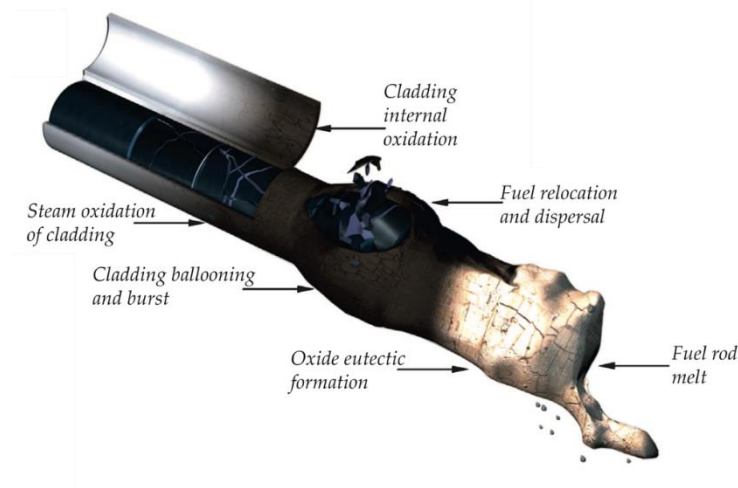
Figure 1. Evolution of a fuel rod under LOCA and SBO conditions [6].

Researchers are investigating several possibilities to make the nuclear reactors safer in case of accident. The main solutions considered are design of new accident-tolerant nuclear fuel, new claddings materials or coating on Zr-based alloy claddings.

Accident-tolerant nuclear fuel

The new fuels, which must be optimized, are already in testing phase. Nowadays, 98 nuclear plants in USA are working with pressed uranium in cylindrical pellet shape [7], each one with 12 mm diameter and 20 mm long. The pellets are stacked in long fuel rods in Zr alloy (**Figure 2**) that are immersed in water.
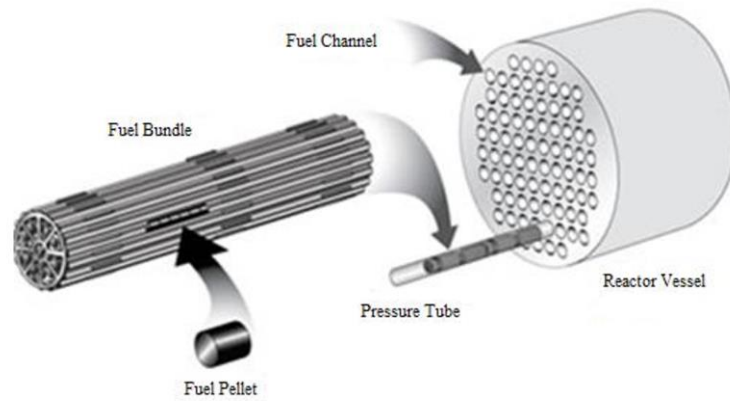
Figure 2. Schematic drawing of a reactor fuel assembly [8].

During the fission, the released neutrons go through the claddings and enter in other fuel rods, triggering a chain reaction able to generate heat. In the second or outer heat exchanger, the heat generated converts water in steam, which is used to create electricity (**Figure 3**).
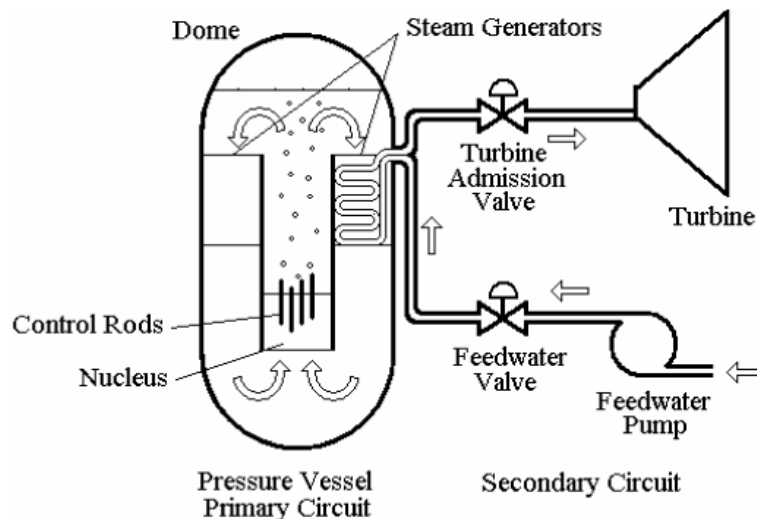
Figure 3. Schematic drawing of nuclear primary and secondary cooling circuit [9].

Some alternative fuel forms, different from uranium oxide pellets, could provide improved accident performance by improving fission product retention. For example, by controlling the heat capacity of the fuel is possible to affect the accident progression for short term accidents. Alternative fuel systems are characterized either by high density and high thermal conductivity (e.g., containing high thermal conductivity second phases) or by encapsulating the fuel in a ceramic non-fissile matrix

23

(FCM), which allows the retention of fission products. Issues are fabrication cost, study of new reactor physics design, optimized fuel enrichment level, irradiation behavior, and investigation of behavior under LOCA and RIA scenarios. The relative lack of practical operating experience with alternative fuel forms compared to monolithic UO_2-based ceramic fuel is also a limit to their development [6].

Claddings alternative to Zr alloys

A variety of materials are being considered as alternatives to Zr alloy cladding, including oxidation-resistant structural alloys (FeCrAl), silicon carbide fiber-reinforced SiC ceramic composites, and refractory alloys. In all cases, the main desired attributes are the resistance to high temperature oxidation and temperature strength.

As a ceramic, SiC has been identified as a potential candidate material to replace Zr-based alloys since it has an higher melting temperature, reduced hydrogen generation under accident conditions, low chemical activity, lower neutron absorption cross-section, mechanical strength up to very high temperatures, good radiation resistance and good corrosion resistance up to temperatures of 1600°C [10]. To overcome the brittle behavior, SiC fiber-reinforced SiC matrix (SiC_f/SiC_m) composites were developed with multiple industrial processes [10].

In spite of the potential benefits of SiC-based cladding, there are a lot of technical issues, such as the fabrication technique of thin wall long tubes, corrosion under the normal operating condition and the hermetic joining seals [10]. These issues are due to the lack of engineering familiarity in design and application. Other issues specific to claddings application include: production of tubing geometries with low cost process, development of robust joining methods, demonstration of hermetic retention of fission products, development of standards, investigation of pellet-cladding mechanical interaction under RIA conditions [6].

However, the brittleness is one of the main obstacles preventing the application of SiC as cladding material: the accumulated stresses during the mechanical interaction (PCMI) cannot be dissipated through the plastic deformation and creep.

The oxidation reaction of the Si and SiC are as follows:

$$Si + 2H_2O \rightarrow SiO_2 + 2H_2\uparrow$$

$$SiC + 2H_2O \rightarrow SiO_2 + CH_4\uparrow$$
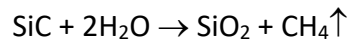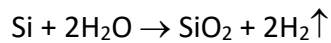
At high-temperature and high-pressure water, the SiO_2 layer is unstable and it dissolves into water through the following reaction:

$$SiO_2 + 2H_2O \rightarrow Si(OH)_4 \ (aq)$$
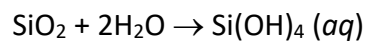
These aspects hinder the development of SiC-based cladding. Additionally, the manufacturing costs, the modification of the cooling system, the high costs and the long time needed to develop such materials are impeding the change from Zr to SiC cladding for LWR.

Another candidate for non-Zr claddings are iron alloys. Austenitic stainless steels (AISI 304, 316, and 347) have been used as cladding materials in BWRs, eventually replaced with Zr due to the stress corrosion cracking (SCC) failure. The alloys capable of forming protective chromia, alumina, or silica are promising. To form protective chromia films, a Cr content greater than 22% wt. is necessary in ferritic steels. For austenitic alloys, similar Cr contents must be accompanied by high Ni additions to preserve the FCC structure. Such materials have a cross-section for thermal neutron ten times higher than that of Zr. Another issue is the hydrogen embrittlement of the ferrous cladding because of the precipitation that occurs after irradiation at 300-400°C (typical for LWR). To avoid the precipitation of hydrides, FeCrAl (13 wt% Cr, 4 wt% Al) alloys were evaluated for this application. However, these alloys are resistant to air oxidation, while they have poor resistance to high temperature steam. Furthermore, the effects of alloy composition on its melting point and oxidation resistance have been examined. Strength and ductility of FeCrAl alloys can be tuned by the alloy composition and the microstructure. Corrosion behavior of these alloys in LWR environments has been examined, and corrosion resistance by forming Cr oxides has been proved. The main drawback is the high neutron absorption cross section of Fe and Cr, which results in 4-6 times higher than the Zr. To compensate this absorption, the pellet enrichment may be increased, or cladding thickness reduced

and pellet diameter extended. In both cases, this is accompanied by a 15-25% of extra costs for fuel [11].

Table 1. Price estimate in k US $ for a PWR fuel bundle with various cladding materials [11].

	Cladding	Fuel pellet	Fabrication	Total	Δ base case (%)
Zr-based (base case)	30	950	140	1120	-
Coated Cr Zr-based	<40	950	140	<1130	<1
FeCrAl cladding	<30	1140	140	<1310	<17
SiC/SiC cladding	>300	950	140	>1390	>24

Coated Zr claddings

The major benefits of coating Zr-based claddings are the economics and the fact that the resistance can be improved without the necessity to modify the base materials, contributing to the possibility for commercial application in the short-term (five years or less).

The coating for Zr claddings concept for ATF seems to be more promising than the alternatives described above. A thin metallic coating has a negligible impact on heat transfer from the fuel to the coolant. If the tube wall thickness of the current Zr-based alloy cladding is between 0.6 and 0.8 mm, the coating will add only 10-μm thickness. Basically, for neutronic calculations and structural considerations, the coated Zr concept is highly similar to the original configuration [12].

Additionally, coated Zr-based alloys are characterized by superior properties as higher melting point and lower hydrogen absorption, thereby mitigating severe accident consequences. Another advantage is to decrease the operating costs (which are the greatest part of a nuclear plant expenses) by using safer and more stable materials for longer time than the traditional ones (**Figure 4**).

The rates of hydrogen generation in the reactor core during LOCA conditions are dominated by oxidation of the Zr-based alloy components. Therefore, the reduction of the high temperature oxidation rate of Zr would provide benefits in terms of improved accident tolerance.

Pronounced improvement in the oxidation resistance of Zr-based alloys at normal operating conditions (300°C) would be achieved. This could decrease the operating costs and, consequently, it may decrease the total cost of an operating nuclear plant (**Figure 4**).
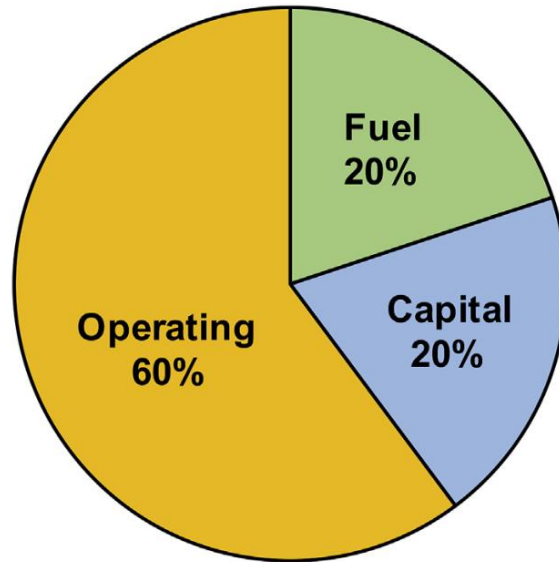
Figure 4. Fuel, operating, and capital costs of a nuclear plant per produced kWh [11].

To enhance the accident resistance of coated Zr-based claddings, some reasonable requirements are desired. The major requirements and challenges which a protective coating must face are:

- capability to coat full-length cladding tube with desired microstructure and acceptable costs;
- fabrication temperature below 500°C to avoid the Zr alloy microstructure changes;
- negligible negative effect on neutron balance (scattering, absorption);
- high thermal conductivity, thermal expansion coefficients of coating comparable to that of Zr, and high melting temperature;
- good corrosion and irradiation resistance in normal operations (extend fuel cycles);
- good mechanical properties involving adhesion, wear, fracture, spallation, and fretting resistance;
- good adhesion and ductility to sustain high deformations of Zr cladding in case of ballooning during accidental conditions;
- improved resistance in high temperature steam or air environment in accident conditions;

- slowing the reaction kinetics with steam to decrease the heat of reaction, reduce the generation of hydrogen, and reduce hydrogen embrittlement;
- improving cladding properties including shock and fracture resistance, and reducing the interactions between the fuel and the cladding walls;
- enhancing gaseous and solid fission products retention.

Moreover, the coating must support the compression from reactor pressurization. Differential volumetric and microstructural evolution between the coating and the cladding can lead to coating spalling. In addition to oxidation resistance, it would be desirable for the Zr cladding to exhibit improved properties in creep behavior, in order to retard ballooning and failure of the cladding during LOCA or SBO scenarios, and also to improve resistance to pellet-cladding mechanical interaction associated with RIA scenarios. The improved high temperature strength would also be beneficial for minimizing spalling of coatings during high temperature excursions [6].

Potential approaches to reduce the oxidation rate include application of self-passivating coatings, these materials that can exhibit high temperature steam oxidation resistance are chromia, alumina, and/or silica formers. Therefore, any ATF coating needs to contain at least one of the elements Cr, Al, or Si.

In particular, the most widely explored coating technologies on Zr-based alloys are the ones that form chromia. Specifically, metallic Cr, CrAl, and CrN coatings have been studied. Excellent stability of a thin (<5 μm) CrN coating on the surface of Zr cladding was demonstrated [1].

Other coatings, like Ti_2AlC, TiAlN, Ti_3SiC_2, and Cr_2AlC that form alumina or silica, have been investigated (**Figure 5**).
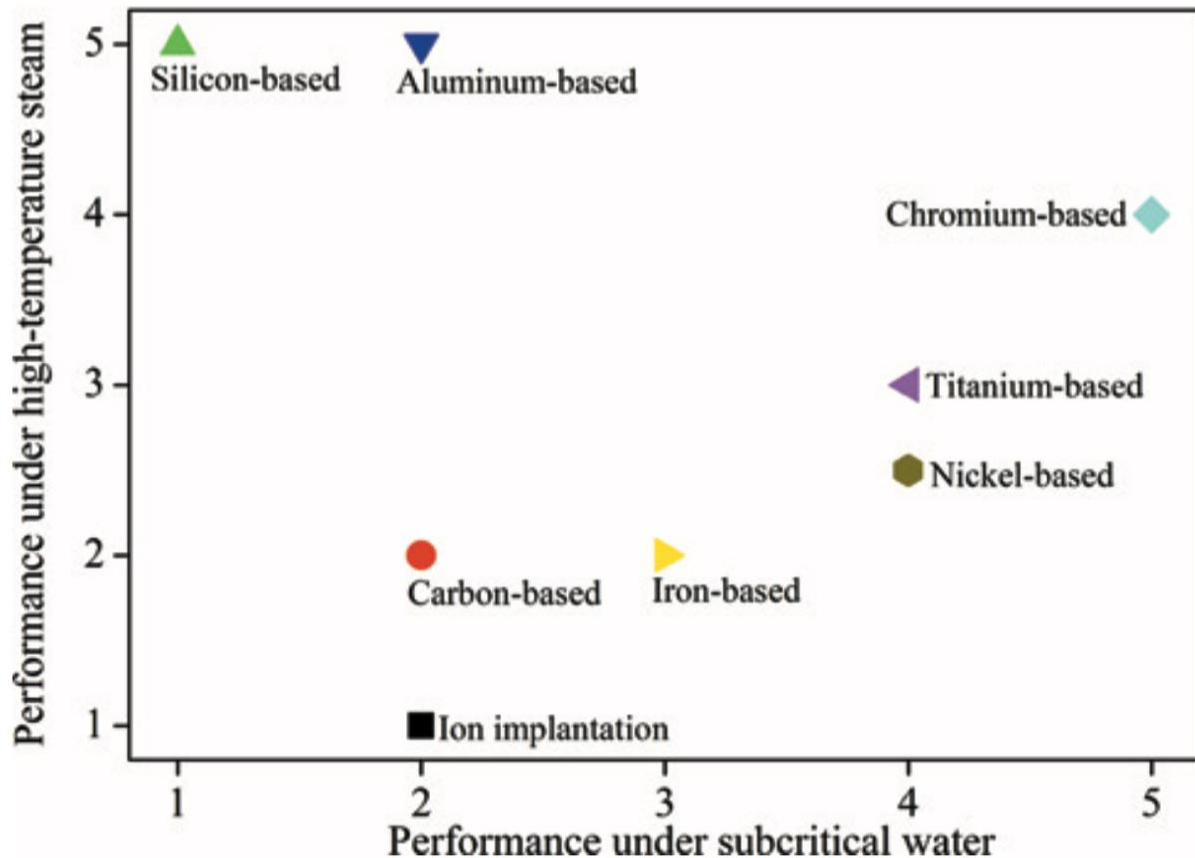
Figure 5. Performance of coatings on Zr claddings in normal and accident conditions (1 worst, 5 best) [1].

This analysis suggests that Cr-based coatings perform excellently under both normal and corrosion conditions due to the growth of a protective Cr_2O_3 layer. The Cr_2O_3 layer acts as an efficient oxidant diffusion barrier during corrosion tests, it lowers by one order of magnitude the weight gain rate in corrosion experiments. It is marked as the highest grade during hot-water corrosion (**Figure 5**). However, one limitation is that the top temperature stability of Cr_2O_3 in steam is approximately 1200°C because of its eutectic point in Zr-Cr phase diagram (**Figure 10**).

Cr coating will not negatively impact the mechanical behavior of the Zr cladding and the neutronic balance impact will be minimal. The use of Cr coating is designed to provide short-term additional protection to the cladding at temperatures up to 1100°C [1]. The presence of Cr_2O_3 on the surface of the cladding coating prevents not only oxygen access but also hydrogen diffusion into the Zr substrate [12].

Metallic Cr attracted much attention due to its high melting point, high temperature oxidation resistance, similar thermal expansion coefficient of Zr and low thermal neutron absorption cross section.

In the case of a Cr coating with a thickness of 10 μm, the resulting chromia that forms under high temperature conditions protects the metallic Zr.

Furthermore, reduced cladding ballooning during LOCA testing and resistance to cladding post-quench ductility loss have been reported for Cr coatings [11].

The Cr-based coatings exhibited the most promising behavior: good compromise between oxidation resistance and adhesion to the metallic substrate, good fretting resistance and improved resistance to oxidation in steam at high temperature. Corrosion tests performed at 360°C in pressurized water (normal conditions) illustrates the rates of weight gain (**Figure 6A**).

A poor oxidation behavior is observed for most of the ceramic (nitrides) coatings [13]. One additional motivation for choosing a fully metallic-based coating is its intrinsic ductility compared to ceramic at high temperature. Indeed, in LOCA conditions, the cladding may experience significant strain (ballooning) due to the internal clad pressure. Internal pressure tests have been conducted on CrN-coated Zr claddings. They have shown that the ceramic coating did not sustain the clad circumferential elongation, inducing a high surface density of open cracks. Scratch test evidenced no coating delamination or spallation, thus indicating a good Cr- Zr bonding. The thin Cr coating has not significant impact the overall mechanical properties of the cladding in nominal conditions. This is not the case for higher temperatures typical of LOCA conditions at which a strengthening effect of the Cr coating is observed.
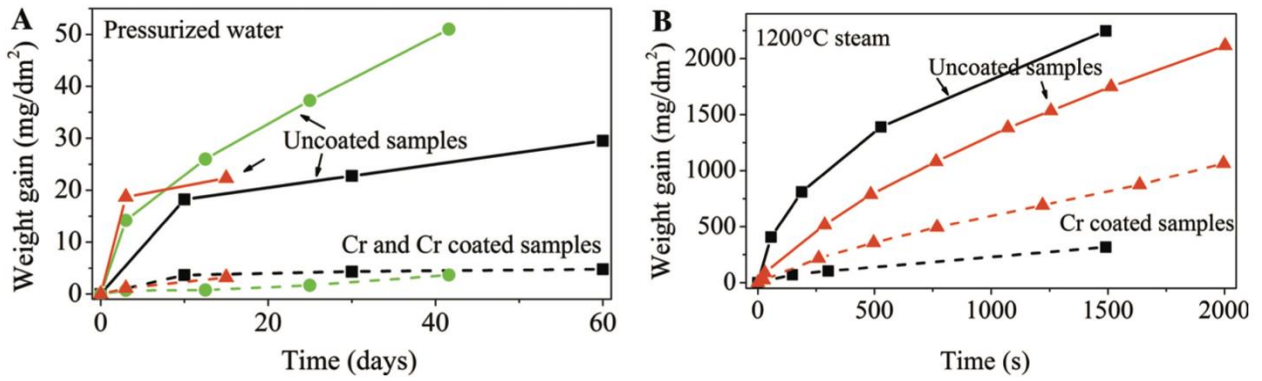
Figure 6. Corrosion rate in pressurized water simulating PWR (A) and high temperature steam oxidation rate under LOCA conditions (B) of uncoated Zr-based alloys and Cr-coated (■ PVD; ▲ Cold Spray; ● Arc evaporation) [1].

Cr-coated Zr claddings were tested in steam at 415°C at 100 bar for 200-250 days [14]. It has been observed that:

- The outer surface color of the coated materials evolves from gold to magenta/deep blue. Such colors are linked to the growth of the thin chromia layer. For not fully protective Cr-coatings, grey spots are observed. This is likely due to the local formation of ZrO_2 islands.

- The Cr-coating is clearly protective with very low weight gain values: less than 5 mg/dm^2 after 200 days in autoclave testing under steam at 415°C at 100 bar, while it is more than 260 mg/dm^2 for the uncoated Zr alloy in the same conditions [14]. Such behavior must be confirmed also under neutron irradiation.
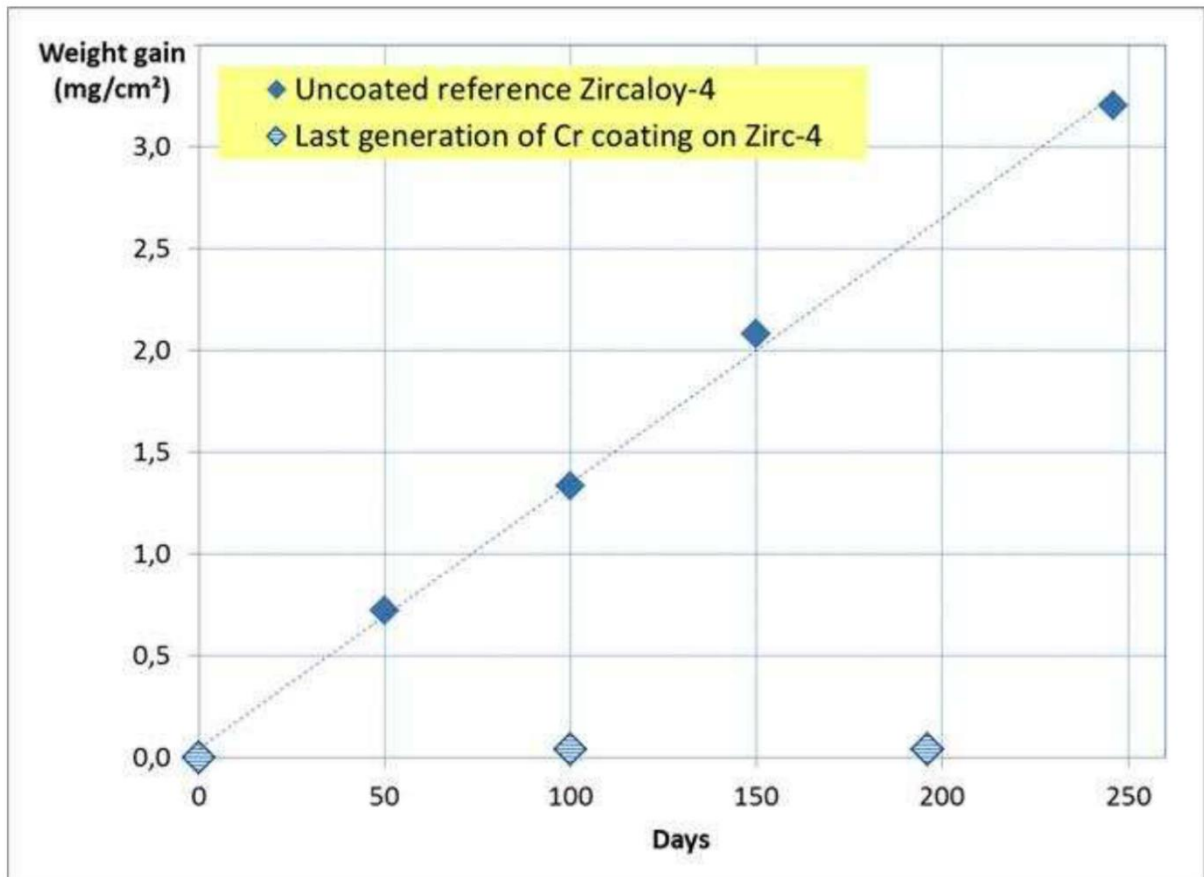
Figure 7. Weight gain of uncoated and Cr-coated materials after autoclave tests at 415°C, under 100 bar steam environment [14].

Hydrogen analyses were carried out on Cr coated samples and compared with the uncoated Zr. The measured hydrogen content was around 1000 ppm after 200 days for uncoated Zr, while for the Cr-coated samples the hydrogen contents reached from 25 to 150 ppm. In tests at 1000-1200°C in steam, 5-10 μm Cr coatings were enough to lead to decrease the weight gain by ten times compared to the uncoated sample.

This result suggests that Cr-coated Zr claddings would be an efficient mitigation solution against hydriding and in-service corrosion.

Pre-existing defect in Cr coating can be an issue as shown in **Figure 8**, where the effects of a cracks in the coating and the subsequent oxidation in both nominal and high temperature steam conditions are represented. The images show that a pre-existing crack has only a limited and very localized

impact on the overall oxidation of the coated sample. Moreover, there is no experimental evidence of any spallation of the Cr or corrosion acceleration of the Zr substrate.
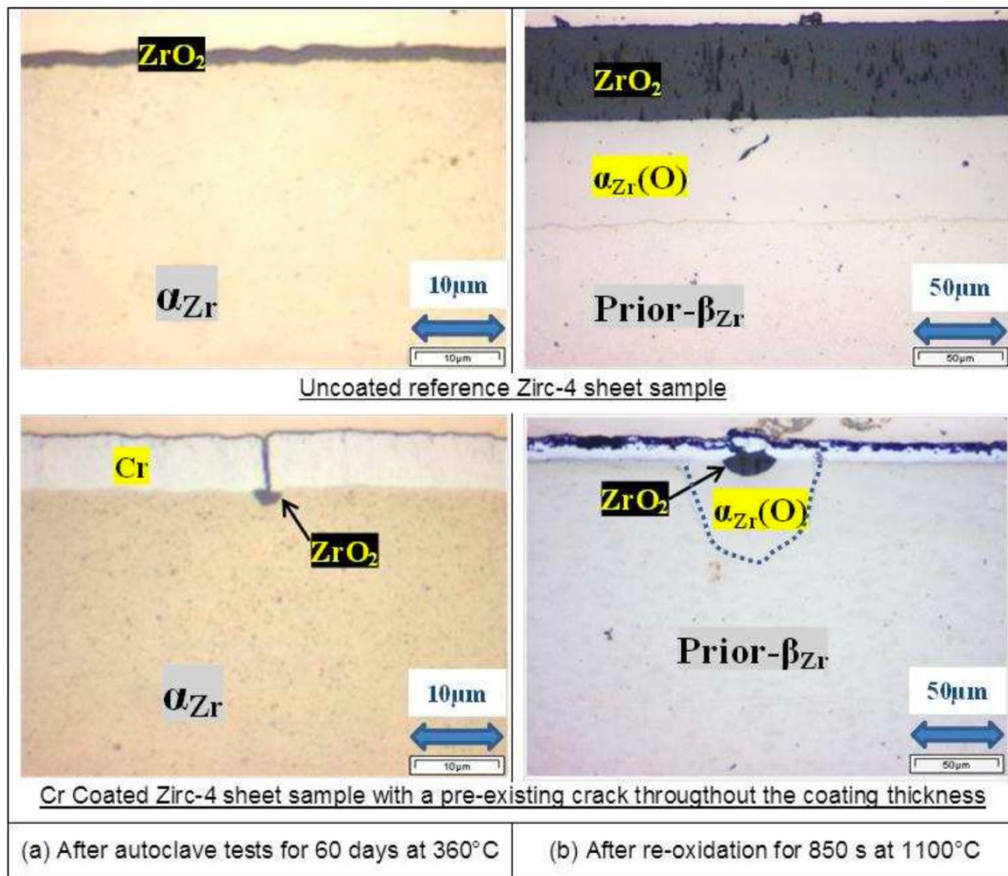
Figure 8. Optical micrographs of uncoated and Cr-coated Zr-4 sheets samples in different conditions [14].

The results show that Cr coatings exhibit a promising behavior with a good compromise between corrosion resistance in normal conditions, adhesion on the Zr substrate and improved resistance to steam oxidation at high temperature [13].

STATE OF ART

Deposition techniques

The most used surface modifications of Zr alloys claddings are:

- Spraying processes, such as cold spraying, laser spraying, and HVOF (high-velocity oxy-fuel spraying), can produce relatively thick coatings up to more than 100 μm. The microstructure of such films shows porosity and it contains a significant number of secondary phases. The main advantages are high deposition rates, low costs, and easy quality control. The major issues are the rough surface of the deposit and the changes in composition between the raw material and the coating. Post-treatment processes are always required to overcome these problems.

- Deposition by magnetron sputtering results in dense coatings with minor or no secondary phases. The coating thickness is usually limited to a few μm. **Figure 9** shows typical cross-sectional views of Ti$_2$AlC coatings deposited by spraying and magnetron sputtering with different microstructures. Sputtering and evaporation produce a vapor of the target, which condenses and deposits on the substrate. Dense films with extremely smooth surface, good mechanical properties, and high adhesion can be produced. The major obstacles are the high costs due to the complex machine structure and the relatively low coating rates. The microstructure, composition, and performance of such coatings can be significantly influenced by the substrate surface conditions and process parameters (substrate temperature, ion current density to the substrate, etc.) [15].

- Other processes, such as electroplating or plasma electrolytic oxidation, were investigated, but no follow up regarding ATF application appeared before 2017. The development of novel surface treatment techniques, such as laser flashing or electron beam remelting, to densify the coating, offers the potential to use these processes [1].

- CVD processes usually run at much higher temperatures than PVD ones, with higher growing rate. MOCVD makes use of toxic precursor, which will severely restrict the practical application of this process.
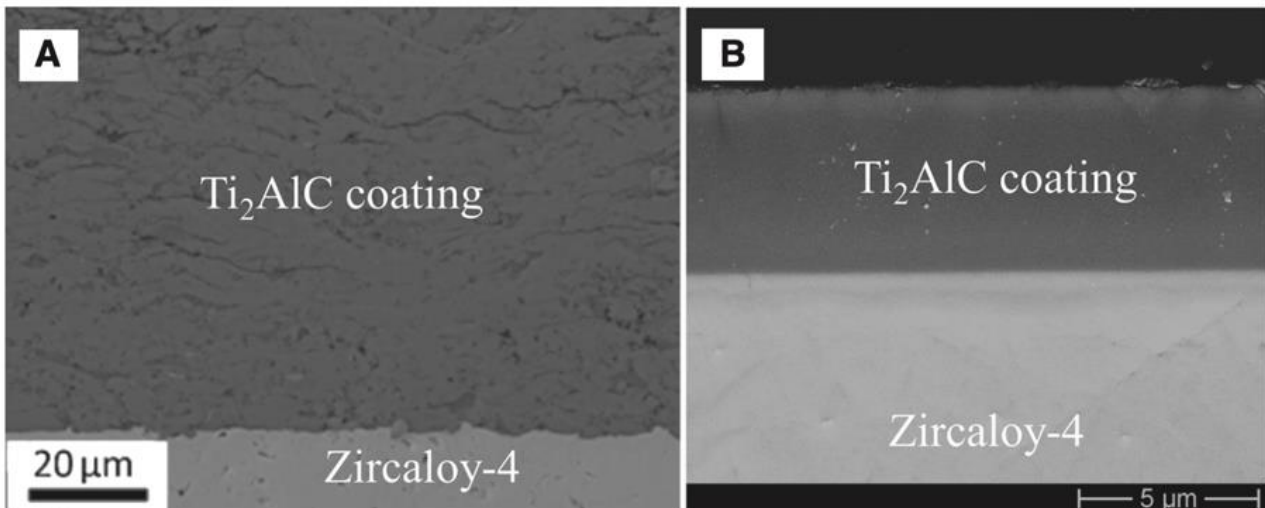
Figure 9. SEM cross section of annealed Ti$_2$AlC coating: (A) cold spaying and (B) magnetron sputtering [1].

Zirconium alloys and other nuclear materials

The material used for nuclear cladding tubes must have important characteristics: low thermal neutron capture cross-sections, high thermal conductivity, high strength, and high corrosion resistance. From considerations of neutron economy, the material choice suitable for water-cooled reactors is restricted to metals like Al, Mg, and Zr or their alloys. However, severe blistering and accelerated corrosion precluded the application of aluminum for application with temperature above 150°C. Be, Mn and their alloys also were not considered as cladding materials, since their insufficient mechanical properties and corrosion resistance in water-cooled reactor operating at temperature range of 200–300°C. In normal operating temperature (300°C), Zr is an exceptional metal for this kind of applications.

Zr alloys were selected in the late 1940s to contain the urania in light water nuclear reactors for the US Navy submarines, applied in civil power generation in the late 1950s and successfully used in LWRs for over 60 years, mainly because their corrosion and degradation issues have been progressively understood and controlled by the nuclear industry [12,16,3].

In a nuclear plant, the fuel is in the form of rods, which consist in long tubes (4 or 6 m long, with approximately 1-cm diameter and 0.6-mm wall thickness) made of Zr alloys and they contain the uranium dioxide pellets. Rods are assembled in bundles of approximately 100 rods each.

35

As the core starts to heat up, the pellet and cladding are immediate subjected to thermal expansion. To avoid mechanical interaction, the gap between pellet and cladding is filled with He. He is pumped inside the cladding to check the presence of leakages and it optimizes the heat exchange between fuel and cladding [7].

The pellet as fabricated contains 5% porosity and initially it undergoes densification due to the irradiation process. Subsequently, fission products are generated and the pellet experiences swelling. Depending on the thermal history (normal operation ramps or sudden RIAs), the gap between the pellet and the cladding disappears. This is due to the swelling of the pellet and to the creep of the cladding in pressurized water. After this point, the stress state in the cladding is dominated by the mechanical interaction with the fuel pellet. The capability of the cladding to exhibit ductility and accommodate pellet expansion is key to its integrity.

While radiations reduce the mechanical properties of Zr alloys, the most significant loss in ductility of claddings is due to hydrogen absorption generated by Zr corrosion in water.

Very small changes in Zr alloys composition and microstructure can cause significant corrosion differences: it was recognized that the corrosion resistance of Zr alloys improves with purity. A further feature of the Zr alloys is that a very small addition of alloying elements (typically less than 0.5%) is sufficient to exhibit significant changes also in mechanical properties.

Sn is a good corrosion inhibitor, and most effective in improving corrosion resistance in N-containing Zr alloys, without seriously affecting the neutron economy. Additionally, Sn increases the yield strength and it maintains good creep properties. Nevertheless, Sn contents higher than 1.5% were observed to deteriorate the corrosion resistance.

Fe, Cr, and Ni have important effects on the corrosion behavior. The Zr alloy contaminated by stainless steel, during the fabrication process, showed a beneficial effect on the corrosion resistance at high temperature. Fe and Cr have a very low solid solubility and, for the same amount of content, the strengthening effect is much larger than Sn. Cr is not only added to improve the corrosion resistance, but also to enhance creep resistance and tensile properties. Ni has a detrimental effect on hydrogen absorption, so its amount is kept within the permissible limit.

The addition of Mo enhances the yield strength and the ultimate tensile strength. Since Mo is generally harmful to corrosion resistance and has relatively higher thermal neutron absorption cross-section, the addition is recommended to be below 0.1%.

Si also has low thermal neutron absorption cross-section, and small amounts of Si provide an increase in the oxidation resistance and creep resistance.

Al is a very effective α-solution strengthener due to its high solubility in α-Zr, it has low thermal neutron absorption cross-section but, is not acceptable because of it is detrimental for corrosion resistance.

Instead of Sn addition, russian nuclear industry focused more on the effects of Nb, which is beneficial as much as Sn. Nb is highly soluble in β-Zr and has solubility of 1,1% at 600°C in α-Zr (**Figure 10**). Nb has beneficial effects similar to Sn, for instance, it counter acts the negative effects of N, C, Al, Ti, and most important, it is better than Sn as hardening agent, and it also reduces the absorption of hydrogen. Further, Nb addition in Zr alloys improves the mechanical properties and it maintains a relatively low thermal neutron capture cross-section. The most important are E110, and E635 alloys, whose chemical compositions are listed in **Table 2**, they have been designed in Russia for VVER (Водо-водяной энергетический реактор: Water-Water Power Reactor) and RBMK (Реактор Большой Мощности Канальный: High-Power Channel-Type Reactor). Both E110 and E635 have high strength, creep resistance, and resistance to radiation. The optimal solution proposed for the VVER fuel assembly was: E110 for claddings and E635 as material of the structural components, since E110 has higher uniform corrosion resistance but insufficient geometrical stability, which could be compensated by the advantages of E635 [10].

To reduce the corrosion and improve the mechanical properties of the cladding, proper Zr alloys have been developed. Westinghouse (USA) uses ZIRLO and Optimized ZIRLO alloys for their PWR, while Zircaloy-2 for BWR. Framatome (France) uses M5 for their PWR, and Zircaloy-2 for BWR. Global Nuclear Fuels (General Electric-led joint venture with Hitachi Ltd) supplies BWR fuel and has recently received approval for ZIRON cladding [17,18].

Table 2. Compositions of nuclear Zr alloys [17].

Alloy	Nominal alloy composition (wt%)				
	Sn	Nb	Fe	Cr	O
Zircaloy-2	1.5		0.14	0.06	
Zircaloy-4	1.3		0.2	0.1	
E110		1.0			
E635	1.2	1.0	0.35		
ZIRLO	1.0	1.0	0.1		
Optimized ZIRLO	0.67	1.0	0.1		
M5		1.0			0.14
ZIRON					

Zr-Cr phase diagram

The interface between substrate and coating must provide a sufficiently strong and stable bond to prevent delamination and failure of the coating.

Interfacial reactions between substrate and coating materials are governed by diffusion mechanisms. The resulting crystalline phase at the interface will influence the overall performance and properties of the component, thus these interfacial phases are a critical aspect of a designed coating.

Equilibrium phase diagrams provide a convenient way to illustrate the crystalline phases that may be present at the interface. In addition, the phase diagram also provides information about transformation temperatures (melting, eutectic, solid-state) that may be the reasons for limitations on the service of the coated component.

In the particular case of Cr-coated Zr substrates, the Zr-Cr phase diagram illustrates the equilibrium phases that may exist at the interface (**Figure 10**).
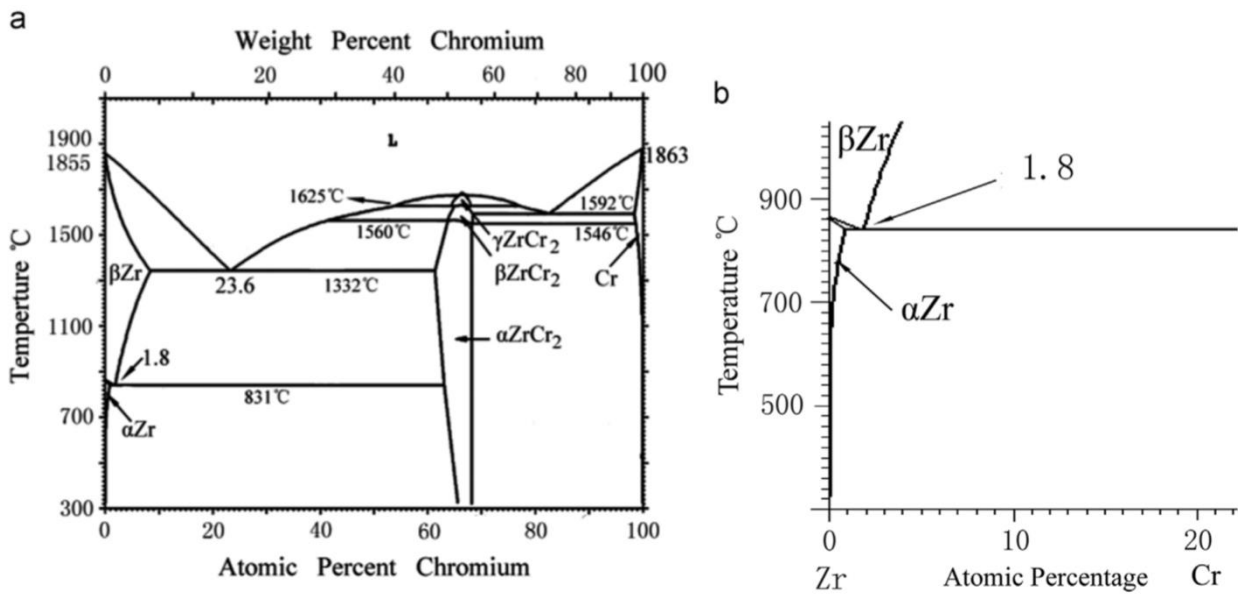
Figure 10. (a) Zr-Cr binary phase diagram and (b) enlarged portion [19].

Pure Zr has two allotropic forms: hexagonal close-packed (HCP α-phase), and body-centered cubic (BCC in β-phase). The α to β transformation temperature is 850°C. Zr alloys remains in α-phase at the normal plant operation temperature (below 400°C). However, it is possible that during accident conditions, phase transformation from α to β occurs has negative impacts on claddings.

The alloying elements are divided into α and β-stabilizers. O and Sn, have high solubility in α-phase, stabilizing it at high temperature, and can raise the α to β transformation temperature. While β phase is stabilized by the addition of Fe, Cr, Ni and Nb. O is added to Zr alloys to increase the yield strength by solution strengthening and its level in the range of 0.11–0.16% is recommended, while N must be removed as much as possible because it deteriorates the corrosion resistance if its level exceeds 0.07%.

α-and β-Zr have extremely different properties regarding the diffusion and absorption of hydrogen, so, the tuning of a proper alloy composition and its phases is a crucial point in designing the fuel cladding elements.

The intermetallic compound $ZrCr_2$ is present in three stable phases on the Zr-Cr phase diagram. These include α, β and γ-$ZrCr_2$: the α-$ZrCr_2$ phase has a composition range of 64-69 at% Cr up to

1560°C at which it transforms into the β-phase. The high temperature γ-phases is only stable between 1625°C (β to γ transformation) and its melting temperature (1673°C).

Intermetallic compounds generally have high melting points, low densities, and exhibit superior corrosion and oxidation resistance that make them ideal candidates for high-temperature structural materials.

If Cr and Zr interdiffusion occurs, the intermetallic compound $ZrCr_2$ is typically brittle at low temperature and it leads to an overall cladding embrittlement. Additionally, this compound has been observed to have poor corrosion resistance at temperature ranges between 500 and 600°C. However, it is not clear the entity of Cr-Zr interdiffusion required to cause an overall cladding embrittlement or loss of corrosion protection.

The formation of $ZrCr_2$ (in β-Zr phase) has been observed with a thickness of 4.5 μm after 225 hours at 850°C [20]. Based on these measurements an equation for the diffusivity coefficient of Cr in β-Zr phase was derived as:

$$D = 6{,}27 \times 10^{-12} e^{\frac{-1{,}26 \times 10^5}{RT}} \ (m^2/s)$$

where T is in K and R is in J/mol K [20].
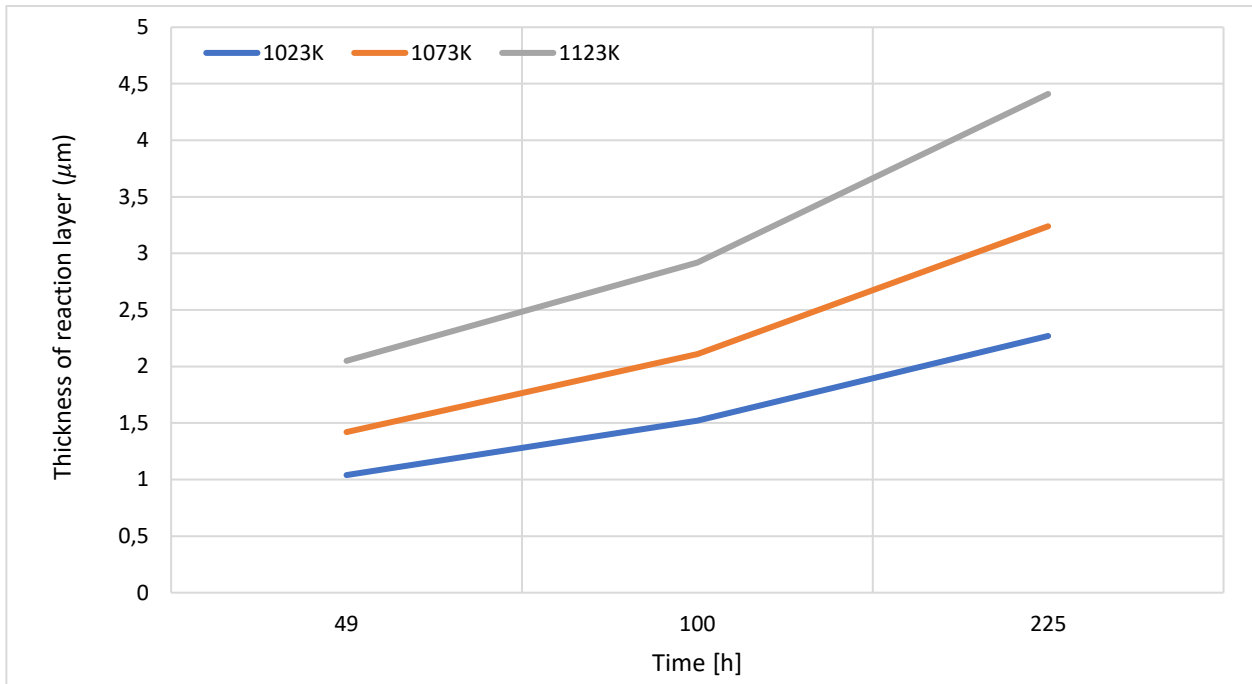
Figure 11. Thickness growth profile of interlayer by diffusion of Cr into Zr at different temperature [20].

At a given temperature and time of the process, it is possible to calculate the Cr diffusion profiles using the analytical second Fick's law solution for one-dimension semi-infinite diffusion of Cr in the β-Zr phase at high temperature:

$$\frac{C(x;t) - C_0}{C_s - C_0} = 1 - \mathrm{erf}\left(\frac{x}{2\sqrt{Dt}}\right)$$

with:

- D thermal diffusion coefficient of Cr in β-Zr;
- $C(x;t)$ concentration at a distance x from the interface, at time t;
- C_0 initial Cr concentration in the Zr substrate;
- C_s concentration at the interface.

Chromium electrodeposition

Electrodeposition is a well-established process for applying metallic coatings to improve surface properties of materials. It is possible to deposit both metals, alloys and composites, and high thicknesses can be deposited (tens of µm). Electrodeposition allows high deposition rates, it is a flexible technology with a relatively low capital costs. ZrO_2

The structure and properties of the deposited material depend on the chemical composition of the electrolyte, its temperature, and current density.

The current distribution between electrodes affects the local thickness of the growing coating. The uniformity of the thickness can be improved by controlling current distribution and hydrodynamic conditions (mechanical stirring) within the electrolytic solution.

An important parameter is the current efficiency or coulombic efficiency: this is defined as… Part of the current is wasted in parasitic reactions (e.g. hydrogen evolution). Deposition efficiencies vary with the electrolyte, plating conditions, and current density.

Chromium electrodeposition process has generally two aims: functional or decorative.

The decorative chromium plating refers to relatively thin coatings (0.1 to 1.0 µm) applied to modify the appearance of a surface.

Functional chromium, referred also as hard or technical chromium, is usually deposited as thick layer (tens of µm) in order to enhance the properties of friction, wear resistance, corrosion resistance and hardness. Functional chromium is deposited by using hexavalent Cr solutions, even though nowadays the research is focused on substituting the Cr(VI) with less dangerous Cr(III).

Trivalent chromium is used for decorative coatings. Advantages in comparison to Cr(VI) are: higher efficiency, better throwing power, higher production rates. Less energy is employed because of the lower current densities required. Also, trivalent chromium is less toxic than hexavalent one. Other advantages include lower Cr concentration levels, resulting in less Cr waste. One of the

disadvantages is that for decorative purposes, color additives must be added to reproduce the metallic outer view and to adjust the color.

In hard coating applications, the corrosion resistance of thick coatings is not good as it is for hexavalent chromium. In general, the process must be controlled more strictly than in hexavalent chromium plating, especially considering metallic impurities.

This thesis work will discuss by means of electrodeposition by hexavalent chromium.

The equipment necessary for the electroplating process is composed by:

- Insoluble anodes: lead alloys containing Sn and Sb;
- Substrate (cathode) to be plated;
- Temperature control system and heat exchanger (high current load requires cooling);
- Stirring system: uniformity in temperature and composition of bath.
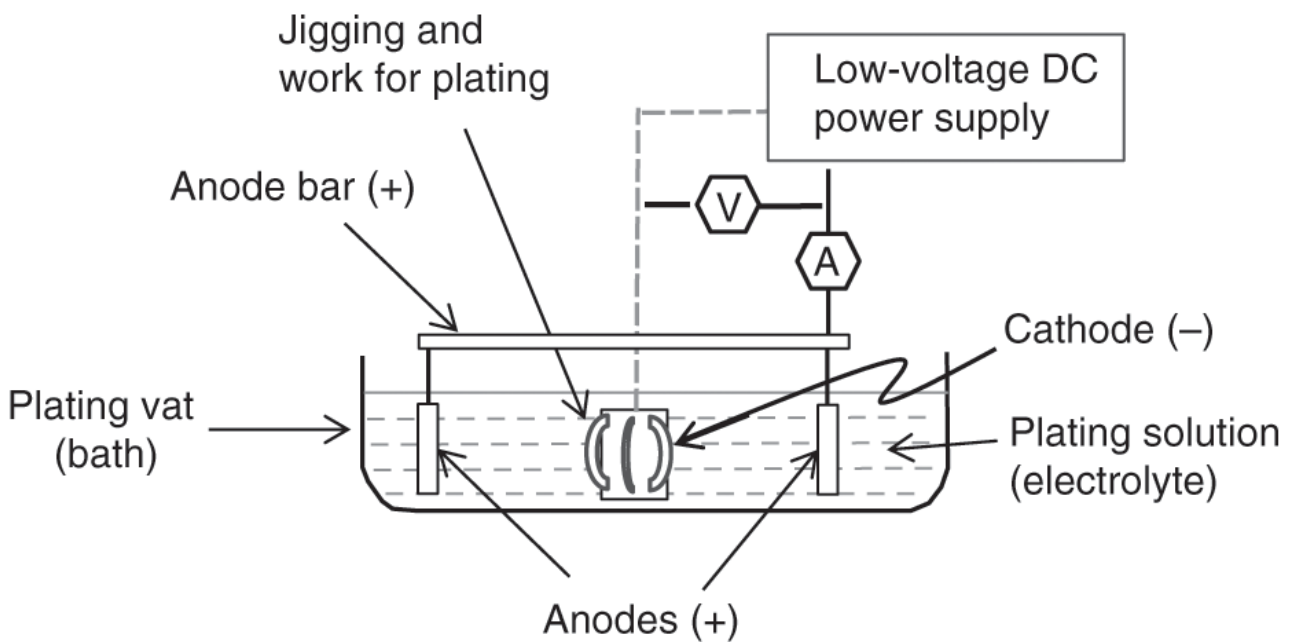
Figure 12. Schematic drawing of typical plating cell [21].

The chromium solution consists of chromium trioxide (CrO_3) between 160 up to 250 g/L dissolved in water. In some cases, for Zr electroplating, it reaches 450 g/l [22,23,24]. When the CrO_3 is added to the water, it dissolves forming chromic acid H_2CrO_4 and dichromic acid $H_2Cr_2O_7$. To control the chromic acid concentration, the density of the plating solution is commonly measured. The relationship between the density and the chromic acid concentration is almost linear.
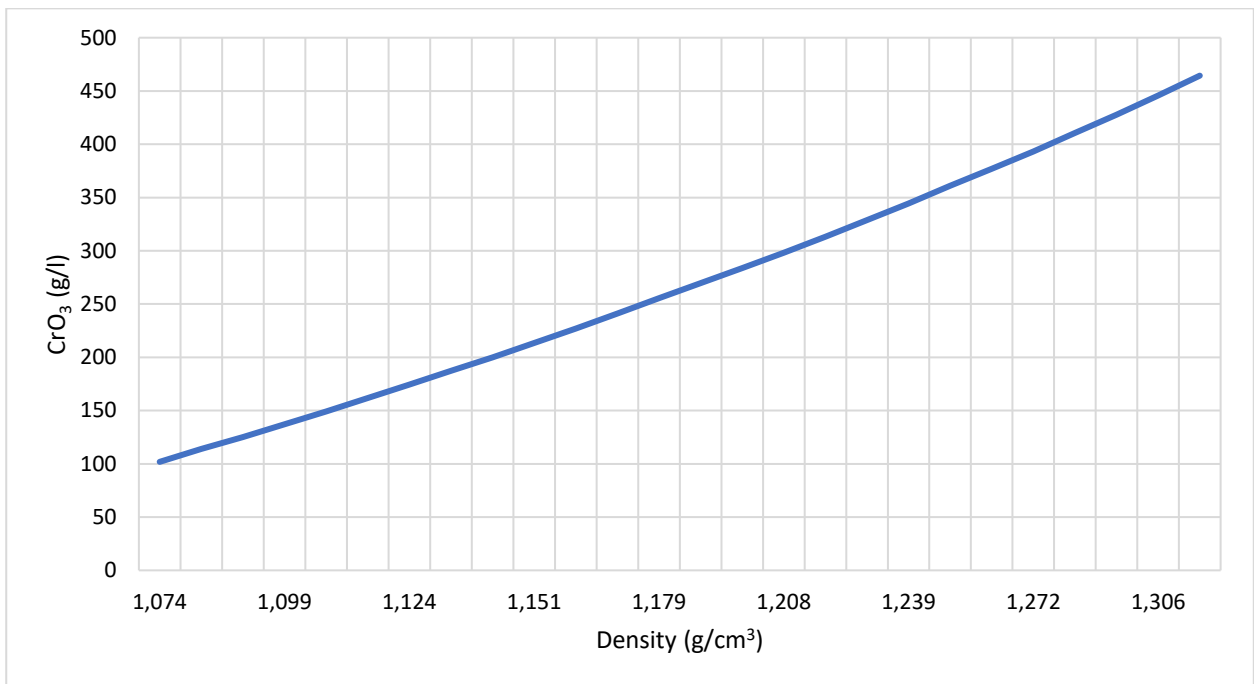
Figure 13. Density of aqueous solution of CrO_3. [25]

The conductivity plotted against the chromic acid concentration shows the maximum at a concentration between 450 and 500 g/l [26].
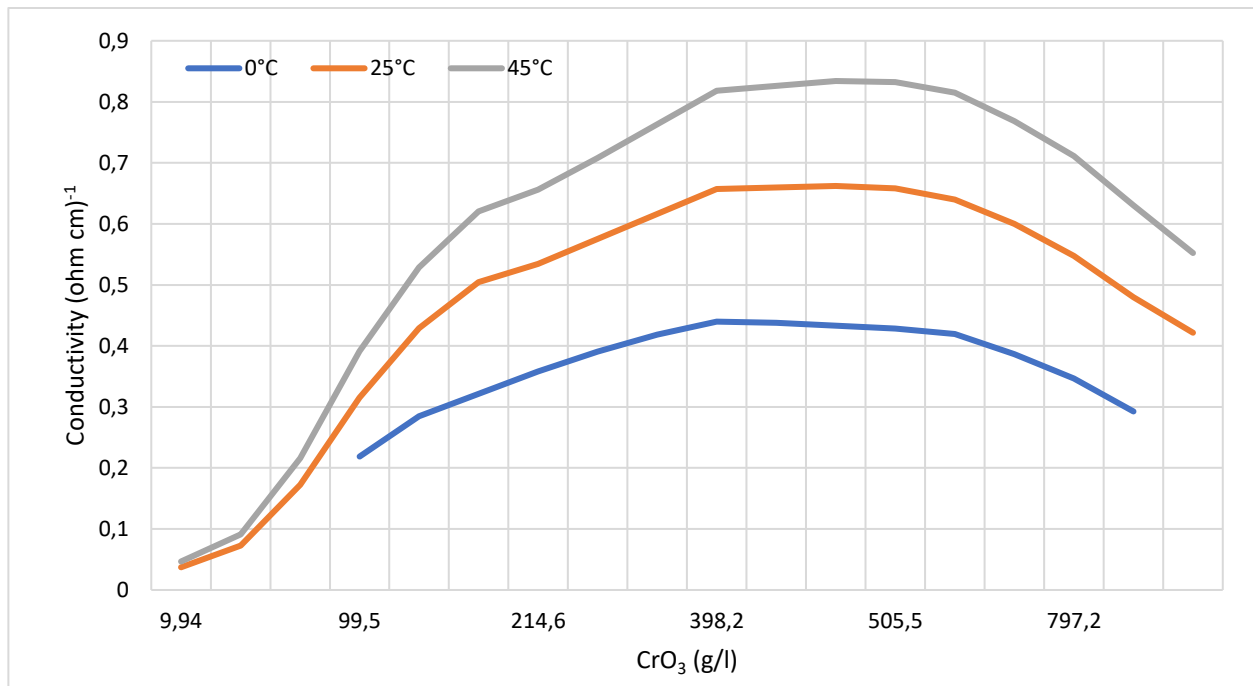
Figure 14. Conductivity vs. concentration for chromic acid solutions at different temperatures [27].

The solution contains sulfuric acid which act also as catalyst. In this strongly acidic solution, sulfates are mostly present as bisulfate ions HSO_4^-. The electroactive species is a chromate-bisulfate complex. The maximum rate of Cr deposition and the maximum concentration of this complex occur at a 100:1 chromic acid/sulfuric acid ratio. While for fluoride catalyzed solutions, the maximal efficiency occurs at around 200:1 ratio. The concentration of free fluoride should be checked regularly, and it must be quantitatively analyzed.

There is also the possibility to work with mixed catalyst solutions. Some of these solutions may contain fluorides, silico-fluorides, other complex fluorides, or organic acids. The mixed catalyst solutions have higher Cr deposition efficiencies, which increase as the chromic acid concentration or temperature is increased. Thicker and harder deposits with less nodularity can be produced. Mixed catalyst solutions can produce a better coverage, they have a wider bright range, greater tolerance to impurities and less sensitivity to current interruption.

Some disadvantages of the mixed catalyst solutions are higher difficulties to control the process, possible etching of non-plated surfaces, the bath becomes a corrosive solution, higher chemical and

plant costs. Moreover, the combination of two or more catalysts make the solutions more difficult to analyze and control.

Furthermore, high quality electroplating solutions require deionized water in the electrolyte because common ions like chlorides, fluorides, and sulfates can cause plating issues.

The chromium deposition reaction is

$$Cr_2O_7^{-2} + 14H^+ + 12\ e^- \rightarrow 2Cr + 7H_2O$$
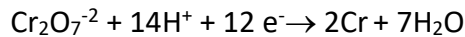
The chromate-bisulfate complex diffuses from the solution to the cathode surface and it is reduced in metallic Cr. An intense stirring of the solution is beneficial for the deposition process.

There also parasitic side reactions the first is the following:

$$2H^+ + 2\ e^- \rightarrow H_2$$
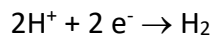
About the 80-90% of the power is consumed by this reaction, it results in the evolution of very large quantities of hydrogen gas from the cathode surface. This hydrogen can be the reason for hydrides formation and embrittlement issues.

The second parasitic reaction is

$$Cr_2O_7^{-2} + 14H^+ + 6\ e^- \rightarrow 2Cr^{+3} + 7H_2O$$
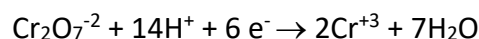
The trivalent chromium ions concentration is controlled by the oxidation reactions at the anode. The accumulation of trivalent chromium affects the current efficiency, power consumption and quality of the deposit.

The most commonly used anode material is lead alloyed with 7% Sn or 6% Sb. Sn increases the anode corrosion resistance, while Sb improves the creep resistance of lead. The alloy elements favor the formation of a conductive layer of lead dioxide (PbO_2) which improves the anode stability.

Regarding the anode reactions, oxygen is produced, and it may be discharged from water molecules or hydroxyl ions:

$$2Cr^{+3} + 3O_2 + 6\ e^- \rightarrow 2CrO_3$$

$$Pb + 4OH^- - 4\ e^- \rightarrow PbO_2 + 2H_2O$$

$$4OH^- - 4\ e^- \rightarrow 2H_2O + O_2$$

$$2H_2O \rightarrow O_2 + 4H^+ + 4\ e^-$$

$$4(OH)^- \rightarrow 2O_2 + 4H^+ + 8\ e^-$$
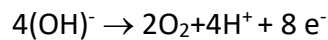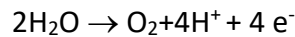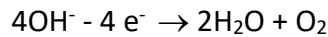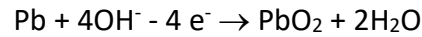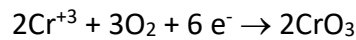
The current density determines the deposition rate, deposit hardness and plate uniformity.

$$m = \frac{MW}{zF} I \cdot t \cdot \eta$$

where m is the mass of the deposit, MW molecular weight of the deposited element, z number of electrons in the reduction reaction, F Faraday constant, I current applied and t deposition time and η coulombic efficiency.

The control of an electroplating process is achieved by making direct measurements on the solution itself (temperature, current density, metal concentration, pH…), or indirect measurements through the deposit properties (smoothness, brightness, porosity of the deposit…). The parameters directly affect the deposit: the current and time determine the deposit thickness, and the current density and solution composition influence deposit brightness and smoothness.

The Hull cell was designed to quantify this latter relationship, and to make possible the derivation of optimal plating conditions.

This device can establish a wide range of current densities on the cathode panel. In this manner, from a single test, the optimal current density ranges can be identified. With a small number of

plating tests, it is possible to verify the effect of different concentrations of additives (brighteners, levelers…) on the quality of the electrodeposit.

The shape of the Hull cell is shown in (**Figure 15**).
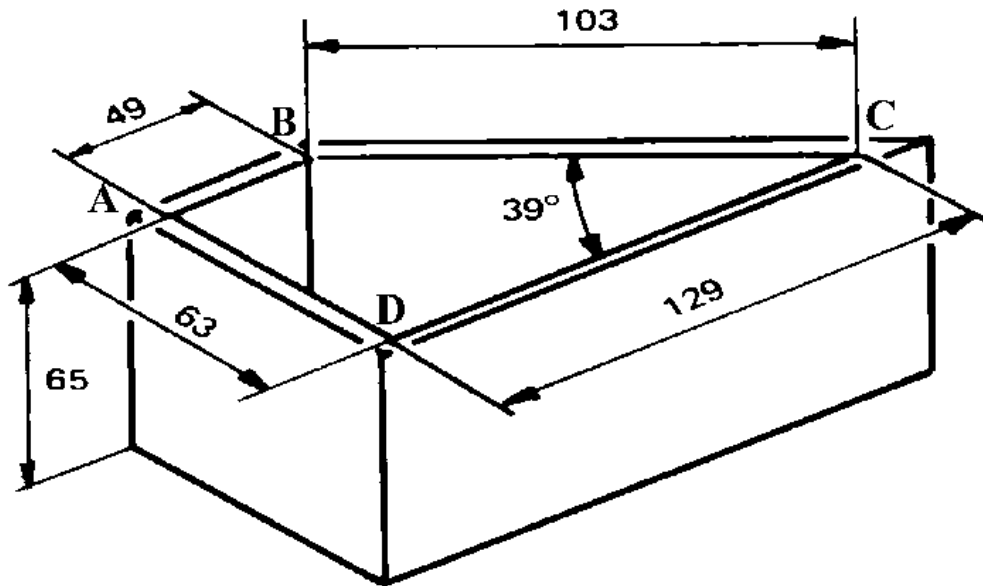
Figure 15. Schematic draw of a Hull cell (sized in mm).

A hull cell is trapezoidal, the parallel sides are insulators, the normal side is the anode and the inclined side is the cathode. Its shape gives an anode-cathode distance from 4.9 to 12.9 cm. An applied current of 2 A onto a flat cathode panel of 10.3×6.5 cm^2 provides a current density range from 0.002 to 0.01 A/cm^2.

The Hull cell therefore allows:

- to optimize current density range;
- to optimize additive concentration;
- to recognize impurity effect;
- to indicate macro-throwing power capabilities.

Calibration of the Hull cell is usually required and achieved by using thickness profiles and assuming appropriate current efficiencies. Such data yields to a calibration graph, ad example for 1, 2, 3 A (**Figure 16**).
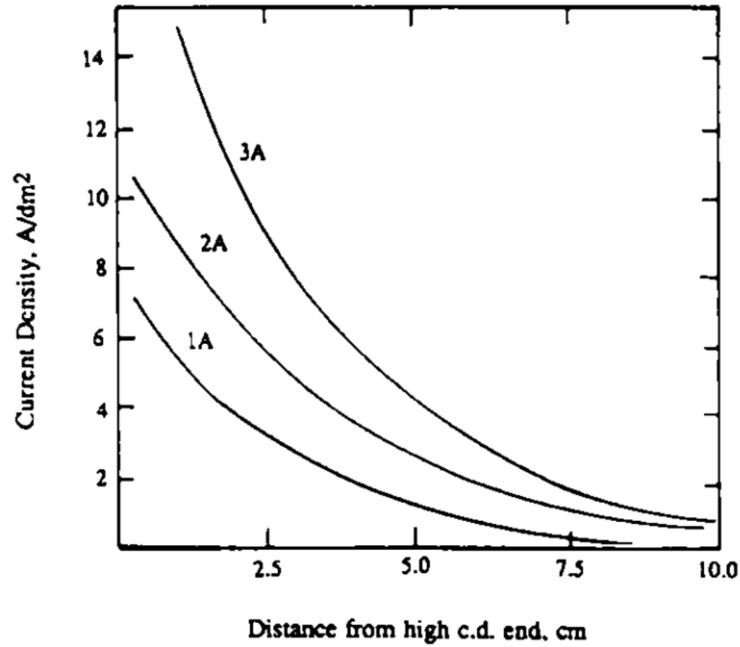
Figure 16. Hull cell calibration graph for three applied cell currents [28].

The formula for current density distribution takes the form

$$i_{(L)} = I_{app}(a - b \, log \, L),$$

where $i_{(L)}$ is the current density at the distance L being the cathode distance from highest current density region (point B in **Figure 15**), I_{app} is the applied current, and a, b are calibration coefficients. The calibration loses validity at extremities of the cathode panel. The problem has been analyzed by several authors and the preferred form, expressed in A/dm^2 and cm units is [28]:

$$i_{(L)} = I_{app}(5.1 - 5.24 \, log \, L)$$

49

The preparation of the surface has an important role in functional Cr plating, and it has a direct effect on the morphology of the deposit: poor surface condition before plating leads to pitting, nodules, and poor corrosion resistance.

Surface stresses from hardening and grinding operations may induce macro-cracks after the plating process.

The Cr deposits whose surfaces have been modified to favor the formation of micro-cracks, channels or pores is named porous chromium. In functional chromium plating, these pores may retain lubricant, thus reducing the friction and increasing the component life in wear applications. In decorative chromium plating, a micro-porous Cr coating is deposited to enhance the corrosion resistance by increasing the total surface exposed to the corrosion current. The deposits typically may have from 300 to 1200 cracks per centimeter. In hard chromium plating it is possible to achieve micro-cracking by varying the operating conditions, or post plate peening or blasting methods.

Magnetron sputtering

In plasma based PVD processes, the deposition species are either thermal evaporated or sputtered from a source (the cathode target) under ion bombardment. Sputter deposition has been known for decades as a flexible, reliable and effective method.

Thermal evaporation suffers limitations such as the difficult deposition of alloys, and the coatings are mainly characterized by a porous microstructure, while in sputtering and in other plasma based PVD processes the porosity can be controlled by tuning the energy of the deposited particles trough an external electric field.

In PVD plasmas the energies of electrons are of the order of a few eV (2 eV for example) which corresponds to 23000 K ($E=k_BT$).

Since the fraction of electrons is very small, the walls of the chamber do not heat appreciably.

To obtain plasma, a source of electron is needed: by putting an electrode at a low negative voltage, spontaneous emission of electrons occurs. These electrons are accelerated and ions may be produced by collision. Free electrons in vacuum can be also used for ionization.

$$e^- + Ar \rightarrow Ar^+ + 2e^-$$
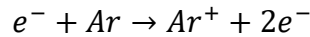
One electron is accelerated by the electric field and it collides with a gas atom. This collision will produce an ion and two electrons.

In this event, a new free electron is created, and it can create another collisional event. So, in principle, this is a self-sustained reaction. There will be also termination events: electrons can be collected from the anodes, and from all grounded surfaces inside the system.

Also, ions are involved in neutralization reactions:

$$e^- + Ar^+ \rightarrow Ar$$
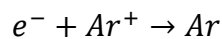
Conventional planar DCMS (Direct Current Magnetron Sputtering) commonly operates using Ar as working gas in the pressure of few Pa and an applied cathode voltage of hundreds of V, whereas the confining magnetic field strength at the target surface is in the range $20 - 60$ mT. This leads to current densities of the order of $4 - 60$ mA/cm^2 and power densities of several tens of W/cm^2 [15].

If a correct balance between collisions happens, a steady state condition is achieved. An electric field is used to accelerate the electrons giving them high energy.

Ions, electron and molecules move randomly, and they can be collected by the workpiece. So, its surface will collect a current density J which is given by the electrical charge q_i multiplied by the flux of these species:

$$J_i = \frac{q_i n_i v_i}{4}$$

being n_i the concentration of the species and v_i their mean velocity.

The mean velocity from the Maxwell-Boltzmann distribution is

$$v_i = \sqrt{\frac{8K_BT}{\pi m_i}}$$

and

$$\frac{J_{el}}{J_{ion}} = \frac{q_{el}n_{el}}{q_{ion}n_{ion}} \left(\frac{T_{el}m_{ion}}{T_{ion}m_{el}}\right)^{1/2}$$

Since the ionic current density is significantly lower than the electronic one, at one surface a negative charge will accumulate and will accelerate ions. A balance between these two current densities must exist: the electronic flow will slow down, while the ion flow is accelerated until the steady state condition is reached.

When the ions from the plasma bombard the target (cathode), they not only release secondary electrons, but also atoms of the cathode material (sputtering). The enhanced ionization, due to the confinement of the charged species by using a magnetic field, makes possible to operate at working gas pressures significantly lower (10^{-3} Pa). The aim of magnetic fields in a magnetron sputtering system is to extend the lifetime of the electrons, by trapping them in the proximity of the cathode, making collisions events more probable (**Figure 17**).

Within the magnetic field, charges species are subjected also to the electric force due to the potential difference. So, any charge will experience a Lorentz force given by:

$$\boldsymbol{F} = -q(\boldsymbol{E} + v \times \boldsymbol{B})$$

Due to magnetic forces, the electrons experience an helicoidal trajectory near the target. This is very useful because the confinement of electrons near the target increases the erosion rate of the target in comparison to conventional DC sputtering systems.
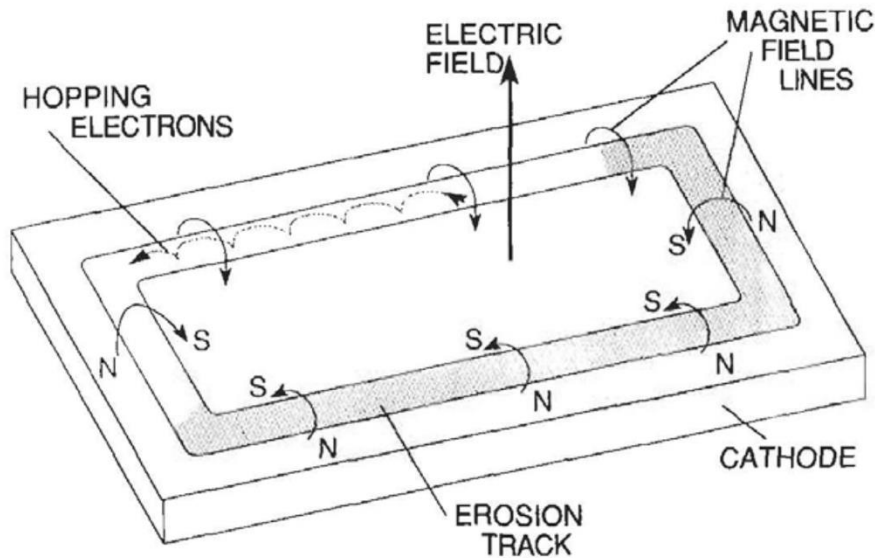
Figure 17. Confinement of electrons near the target due to magnetic field.

The magnetron sputtering technique is well established for deposition of thin films of both metallic and dielectric materials and it is easily scalable for depositions on large surfaces. Over the years, the magnetron sputtering became an extremely important technology for thin film deposition in a wide range of industrial applications. These include metallization in integrated circuits, coatings for wear resistance and corrosion protection, large area coating of architectural glass and display applications.

Depending on the deposition the applied target voltage can be constant (DC), radio frequency (RF), or pulsed.

In a DC system the cathode is kept at a constant negative voltage. The magnet assembly consists of an outer annular magnet and an inner one of opposite polarity, and the magnetic field lines go from the cathode center to the annular cathode region. Since the electrons spend more time where the electric field is perpendicular to the magnetic field, in the ideal case, the magnetic field should be parallel to the cathode surface. However, in the real situation, the magnetic field lines form arcs (erosion region), where electrons and ions are confined, by forming a dense glow discharge. Consequently, these regions are more subjected to high sputter activity.

In the planar magnetron configurations, due to the magnetic confinement, the sputter-erosion region is not uniform and leads to the formation of a circular groove-like erosion pattern. The groove formation limits the target utilization in the range 26 – 45%, resulting in higher operating costs. This also means that the deposition pattern can be non-uniform and thickness uniformity must be achieved by substrate (or target) movement.

The DC discharge is considered balanced if the magnetic fluxes of the outer and the inner poles are the same (**Figure 18**). If the condition is satisfied, the magnetic field traps the plasma just in front of the cathode target. Thus the substrate, experiences very little impingement by ions, and it is very important for depositions on heat sensitive substrates. To increase the ion flux to the substrate, the unbalanced magnetron was developed. It is based on strengthening or weakening of the magnetic flux through one of the poles, which leads to an unbalance in the magnetic circuit.

There are two types of unbalancing. In type I, all field lines originate from the central magnet and some are not passing into the annular magnet. In type II, not all field lines originate from the central magnet and all are passing into the annular magnet. These unbalanced field lines extend to the substrate vicinity. Some of the secondary electrons can follow these magnetic field lines toward the substrate. This leads to a significant increase in the ion current in the vicinity of the substrate, and the energy of the bombarding ions can be tuned by applying a substrate bias.
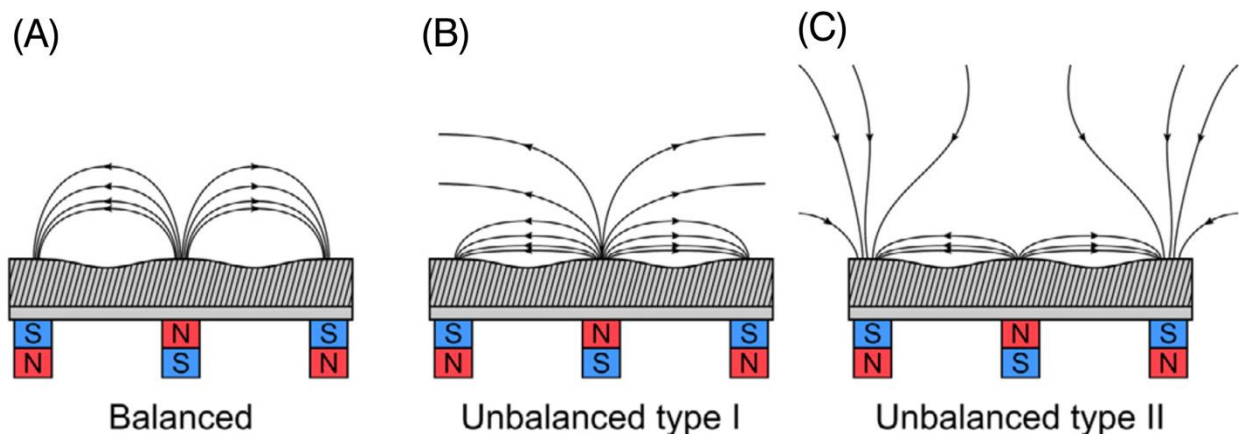
Figure 18. Schematic of the magnetic design commonly used in magnetron sputtering discharges [15].

Most of the ionization events occur in the region where the energetic electrons are trapped. An electron will move in the magnetic field with the angular frequency

$$\omega_{ce} = \frac{eB}{m_e}$$

and the corresponding rotation radius is

$$r_{ce} = \frac{u_{e,\perp}}{\omega_{ce}} = \frac{u_{e,\perp} m_e}{eB}$$

where $u_{e,\perp}$ is the electron speed perpendicular to the magnetic field B. Typical values for r_{ce} are $1 - 10$ mm. This means that the electrons are confined in proximity of the target since, their rotation radius is much smaller than the characteristic size of the system. As a comparison, ions have a rotation radius r_{ci} in the order of 1 m, which is larger than the characteristic size of the system, and, the ions are not confined by the magnetic field.

The glow discharge is sustained by secondary electron emission from the cathode and by ion bombardment. The discharge current at the cathode consists of electron I_e and ion current I_i

$$I_D = I_e + I_i = I_i(1 + \gamma_{see})$$

where γ_{see} is the secondary electron emission coefficient. It is worth mentioning that $\gamma_{see} = 0.05 - 0.20$ for most of metals, so the dominating contribution of the discharge current is due to ions.

MATERIALS AND METHODS

Materials

In this work Cr deposited by electroplating (in Milan) and by magnetron sputtering (in Tomsk) will be analyzed and compared. Characterization of the coatings before and after oxidation test will be the subject of this work.

The deposition substrates are Ti grade 1 and Zr-1Nb alloy E110 (see **Table 2**).

Electrodeposition

The first set of electrodepositions were carried out on Ti grade 1. The choice of Ti is due to the similar capability to Zr to passivate its surface very quickly, creating superficial tenacious oxides. This causes many difficulties in electroplating on material such as Ti, Zr, Al, Mg and stainless steel. These materials require special surface activation treatments to obtain an adherent plating [29]. The main task was to eliminate this oxide layer and avoid its re-formation during the process. Some etching and activation solution containing fluorides have been suggested in many patents [29,30,23,22].

The equipment used to electrodeposit Cr on Ti and Zr substrate include:

- Power supply: Elektro-Automatic PSI;
- XRF (X-ray fluorescence): Fischer scope XAN;
- Magnetic stirrer
- Thermometer
- Chemical reagents technical and some analytical grade:
  - HF (38-40%)
  - CrO_3
  - H_2SO_4 (96%)
  - $NaHF_2$
  - HNO_3 (65%)

The dimensions of Ti samples were 3.5 cm × 6.5 cm × 1 mm, while the Zr alloy pieces 1.5 cm × 1.5 cm × 2 mm

A support of insulated Ti with Kapton has been used to coat the Zr alloy samples. In addition, to compute the optimal current density for the deposition process, the Hull cell has been used.

The starting procedure to coat Ti consisted in:

1. substrate degreasing with acetone or ethanol to eliminate organic contaminations;
2. chemical pickling for 3-4 min in an aqueous solution containing 10% vol. HNO_3 (65%) and 10% vol. HF (38-40%) at room temperature;
3. rinsing with distilled water;
4. electrodeposition in aqueous electrolyte containing 250 g/l CrO_3 + 2.5 g H_2SO_4; using lead anode (distance cathode – anode about 8 cm).
5. rinsing with distilled water.

Magnetron sputtering installation

Cr coatings with different thicknesses have been deposited on Zr-1Nb.

In each set of depositions, the Cr coatings have been deposited also on polished Si (110) substrates. The scheme of the ion-plasma installation is shown in **Figure 19**.
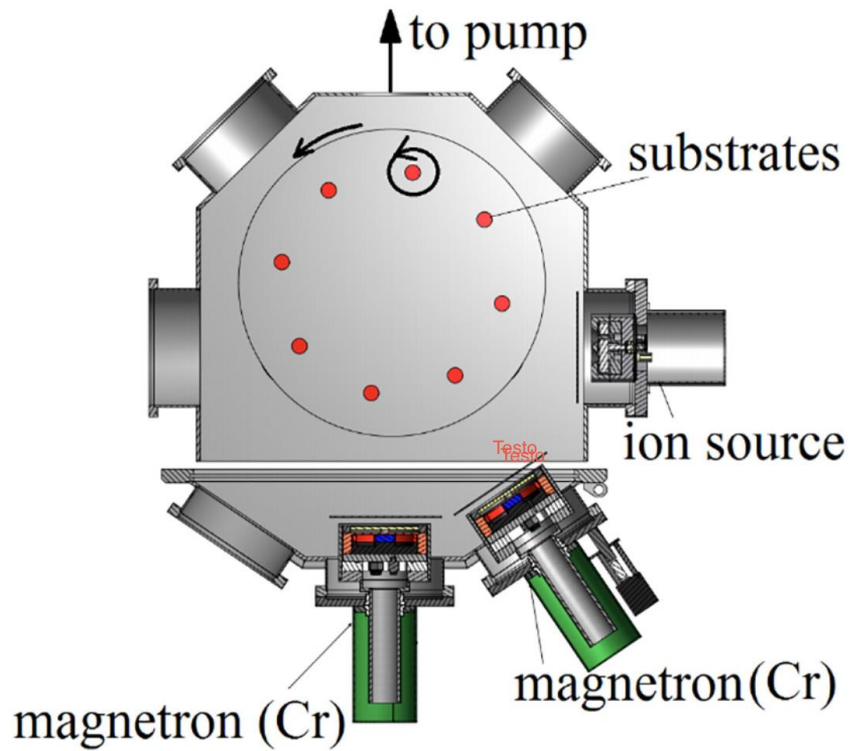
Figure 19. Scheme of magnetron sputtering installation [31].

The magnetron sputtering consists in a vacuum system with a spiral, a turbomolecular and a cryo-genic pump, two (or three for high thickness deposition) magnetron sputtering systems with disk (Ø 90mm) targets, ion source, planetary substrate-holder (8 holders) and substrate biasing system. For the depositions, the unbalanced (Type 2) magnetron sputtering system with Cr target (99.95%) was used.
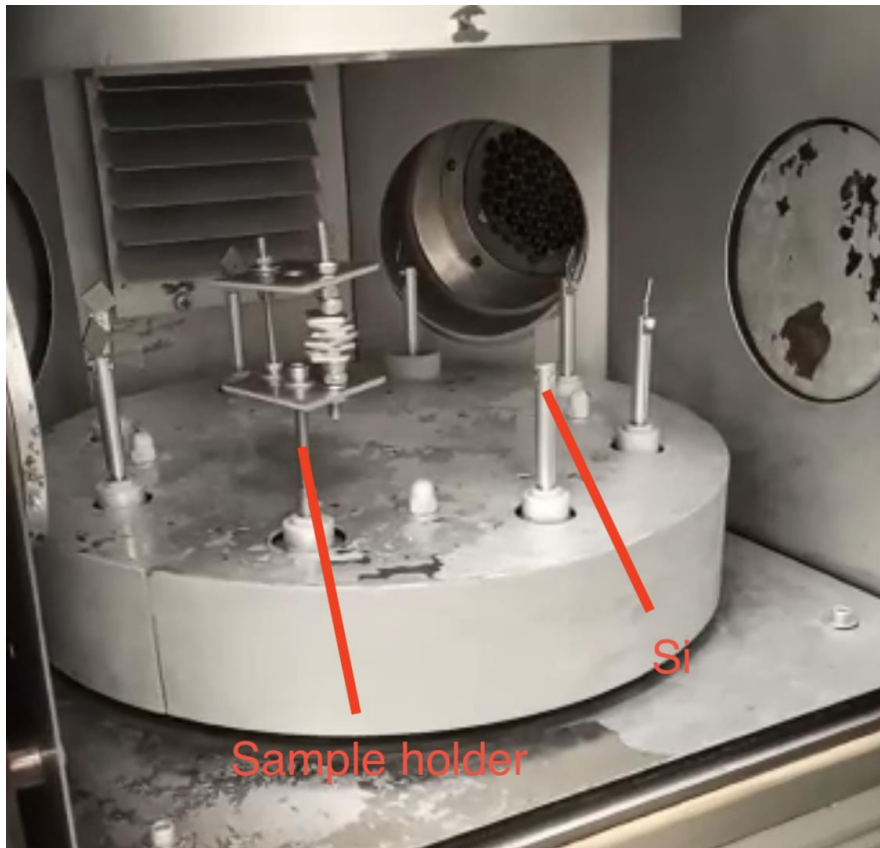
Figure 20. Photo of magnetron chamber. Inside there are: 1 Si substrate, 6 Zr-1Nb samples and 1 sample holder which contains 7 electroplated samples.

The magnetron and substrate biasing system had direct current (DC) power supplies of APEL-M series (Apelvac, Russia). The base pressure was 2×10^{-3} Pa. The distance from targets to the substrates was 100 mm. The substrates were planetary rotated, during both the ion treatment and the coating deposition, to uniform the coating thickness.

In the chamber an ion source is present by which the samples were cleaned by plasma etching and it is present also a carbon heater. Before deposition, the substrates were treated by ion source in Ar atmosphere to remove surface oxides and contaminations.

The ion source worked for 30 minutes with potential 2500 V, current 46 mA, pressure 0.15 Pa, Ar inflow 7-8% from 150 cm^3/min, U_{bias} = -600 V, I_{bias} = 0.04-0.05 A (pulse frequency of bias 100 kHz, duty cycle 70%). Such parameters have been chosen to decrease the arcing probability on the substrate surface during etching stage.

The carbon heater has a temperature of 1000 °C and it allows to maintain the temperature of the working pieces at 300°C.

To control substrate temperature, an infrared pyrometer Optris CT laser 3MH1CF4 was used during coating deposition.

Cr has been deposited onto galvanic samples in order to uniform the uncovered corner. The process lasted for 64 minutes (for an estimated thickness about 2 μm). The result was reproducible for all the samples and the magnetron deposited Cr is adherent to the galvanic one. Multi-cathode magnetron sputtering was elaborated for the depositions.
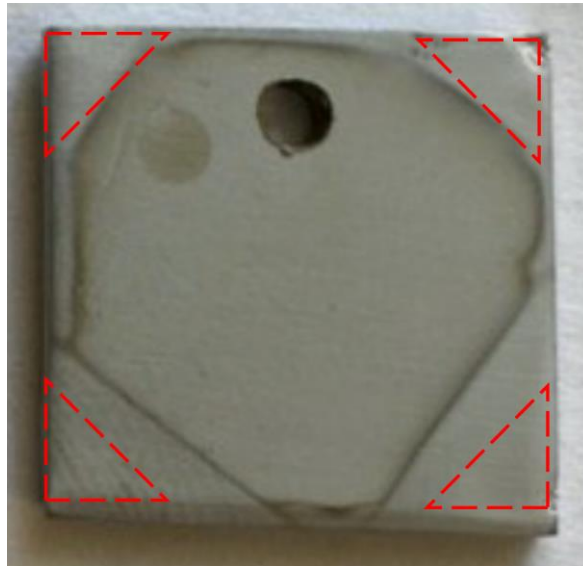

Figure 21. Electrodeposited sample (Zr-1Nb) with magnetron-deposited Cr on the corners (red triangles indicate the original uncoated areas).

The operating parameters for Cr coatings depositions are listed in

Table 4.

A sample holder has been built to deposit the Cr on the corners of the uncoated areas of electroplated samples (**Figure 22**, **Figure 80**):

Figure 22. Sample holder to deposit Cr on corners of electroplated samples.

Cr deposition onto Zr-1Nb alloy by magnetron sputtering

Zr-1Nb samples have been subjected to some necessary pretreatments before deposition:

0. grinding and polishing by sandpaper from 600 up to 4000 grit;

1. immersion in a cleaning solution (3 g of "Flatter" soap in 200 ml water) at 100°C for 6 minutes;

2. rinsing in water at 50 °C for some minutes;

3. rinsing in room temperature water and then with current tap water for 6 min;

4. immersion in alcohol solution and boiling (1-2 min) and drying in its vapor;

5. drying in air (oven) at 106 °C for 10 min to evaporate any alcohol and water.

Four set of magnetron sputtering depositions of Cr were made: three consist in deposition of Cr on Zr-1Nb alloy with different thicknesses (Cr-59, Cr-61, Cr-62); the fourth set (Cr-60) was carried out on electroplated sample in order to deposit Cr onto the uncovered part near the corners.

Figure 23. Sample holders for magnetron deposition onto Zr-1Nb samples.

Steam oxidation

High-temperature oxidation in steam was carried out by using an ITM facility at a temperature of 1200 ± 3 °C for 5 (LOCA 1) and 20 (LOCA 2) min. The facility in operation is shown in **Figure 24**. According to this scheme, the samples were placed in the open-top quartz reaction tube (1) at the level (3) and fixed with quartz fiber. After switching on the facility, the tube furnace (2) heats the quartz reaction tube (1) up to the indicated temperature. The temperature is maintained using the control unit (5) and the thermocouple (4). Steam is generated when water evaporates from the tank (7) heated by the heater (8). The steam flow rate is about 1.15 $g \cdot cm^{-2} \cdot min^{-1}$. Steam is injected into the reaction tube (1) through the drip evaporator (6).

Figure 24. The ITM facility for high-temperature oxidation in steam. On the left it is in operation, on the right its scheme (1. Quartz reaction tube; 2. Tube furnace; 3. Specimen location; 4. Pt/Rh-Pt Thermocouple; 5. Control unit; 6. Drip evaporator; 7. Water tank; 8. Heater).

The samples at room temperature were introduced in the steam environment at 1200°C. After the period of staying in the chamber, samples were immediately immersed in water at room temperature, thus, providing two hard thermic shocks.

Air oxidation

Oxidation in air was carried out at 1100°C. A furnace (ATS 3210, Applied Test Systems Inc.) and a temperature control system (ATS AB-900, Applied Test Systems Inc.) were used.
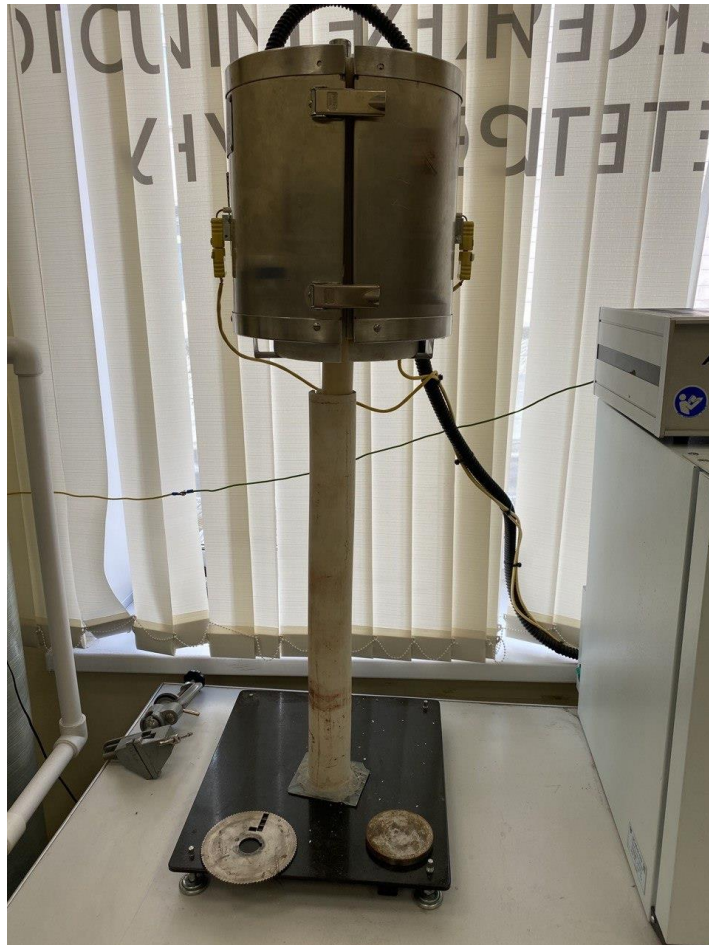

Figure 25. Atmospheric furnace for oxidation test.

The samples were fixed in the furnace chamber by ceramic (quartz) wire and heated following the thermal profile in **Figure 27**.

Figure 26. Samples (3 electroplated, 3 magnetron and 1 uncoated) ready for oxidation test in atmosphere.
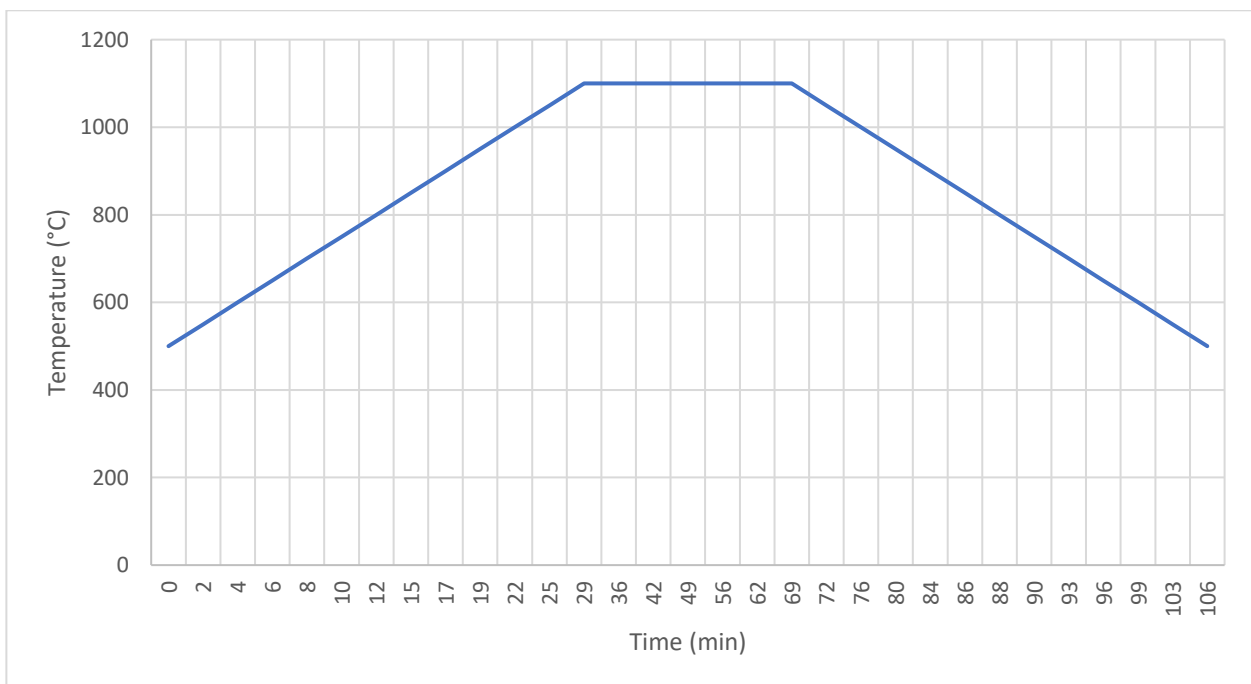

Figure 27. Temperature profile of samples in the atmospheric test.

The thermal profile of the atmospheric test consists in a pre-heating of the furnace until 500°C, introduction of samples in the chamber, heating up to 1100°C in 29 min with heating rate of 20.7

°C/min, steady state condition (isothermal test at 1100°C) for 40 minutes and then, cooling down from 1100°C to 500°C in 37 minutes (cooling rate of 16.2°C/min), then, extraction and cooling of the sample at room temperature.

Characterizations

Gravimetry test

Weight measurements were carried out on the deposited samples (electrodeposited and magnetron-deposited) and uncoated Zr-1Nb, to evaluate the weight gain and to compute the oxidation rate.

The weight gains of the samples after oxidation tests were measured using analytical balance machine (Sartorius CP124 S) with an accuracy of 10^{-4} g.

To be more precise, a relative sample has been weighted as well with the aim to evaluate the presence of differences in weights due to external causes (e. g. atmospheric contaminations).

To analyze qualitatively the results of the oxidation tests, gravimetry measurements have been carried out and the mass gain (normalized on the coated surface) for each sample has been computed.

Those computations were made by considering the difference of weights of the samples before (m_1) and after (m_2) the tests.

$$\Delta m = m_2 - m_1$$

Every sample has both uncoated and coated regions.

$$S_{tot} = S_{Uncoated} + S_{coated}$$

To compute the mass gain of the coated samples, the contribution due to the uncoated areas must be known. By knowing the mass gain of uncoated Zr-1Nb samples ($\Delta m_{Uncoated}$), this contribution ($W_{Uncoated}$) is

$$W_{Uncoated} = \frac{\Delta m_{Uncoated}}{S_{Uncoated,Zr}}$$

Since the sample is completely uncovered, $S_{tot} = S_{Uncoated,Zr}$.

Every dimension of uncoated part of the samples has been measured, thus, the $S_{Uncoated}$ of each sample is known and the mass gain contribute due to the uncoated surface will be:

$$\Delta m_{Uncoated} = S_{Uncoated,Sample} * W_{Uncoated}$$

The mass gain contribute due to the coated part is

$$\Delta m_{Coated} = \Delta m - \Delta m_{Uncoated}$$

And finally, the mass gain due to the coated part normalized to its surface is:

$$W_{coated} = \frac{\Delta m_{Coated}}{S_{coated}}$$

X-ray diffraction (XRD) analysis

Crystalline structure of the samples was studied by X-ray diffraction (XRD) using Shimadzu XRD-7000S in a Bragg-Brentano configuration with CuKα-tube (40kV, 30mA). The scanning range was 10–90° with an exposure step of 0.03°.

GDOES

A glow discharge optical emission spectroscopy (GDOES, GD-Profiler 2 HORIBA Scientific) was used to evaluate the elemental distribution in the samples before and after high-temperature oxidation in steam environment.

LECO

LECO instrument (RHEN602) has been used to determine the hydrogen content of samples. The starting point of the procedure is to warm up or melt the sample in a furnace with electrodes in

inert gas environment. The hydrogen is measured by detecting the thermal conductivity changes of the transport gas.

Figure 28. LECO installation for hydrogen content measuring in metals or alloys.

Scanning electron microscopy

The thickness and cross-section of the as deposited Cr coatings were measured by scanning electron microscopy (SEM) using Quanta 200 3D.

Procedure to prepare the metallographic samples to SEM microscopy:

1. cutting the samples;
2. preparing a plastic base where to place the sample and to avoid resin leakages;
3. mixing 1 part of liquid "Technovit" and 2 parts of powder "Technovit" (% wt);
4. adding the resin in the plastic base. After 30 min the resin is solid. Wait two hours;
5. polishing the surface starting from sandpaper 400 up to 4000 grit.

Optical microscopy

The thickness and microstructure of the as-deposited and oxidized samples were studied by an optical microscopy using AXIOVERT 200MAT.

Adhesion Test

The adhesion tests were carried out with a Micro Scratch Tester with which acoustic emission, tangential force and profile depth have been analyzed.

The parameter for the scratch were: progressive type, with a starting load of 0.01N, a final load of 30 N and a loading rate of 30 N/min along a scratch groove of 7 mm.

The indenter was Rockwell type (C-029) made of diamond with a radius of 100 µm.

RESULTS AND DISCUSSION

Electrodepositions

Preliminary tests on Ti

The first bath used had a standard composition of 250 g/l CrO_3 with H_2SO_4 as catalyst in a weight ratio 100:1 (base electrolyte). First, different times of deposition and different current densities have been tested.

The most interesting Cr layer were obtained by using electroplating solution contaminated with fluoride arising from the etching solution.

For this reason, some intentional additions of fluoride to the fresh bath were made.

Once the electroplating process on Ti was stabilized and reproducible, experiments on Zr substrate started.

Effect of time of deposition

The experiments on deposition time effect were carried out by using a stirred base electrolyte at 50°C and a current density of 0.39 A/cm^2. The deposition time, in the range from 15 to 60 min, the Cr layers were affected by strong internal stresses causing the cracking of coating **Figure 29**. The samples were prepared in a sequential way using the same electrolyte. For every sample, the procedure discussed in "**Electrodeposition**" section has been carried out.
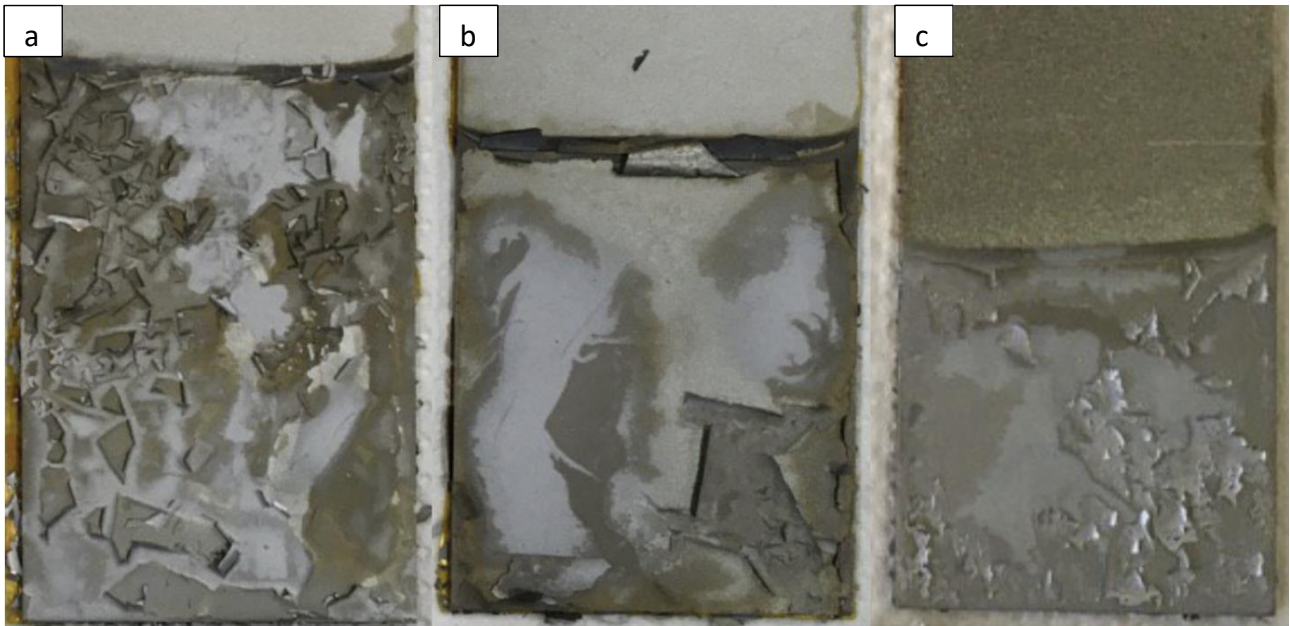
Figure 29. Effect of time of deposition on Ti substrate (samples # 2, 3, 4) for (a) 60 min; (b) 30 min and (c) 15 min (in base electrolyte, 0.39 A/cm², 50°C).

Effect of fluorides content

Baths containing only sulphates as catalyst resulted ineffective, instead, by adding fluorides to the solution, gave better results. Experiments with additions of HF (38-40%) 2, 5 and 10% (vol.) to the base solution were done. The aim was to exploit the possibility to destroy the passive film of Ti but, high quantities of fluorides in the electrolyte did not carry to any Cr deposit. No deposition (XRF analysis) was observed for concentrations of 5% and 10% at 50°C and 0.39A/cm² (**Figure 30**). The experiments have been repeated by using a current density two times higher: in this case, for concentration of 2%, the quality of Cr deposited was slightly improved (**Figure 31**). This is in agreement with findings of ref [32].
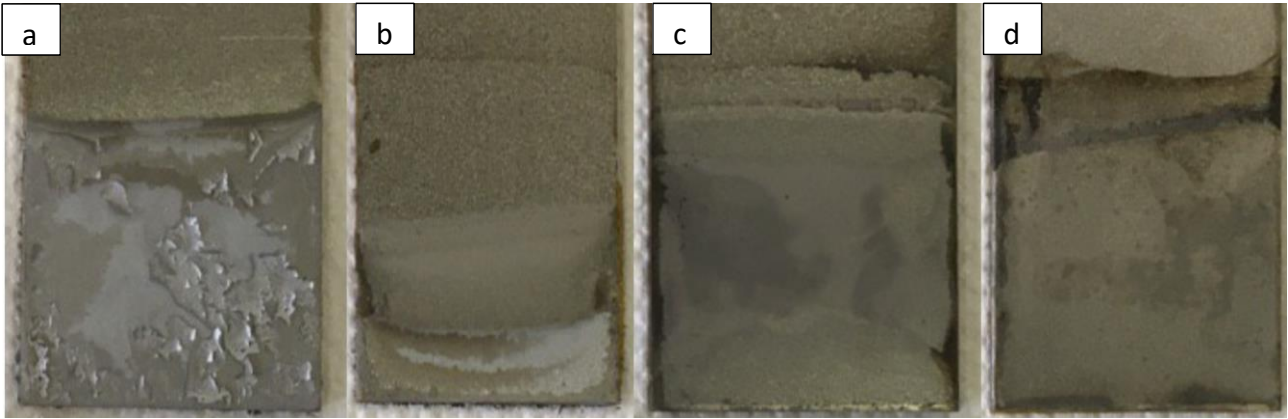
Figure 30. Effect of addition of concentrated HF 0.39A/cm^2 and 50°C . (a) 0%; (b) 2%; (c) 5%; (d) 10%. vol. Samples #4, 5, 6, 7.
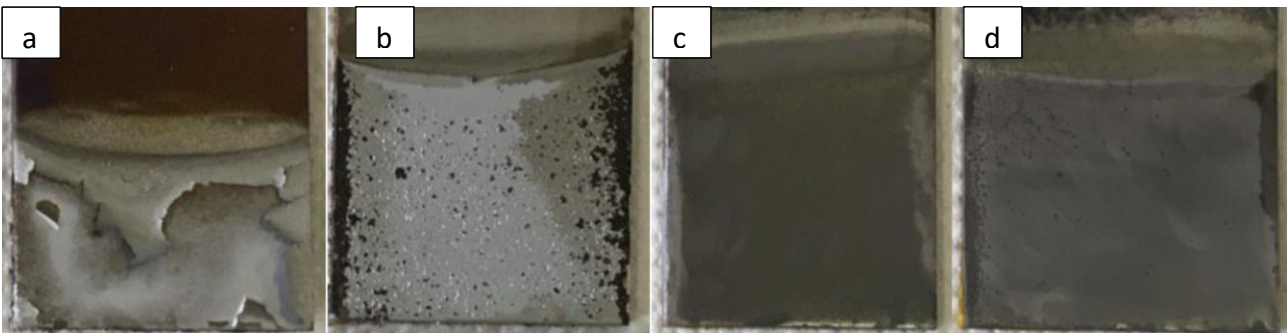
Figure 31. Effect of addition of concentrated HF 0.83 A/cm^2 and 50°C . (a) 0%; (b) 2%; (c) 5%; (d) 10%. vol. Samples #8, 10 – 5 μm, 11, 12.

Effect of activation

The samples #1-10 were done by following the procedure "etch, rinse and deposit". Overall, the quality of the coatings was poor (not adherent or absent). Thus, an activation step of the Ti substrate was introduced in procedure. The composition of the activation solution was taken from [29, 33]. The step was carried out in aqueous solution containing 18 g NaHF$_2$ with addition of 2 ml of H$_2$SO$_4$ (96%) per liter of solution, for 1 minute at room temperature. The aim of this step is to dissolve the surface oxides, making the substrate more reactive during the electroplating. According with [29,33,23], the formation of hydrides and fluorides on the surface prevent the diffusion of oxygen and thus, the formation of further oxides.

It is an interesting point to investigate the concentration of free fluorides in the solution as function of pH.

For a better understanding of the chemical equilibria that arise in this electrolytic solution, the content of free fluorides in a solution composed by water (H_2O), sodium bifluoride ($NaHF_2$) and sulfuric acid (H_2SO_4) have been computed.

The species in solution will be: H^+, HSO_4^-, SO_4^{2-}, HF, F^-, HF_2^-, Na^+ and OH^-.

For the calculations, the dissociation equilibria are taken into account (equilibrium constants at 25°C from [34]).

$$H^+ + F^- \rightleftarrows HF$$

$$K_1 = \frac{[HF]}{[H^+][F^-]} = 10^{3.14}$$

$$HF + F^- \rightleftarrows HF_2^-$$
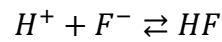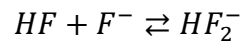
$$K_2 = \frac{[HF_2^-]}{[HF][F^-]} = 10^{0.74}$$

The fluorides are present both as free fluorides [F⁻] and in associated form [HF], [HF₂⁻]. The sum of these concentrations gives the total fluorides concentration $[F]_{tot}$:

$$[F]_{tot} = [F^-] + [HF] + 2[HF_2^-]$$

$$[HF] = K_1[H^+][F^-]$$

$$[HF_2^-] = K_2[HF][F^-]$$

Thus,

$$[F]_{tot} = [F^-] + K_1[H^+][F^-] + 2K_2K_1[H^+][F^-]^2$$

$$2K_2K_1[H^+][F^-]^2 + [F^-](1 + K_1[H^+]) - [F]_{tot} = 0$$

$$2K_2K_1 10^{-pH}[F^-]^2 + [F^-](1 + K_1 10^{-pH}) - [F]_{tot} = 0$$

Since the total fluoride content $[F]_{tot}$ is known (it comes from the amount of NaHF$_2$ added in the solution), by measuring the pH it is possible to establish the free fluoride content by solving the equation in $[F^-]$.
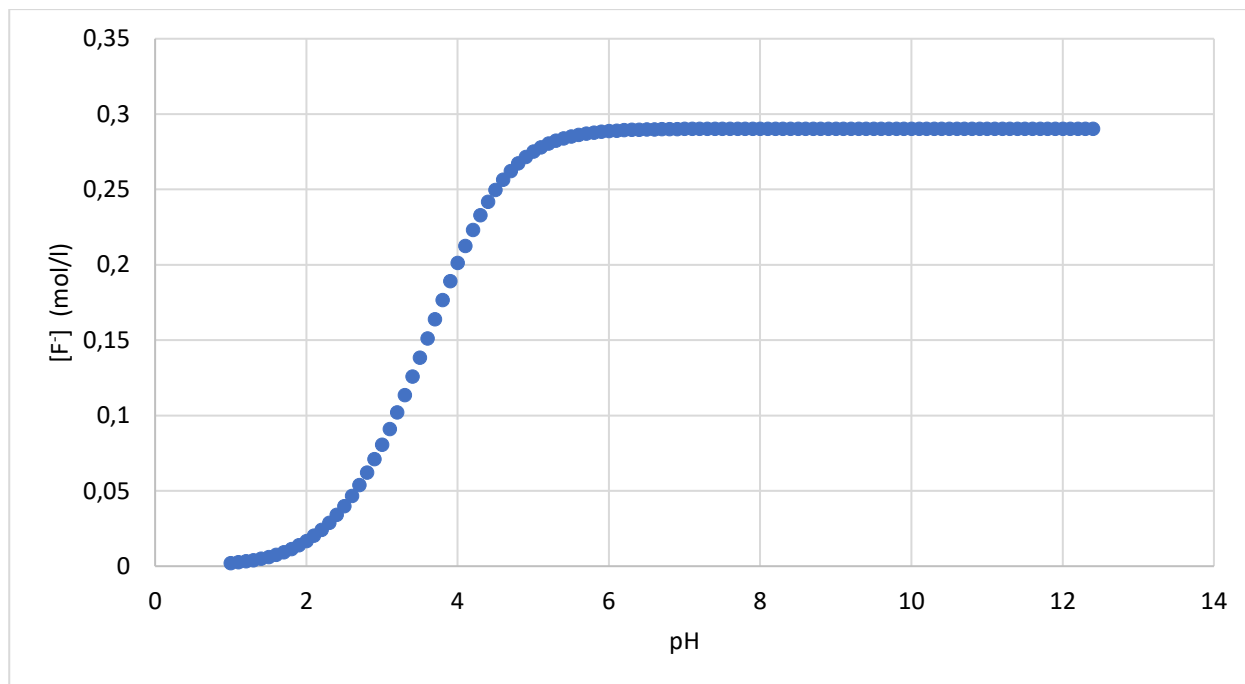
Figure 32. Plot of concentration of free fluorides as function of pH of the solution.

In our experiments the pH of the solution has been checked by pH test paper and it has a pH value around 4.

The effect of the activation step on Ti grade 1 is not naked eye appreciable. The appearance of untreated Ti is similar to that of activated Ti. On the other hand, the effect on Zr-1Nb is drastically different, as it is shown in **Figure 38**

Effect of current density

In order to exploit a wider current densities range, Hull cell experiments on Ti have been carried out. In three different experiments, Cr have been deposited onto three Ti panels in the Hull cell.

Each test was characterized with a different current applied (3, 6, 9 A). The results are showed in **Figure 33**.
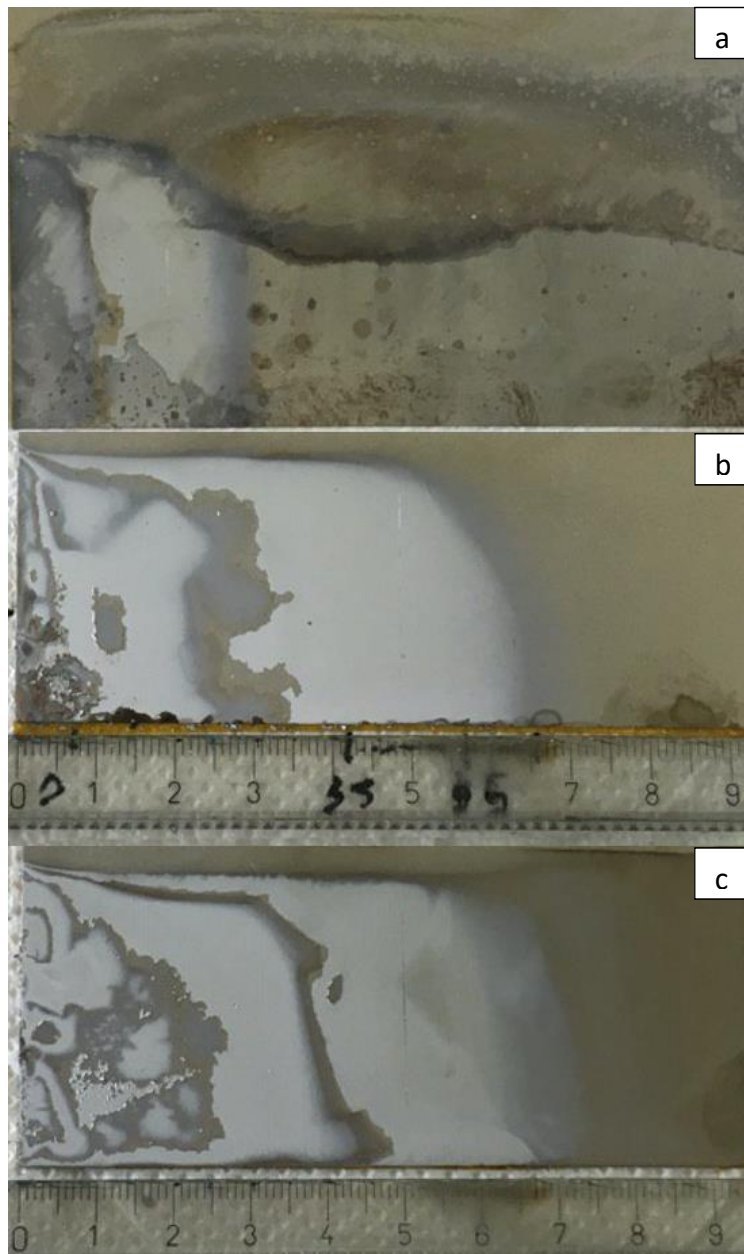
Figure 33. Result of Hull cell experiment (Cr onto Ti) with base bath at 50°C for three current values: (a) 3; (b) 6 and (c) 9 A. (highest c.d. on the left side).

According to the Hull cell formula, the optimal current densities (A/dm^2), determined by the coordinate L (cm) of the most adherent Cr region on Ti (respectively 2, 5 and 5.5 cm), in absence of fluoride at 50°C, for the three experiments are:

$$i_{(L)} = 3(5.1 - 5.24\ log\ 2) = 10.6\ A/dm^2$$

$$i_{(L)} = 6(5.1 - 5.24\ log\ 5) = 8.6\ A/dm^2$$

$$i_{(L)} = 9(5.1 - 5.24\ log\ 5.5) = 11.0\ A/dm^2$$

The high current density, near the left edge, cause cracks and spalling due to internal stresses. More-over, different regions (coordinate L) are characterized by different current efficiencies (repartition between Cr(VI) and H^+ reduction).

Effect of temperature

Deposition of Cr at 50°C from a solution (300 ml) containing 1.75 g HF (38-40%) has shown a non-uniform white deposit only at the edges and in the central region of the sample (**Figure 34**).
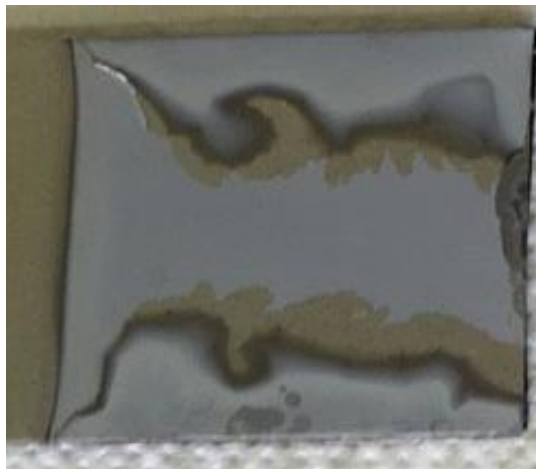
Figure 34. Cr layer deposited on Ti from base solution (300 ml) containing 1.75 g of HF (38-40%) at 50°C for 10 min at 0.4 A/cm². (sample #18).

From the same electrolyte, Cr coating deposited at room temperature are adherent with a gray dull appearance. As described below, this result is important for the further depositions (**Figure 35**).
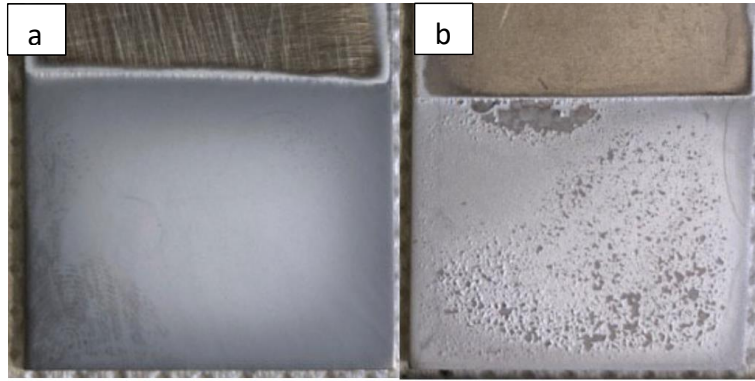
Figure 35. Cr coatings deposited on Ti from base solution (300 ml) containing 1.75 g of HF (38-40%) for 10 min at 0.23 A/cm^2 at (a) room temperature; (b) 42°C (sample #44 and 44.2)

According to the results at room temperature, it was decided to combine in one cycle two electro-depositions steps (double chromium): 1) deposition at room temperature for few minutes, followed by 2) a progressive increase in the temperature of the solution until 50°C (**Figure 39**). The resulting coating is the combination of two layers, the first that is adherent to the substrate and the second that is bright with uniform and compact structure (**Figure 36**).
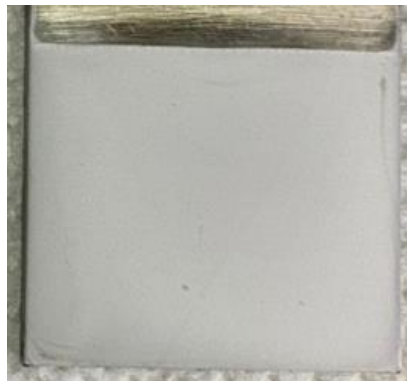
Figure 36. Cr layer deposited in electrolyte containing 1.75 g HF (38-40%) following the temperature profile illustrated. I=0.21 A/cm^2 (sample #54).

Tests onto Zr-1Nb

Until now, the experiments regarded the Ti substrate.

A procedure to deposit adherent Cr coating onto Ti has been developed, but since the Zr-1Nb sample are smaller, the different current density distribution on the samples caused issues.

Figure 37. Effect of high current density on Zr-1Nb samples in presence of fluorides.

XRF analysis showed that a non-uniform thickness distribution was present, for 1h-plating in the based electrolyte containing 1.75 g HF (38-40%), a thickness of 10 μm was deposited on the central part of the samples, while in proximity of the corners it reached 20 μm (**Figure 37**).

In order to make more uniform the current distribution on the cathode surface, a mask was realized (**Figure 79**).

Electrodeposition procedure to deposit Cr on Zr-1Nb alloy

The optimized procedure for electrodeposition on Ti, and applied to Zr-1Nb (E110), consists in:

1. substrate degreasing with acetone or ethanol to eliminate organic contaminations;
2. sandpaper treatment (SiC grit 100) (it can improve the adhesion as suggested from [29]);
3. connecting the Zr-1Nb substrate onto the Ti sample holder (**Figure 79**);
4. chemical pickling for 3-4 min in an aqueous solution containing 10% vol. HNO_3 (65%) and 10% vol. HF (38-40%) at room temperature;

78

5. rinsing with distilled water;

6. activation for 1 min in 1 l solution containing 18 g $NaHF_2$ and 2 ml H_2SO_4 (96%) at room temperature; activated Zr alloy appears as a black layer (**Figure 38**).

Figure 38. Activated Zr sample (black region).

7. rinsing with distilled water;

8. electrodeposition at room temperature, by using sample holder with mask, for 8-10 min with a current density of 0,21 A/cm^2 (cell voltage 3-3.5 V) in a bath containing 75.9 g CrO_3 + 0.6 ml H_2SO_4 (96%) + 1.75 g HF (38-40%) + distilled water (balance to 300 ml); (deposition on both surfaces, with a cathode-anodes distance of about 4 cm).

9. rising the temperature at 50°C with the following temperature profile and keep the temperature constant until the deposition ends (**Figure 39**);

10. rinsing with distilled water.
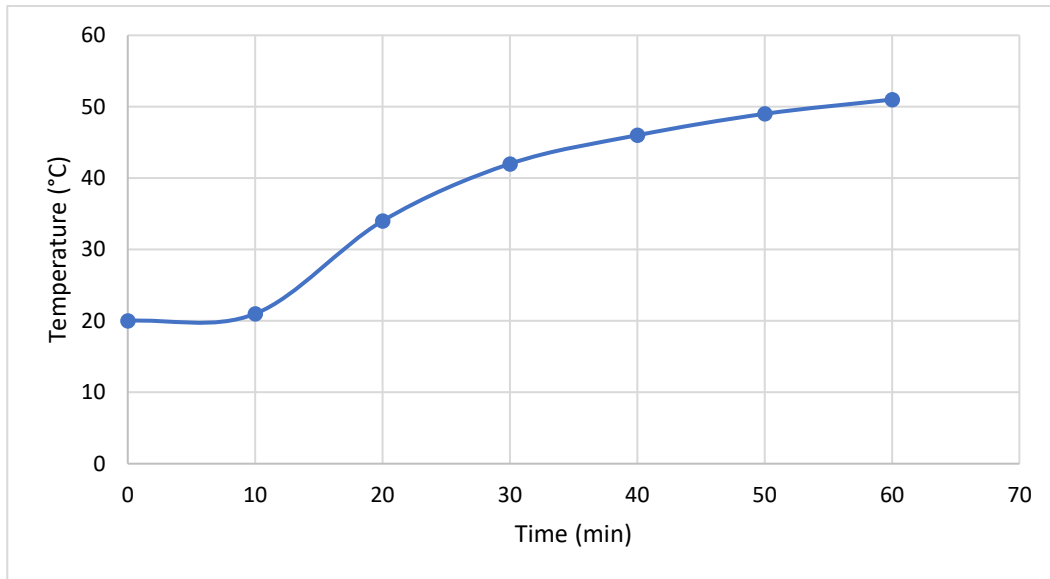
Figure 39. Characteristic temperature profile during 1-hour electrodeposition of Cr onto Zr-1Nb alloy.

Figure 40 shows the final result of the electrodeposition of Cr onto Ti and Zr-1Nb. Further post-treatments for hydrogen degassing or diffusion of Cr into Zr-based alloys are suggested [35,24,22]. In literature the best results were obtained when specimens, after the deposition, were heated at 700 °C for 1 hour in order to promote the Cr diffusion into the Zr-Nb substrate [29].
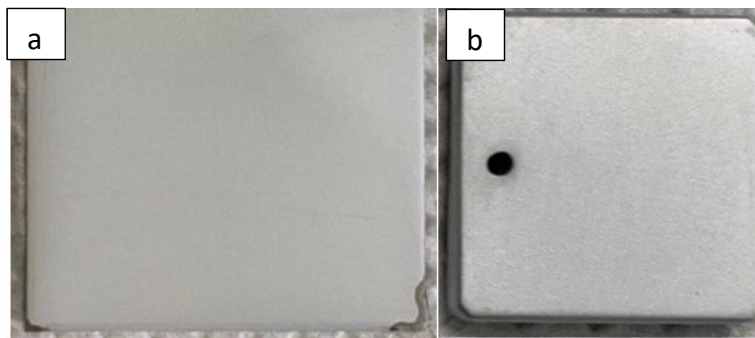
Figure 40. Ti (a) and Zr-1Nb (b) samples coated with Cr following the procedure explained above (#55, 59).

As for Ti, the changing in temperature effects the current efficiency since at cold temperature the deposition rate is experimentally higher than high temperature. The cold Cr result shows a higher thickness (35 µm) than the double Cr (18 µm).

Figure 41. Cold chromium plated sample on the left (35 µm thick), and chromium plated following the procedure described below on the right (18 µm thick). Both the deposition processes lasted 75 minutes on Zr-Nb samples.

By using the procedure described above, the following samples have been prepared:

Table 3. Samples prepared with the procedure discussed above and relative current efficiency.

Sample (#)	Time (s)	Thickness (um)	Efficiency (%)
70	4500	35	29
67	3600	20	21
68	3600	15	16
69	3600	15	16
71	4500	15	13
73	4500	22	19
74	4200	17	15
75	3600	11	12
76	3600	18	19
77	3600	12	13
78	3600	12	13
79	3600	14	15
80	3600	15	16
81	3600	11	12
82	4200	17	15
84	2400	8	13
85	2400	10	16
87	2400	12	19
88	3600	6	6
89	5400	20	14

Only for the sample #70 the temperature was constant, other samples were subjected to a temperature profile. This confirms that the process is depositing two different Cr layers with two different internal tensile stresses. The Cr deposited at lower temperature is less stressed and thus, it results more adherent.

Magnetron-deposited Cr coatings

Other samples were prepared by depositing Cr by magnetron sputtering in TPU laboratories and these are used to make a comparison.

The parameters of the magnetron depositions onto Zr-Nb based alloy are listed in the

Table 4.

For the study, deposition mode Cr-60 was used for deposition Cr onto the corners. Magnetron sputtering at the modes of Cr-59, Cr-61 and Cr-62 was elaborated for chromium deposition onto Zr-1Nb pieces.

Dual magnetron sputtering system was used during the deposition of Cr-59, Cr-60 and Cr-61, while for the deposition of Cr-62 a three-magnetrons system was employed to increase the deposition rate.

Table 4. Operating parameters of magnetron sputtering depositions.

	Cr-60 corner	Cr-59 thin	Cr-61 medium	Cr-62 thick
P_1 (W)	2500	2500	2500	2500
P_2 (W)	2500	2500	2500	2500
P_3 (W)	-	-	-	2500
V_1 (V)	840	817	785	758
V_2 (V)	714	730	705	678
V_3 (V)	-	-	-	655
I_1 (A)	4.41	4.50	4.50	4.80
I_2 (A)	4.67	4.63	4.65	4.62
I_3 (A)	-	-	-	3.80
Time (min)	64	192	284	256
Temperature (°C)	215	215	215	215
Thickness (μm) *	1.3	4.5	6	8.2
Pressure (Pa)	0.21	0.21	0.21	0.21
Ar inflow (SCCM)	21	22.5	22.5	22.5

*Thickness evaluated by analysis of SEM images.

To deposit adherent Cr coatings, special pretreatment was used. Firstly, higher bias was used for 2 min. Other parameters are voltage of 600 V, current of 0.2 A (pulse frequency 100 kHz, duty cycle 70%). Then, during coating deposition, bias parameters were 100 V, 0.19-0.23 A (pulse frequency 10 kHz, duty cycle 70%).

Before the deposition, the sample have been etched in Ar plasma for 30 min (0.15 Pa). For this process, an ion source with closed electron drift has been used.

The temperature of substrate during the processes was very similar, around 215°C. This explains that the overall process parameters were almost equal during the deposition modes, and the process had a good reproducibility.
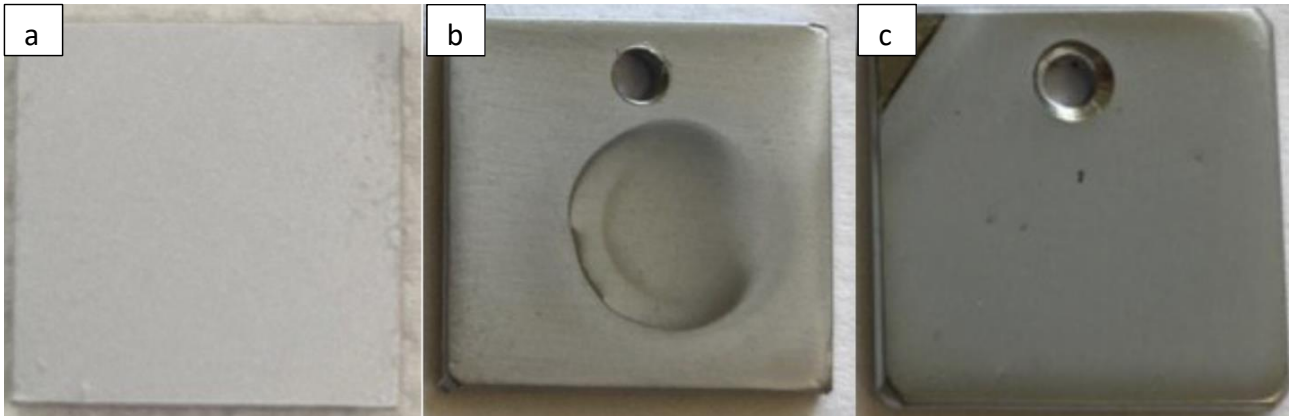
Figure 42. Initial outer view of (a) electrodeposited coating; (b) corner deposited by magnetron; (c) magnetron deposited (on the right) Zr-1Nb samples.

Properties of as deposited Cr coatings

Crystal structure

From the XRD analysis of the electrodeposited sample, it is evident only the metallic Cr body - centered cubic (BCC) pattern. Due to thick Cr coating, it is not possible to find peaks from Zr based substrate.
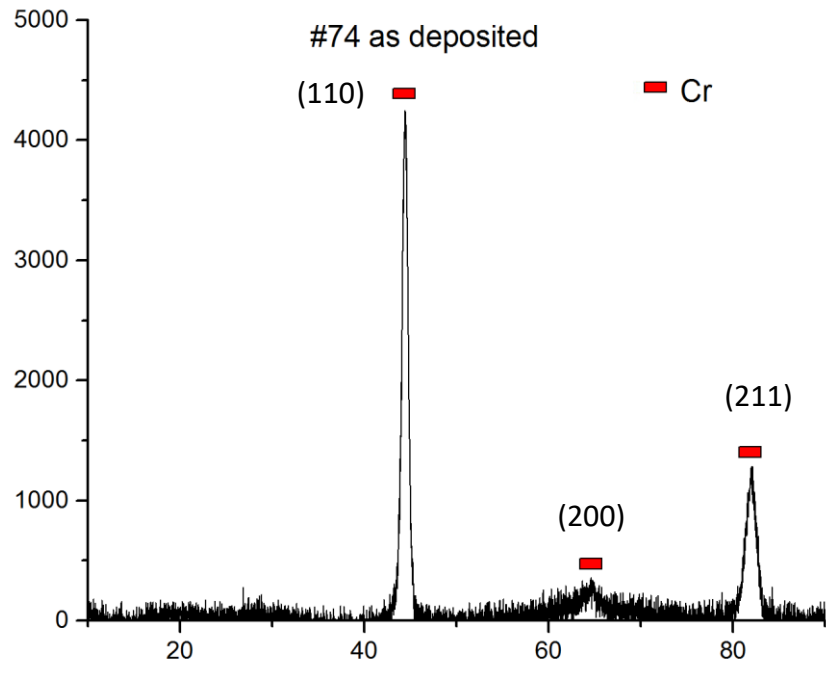
Figure 43. XRD spectrum of electrodeposited sample #74 – 17 μm.
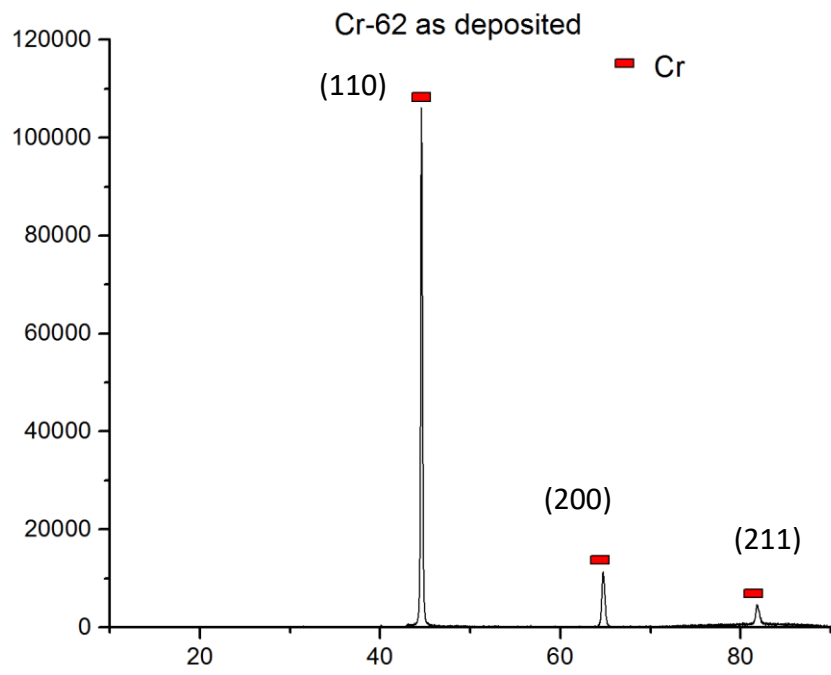
Figure 44. XRD spectrum of magnetron deposited (Cr-62 – 8.2 μm)

No other elements or phases are observed in the magnetron-deposited spectrum.

The relative high intensity of the signal of the peak at 44° means that the magnetron coatings have been deposited pronominally oriented along the (110) direction. For galvanic samples this is different, since the intensities are more comparable.

Microstructure

The microstructure of the deposited coating is significantly different according with the deposition technique used during the process. The coating deposited by magnetron result more compact with a clean interface between Zr-1Nb substrate and metallic Cr (**Figure 45**). This coating microstructure is attributed to using of special pretreatment before coating deposition (high substrate bias during 2 min) and apply pulsed bias during coating growth (-100 V). Both approaches positively result in good coating adherence and compact microstructure.
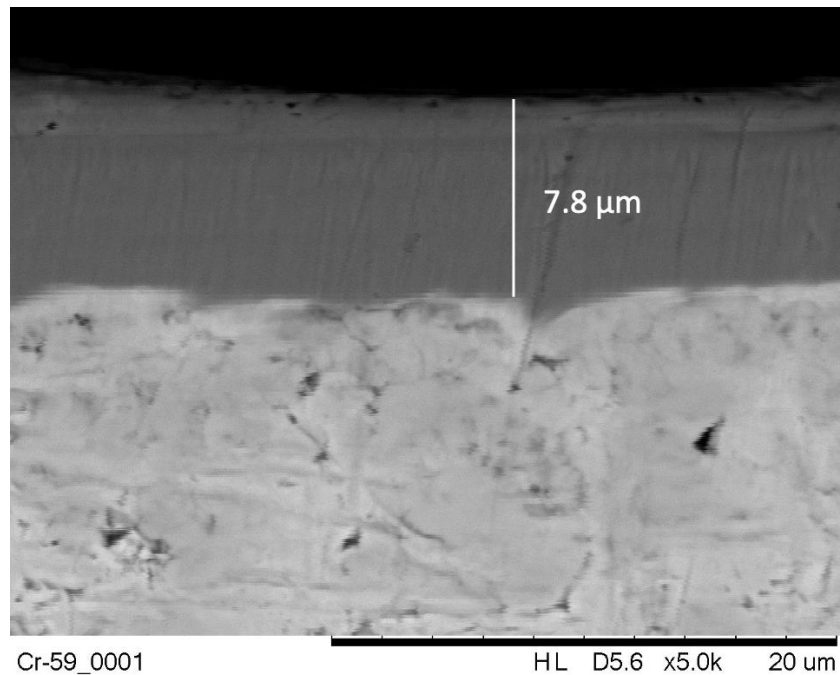
Figure 45. SEM image of magnetron deposited Cr (sample Cr-59 – 4.5 μm) on Zr-Nb before oxidation test.

While, the coating electrodeposited shows a less compact structure. In particularly, it shows a porous layer at the interface between Zr-Nb substrate and metallic Cr. It is due to the activation process in order to improve the adherence during the deposition. This structure introduces a new interface (and defects) that can influence negatively the adhesion of the coating.

14.4 μm

8.5 μm

Cr-79_0000   H   D12.2 x1.0k   100 um
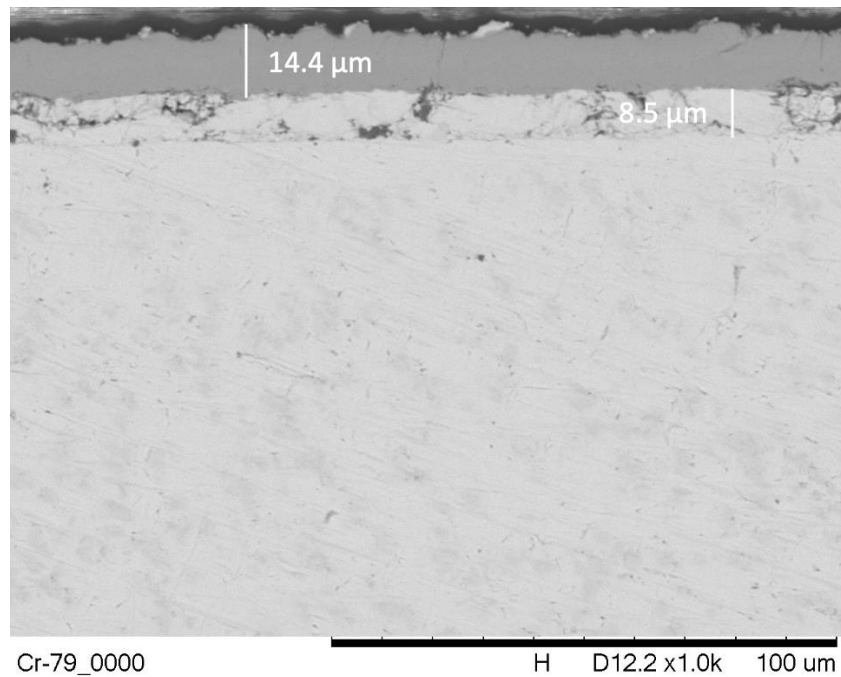
Figure 46. SEM image of electrodeposited Cr (sample #79 – 14 μm) on Zr-1Nb before oxidation test.

GDOES of the as-deposited Cr coatings by electroplating

During conventional chrome plating processes, a detrimental side effect occurs: hydrogen occlusion. Hydrogen can penetrate into the substrate and causes embrittlement of the metal part with subsequent reduction of mechanical properties [30]. Zr-based alloys can absorb large amounts of hydrogen and thus embrittle considerably.

In this case, we supposed that hydrogen can be absorbed also during etching and activation steps. Most conventional chrome plating control documents, therefore, specify a degassing thermal treatment to remove hydrogen gas.

The longer the plating cycle, the more likely it is that hydrogen embrittlement will occur. Embrittlement is also more likely to occur after an acid clean. Shot peening and/or liquid honing can be used to relieve embrittlement stress [35].

From GDOES analysis is clearly visible the presence of hydrogen at the surface of the sample and at the interface between Cr and Zr-Nb based alloy.
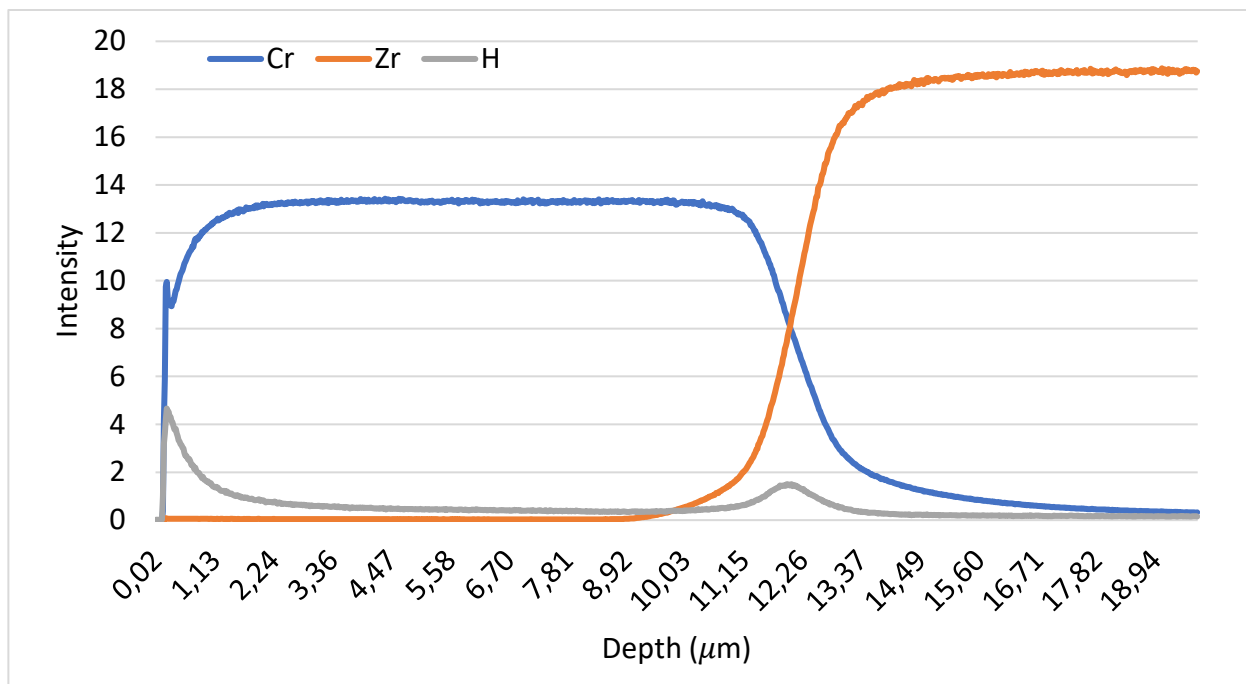
Figure 47. GDOES profile of electrodeposited sample (#78 – 12 μm) before oxidation.

The presence of hydrogen at the sample surface can be related to absorption of water and other impurities during the pretreatment procedures before GDOES test.

The hydrogen at the interface between Zr-Nb substrate and metallic Cr. This hydrogen may be due to the etching and the activation of the samples before the deposition or it can be also due to the electrodeposition itself.

However, the Cr coatings have low hydrogen permeability and the galvanic process is realized at low temperatures (20 - 50°C), the absorption and diffusion of hydrogen are strongly limited into Cr-coated Zr sheets, thus hydrogen can be only at the interface area.

Other main point is good correlation of as deposited coatings thicknesses by XRD and GDOES instruments. Both techniques show that coating thickness is equal to 12 μm.

Adhesion test

During the adhesion tests, no spalling was observed on the Cr magnetron deposited. The instrument shows a very low acoustic emission of magnetron-deposited samples compared to the

electrodeposited ones (about one order of magnitude lower). This may be a consequence of the more compact structure of as result of the vacuum technique, while regarding the electroplated samples, some spalling phenomena were observed during the adhesion test. Moreover, the coating cracking and spallation are obviously observed during the drilling process at the stage of sample preparation.
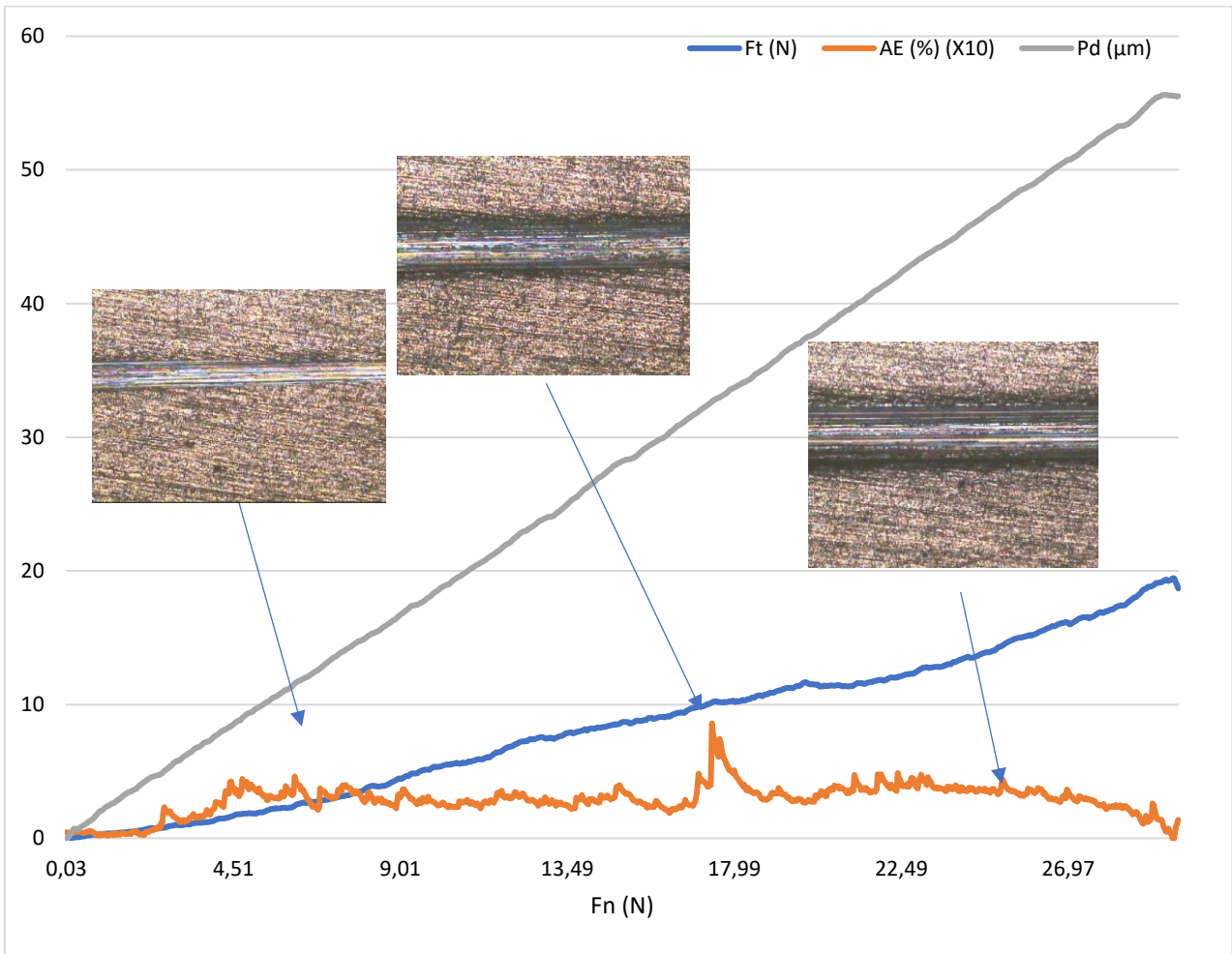
Figure 48. Adhesion test of magnetron deposited Cr (sample Cr-59). The signal of AE is increased in 10 times.
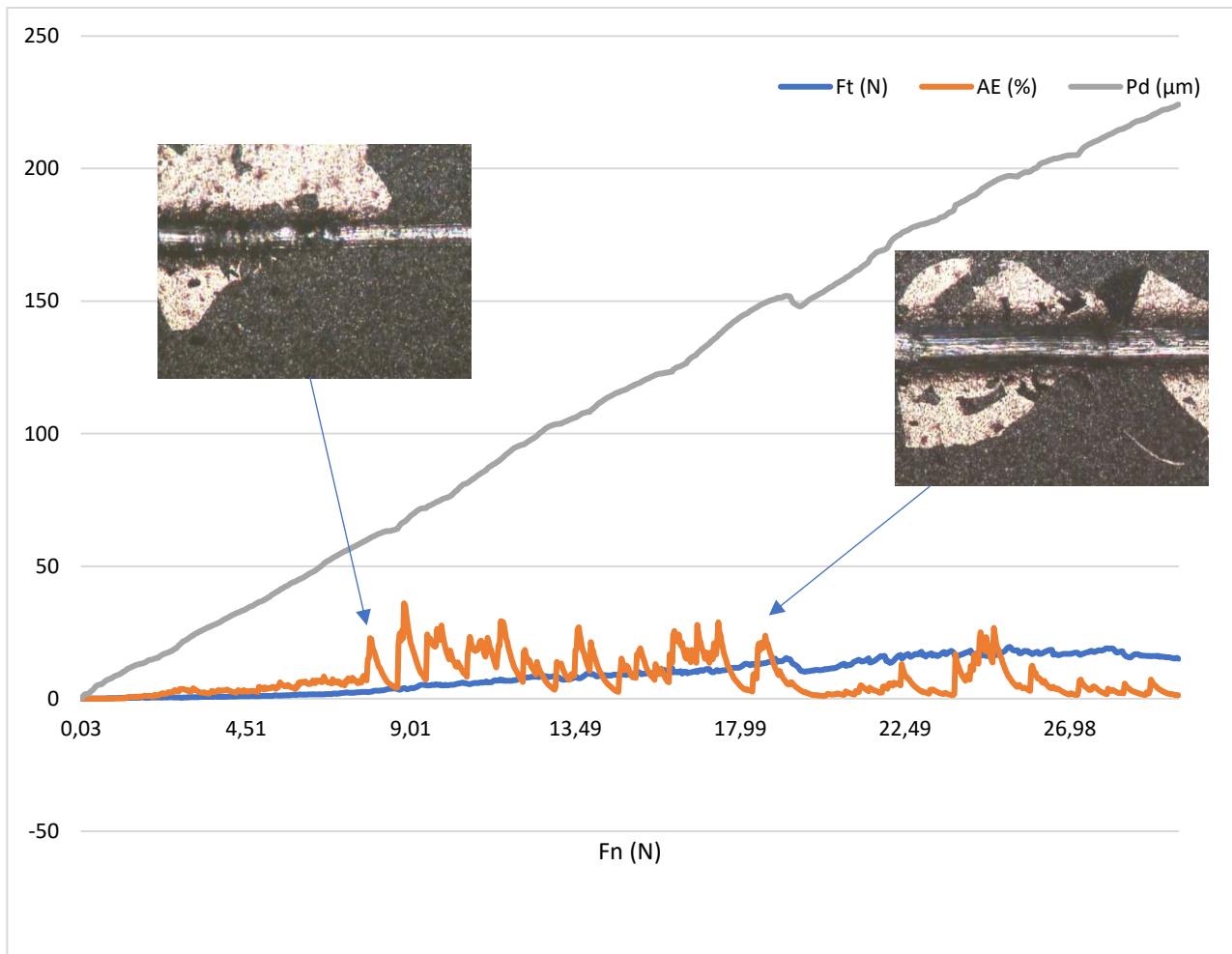
Figure 49. Adhesion test of electrodeposited Cr on Zr-Nb (sample #79 – 14 μm).

The coatings thickness did not influence the adherence of Cr to Zr-1Nb substrate. From **Figure 81** to **Figure 84**, in the **APPENDIX**, there is shown that 4.5-8.2 μm-thick Cr coatings by magnetron sputtering and the samples with the Cr thickness of 5-18 μm have the similar adhesion behavior independence on their thickness.

OXIDATION TESTS

For qualitative analysis of the sample behavior in oxidation tests, each sample (coated and pure Zr-1Nb sheets) was necessarily photographed before and after test. The outer view of the samples is shown in **Table 10** in **APPENDIX**. There is obviously presented that pure Zr based samples are strongly oxidized in atmosphere or LOCA conditions. White-colored films are ZrO_2 that can be

spalled even during the test. Opposite situation is found for the Cr-coated samples. The most samples saved their preservation and colored by dark-green and blue. Such colors are indicated (1) the oxidation of Cr coatings onto the Zr sheets and (2) coatings are adherent even after oxidation test and thermal shocks.

The results of analytical measurements of oxidized samples are presented below. Firstly, the samples after atmosphere oxidation are discussed, then – LOCA conditions.

High temperature atmosphere oxidation test

Three electrodeposited samples (with corners deposited by magnetron), three magnetron deposited samples and one uncoated Zr-1Nb samples have been subjected to oxidation test at high temperature in natural atmosphere environment (with the presence of O_2 and N_2). The temperature profile of this experiment is indicated in **Figure 27**.
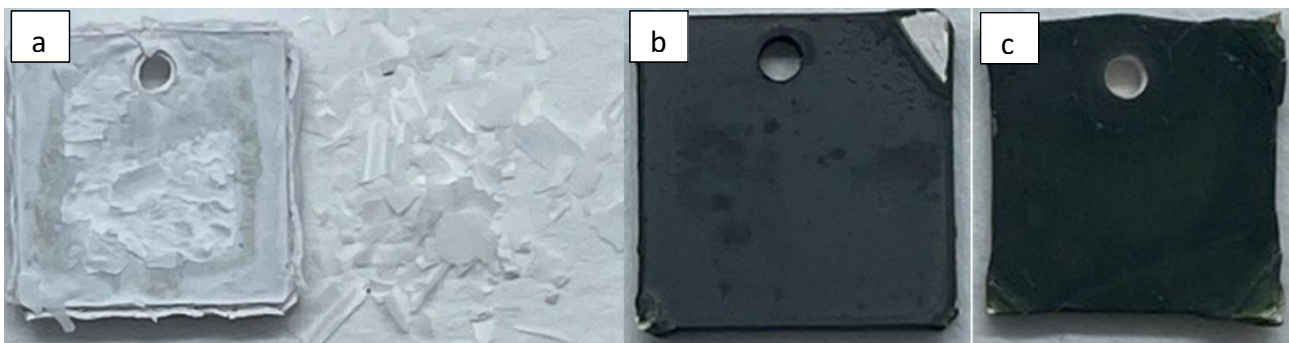
Figure 50. Outer view results after oxidation test in atmosphere environment. (a) Uncoated; (b) Magnetron-deposited; (c) Electrodeposited.

Gravimetry measurements have been carried out before and after the oxidation and the weight gain of each has been analyzed considering its covered and uncovered geometry. By knowing the oxidation rate of the uncoated Zr-1Nb sample, it is possible to compute the oxidation rate for each coated sample. To calculate the mass gain of the samples, the procedure described in "**Gravimetry test**" section was used. **Figure 51** shows the mass gain of the samples after atmosphere oxidation.
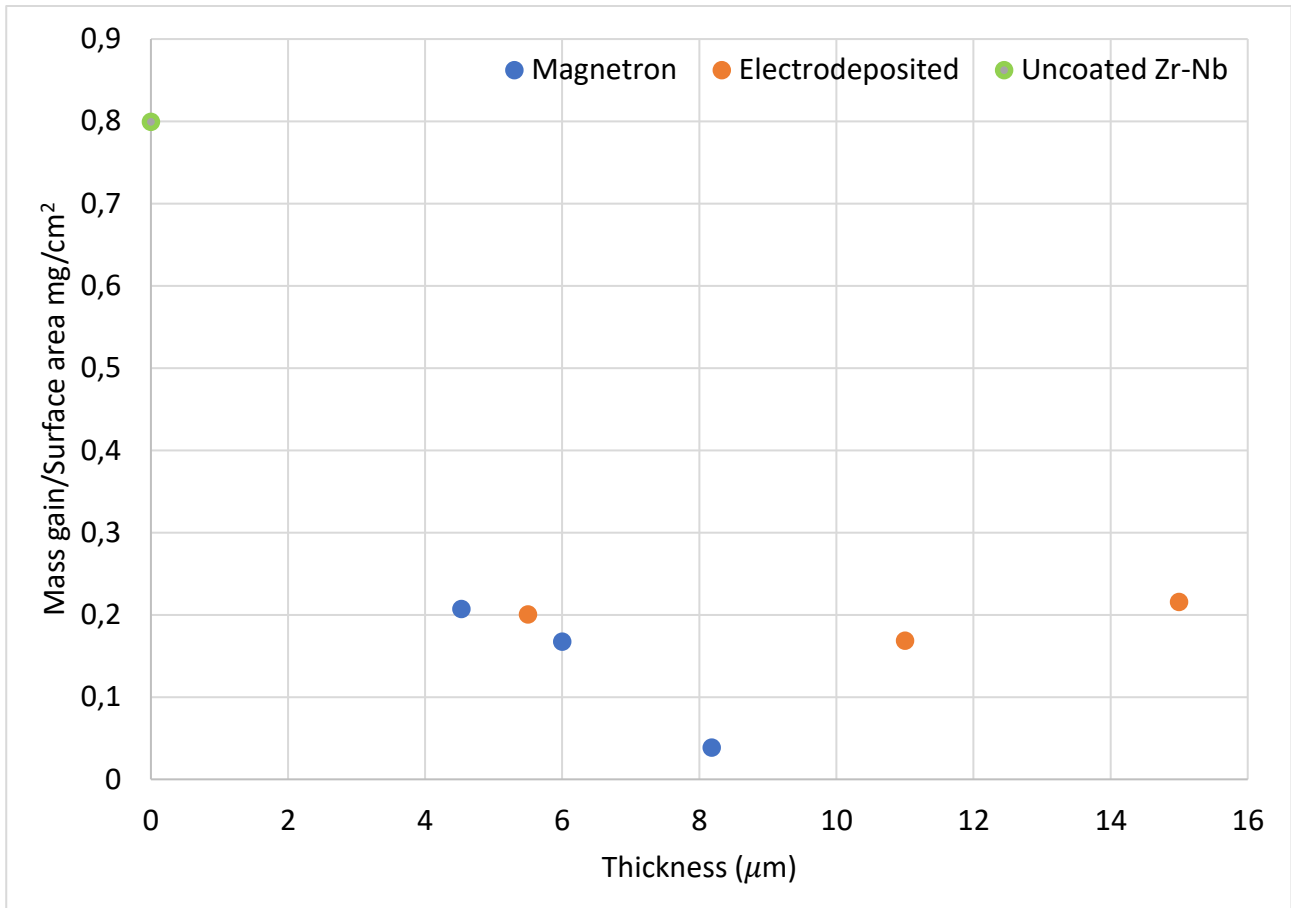
Figure 51. Gravimetry result of oxidation test in atmosphere environment.

The samples coated (both by magnetron and electrodeposited) show a better corrosion resistance behavior if compared to the uncoated Zr-1Nb sample, in particular, they weight gains are minimally about four times lower. Moreover, for magnetron samples is clear how the thickness of the coating influences the corrosion resistance: the weight gain due to the oxidation decreases almost linearly by increasing the thickness of the Cr coating. About the electrodeposited samples, this relation is not clear, probably some defects present in the samples (such as on its corners) caused a higher oxidation rate of the material, making the result incomparable with the others. The best result is found for the magnetron coating (Cr-62) with the thickness of 8.2 μm. It is in 10 times lower than uncoated Zr-1Nb sheets. The analysis of the mass gains of the samples show that magnetron samples (4.5-8.2 μm) have better protective properties even for lower thickness in comparison with thicker (5.5-15.0 μm) electroplated coatings.

Figure 52 and **Figure 53** show the XRD patterns of the thinnest samples (magnetron and galvanic deposited) after atmospheric oxidation. Here, it is good to notify that the as-deposited Cr coatings were oxidized at 1100°C in a natural atmosphere.

Both, magnetron and galvanic coatings, had similar crystal composition after oxidation. The found phases were Cr_2O_3, initial BCC-Cr phase, CrN and Cr_2N, interface of Cr_2Zr, ZrO_2 and Zr_3O (α-Zr(O) phase). The presence of these phases is related to oxidation of Cr coatings at high temperatures and oxygen diffusion into Zr sheets. When a residual Cr layer is present, the formation of ZrO_2 phase can be explained by higher affinity of Zr to oxygen (forming zirconia in comparison with chromia). More-over, at high temperatures Cr and Zr can diffuse and the Cr_2Zr interlayer grows. An interesting point is that CrN and Cr_2N phases could be due to re-oxidizing mechanism of ZrN layer to ZrO_2, and to the interaction of newly available nitrogen with residual Cr. Such mechanism is suggested in the earlier published study [36].

However, according to the XRD patterns of thicker samples after atmosphere oxidation, the intensities of ZrO_x and CrN_x phases are strongly decreased or they disappeared with the coating thickness (**Figure 117**, **Figure 120**, **Figure 125**, **Figure 126** in **APPENDIX**). This fact is more pronounced for the magnetron deposited coatings. Mainly, it is related with higher absorption of X-ray by thick Cr_2O_3 and residual Cr layers. Thus, for the future analysis of oxidation resistance of Cr-coated samples, other analytical instruments were used.
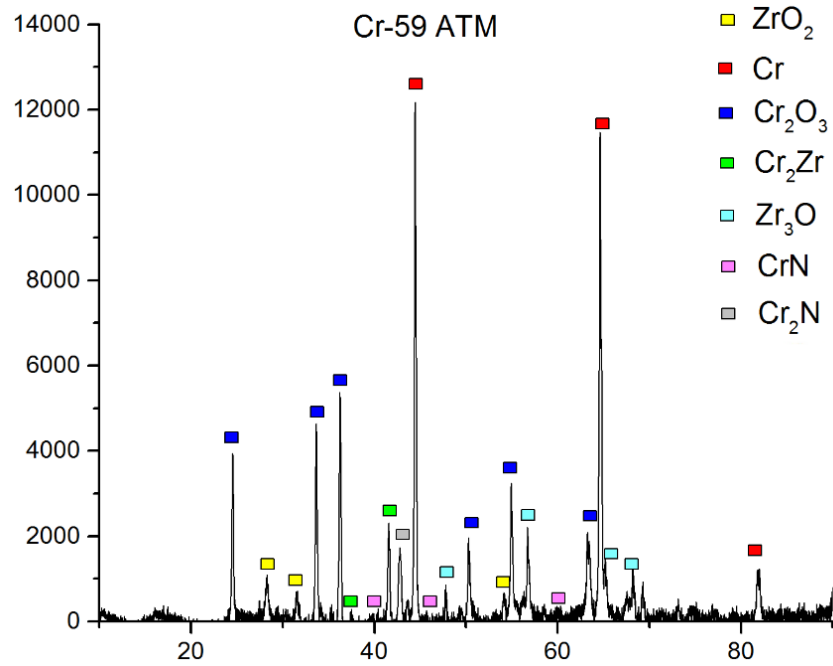
Figure 52. XRD spectrum of oxidized Cr coating (sample Cr-59 – 4.5 μm) deposited by magnetron sputtering in atmosphere environment.
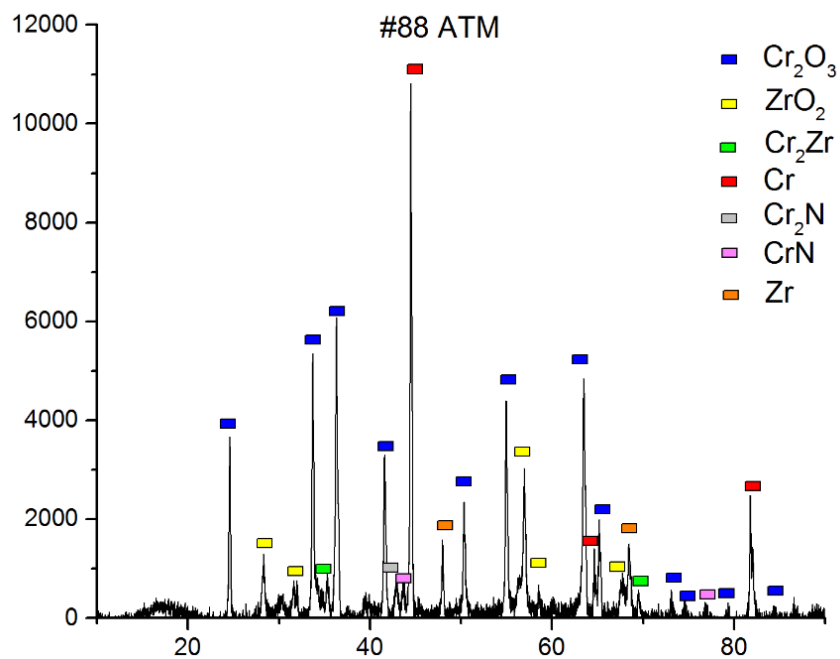
Figure 53. XRD spectrum of oxidized Cr coating (sample #88 - 6 μm) deposited by electroplating in atmosphere environment.

Figure 54 shows the cross-section of uncoated Zr-Nb alloy after atmospheric oxidation test. There is clearly shown that the sample is destroyed under these oxidation conditions. The presence of thick oxides and nitrides layers is found by optical microscopy. According to the data the thickness of ZrO_2 can be up to 850 μm, ZrN 85 μm, α-Zr(O) 40 μm and the remaining part of the material is in prior β-phase with interbedded α-Zr(O) grains. The uncoated sample after oxidation show a really thick (>800 μm) layer of ZrO_2 (black part in **Figure 54**). The coatings, both magnetron and electro-deposited, protect the Zr from the oxidation, since no ZrO_2 is detected by optical microscopy or SEM. In the optical microscopy image of uncoated sample (**Figure 54**) the presence of α-Zr(O) is clearly notable, it appears as a white layer between the β-Zr and the ZrN. Regarding the coated samples, only the thinnest electroplated sample show the presence of α-Zr(O), the other galvanic or magnetron coatings are enough protective and they have the capability to avoid the oxygen penetration during atmospheric oxidation test. Moreover, the optical microscopy shows also that ZrN is present only on uncoated Zr-1Nb alloy, while for deposited coatings only the Cr layer is visible.

Analysis of the obtained results indicates the strong effect of nitrogen on oxidation and degradation of Zr alloys at high temperatures (**Figure 54**). In an uncoated zirconium alloy, a non-uniform ZrO_2 layer is observed. Nitrogen can interact with α-Zr alloy that results in the formation of ZrN phase. The latter phase becomes embedded in the oxide matrix during further oxidation stage and then can be re-oxidized by newly available oxygen. The difference in the molar volumes of ZrN (14.8 cm^3) and ZrO_2 (21.7 cm^3) is significant, so the phase transformation of ZrN → ZrO_2 occurs with a volume increase of 47% that is the source of high compressive stresses. The stress relaxation can lead to generation of cracks and finally formation of porous oxide layers. Cracking of ZrO_2 layer during the re-oxidation stage also results in non- uniformity of the oxide layer due to enhanced oxidation and destruction of zirconium alloy along the formed cracks [36].

Due to low solubility of N in chromia, nitrogen can diffuse through the outer oxide layer (Cr_2O_3) mainly along the grain boundaries and defects to the metal where it can stabilize the α-Zr phase or react with the α-Zr to form the ZrN phase. Then, the re-oxidation process can occur like the uncoated alloy [36].
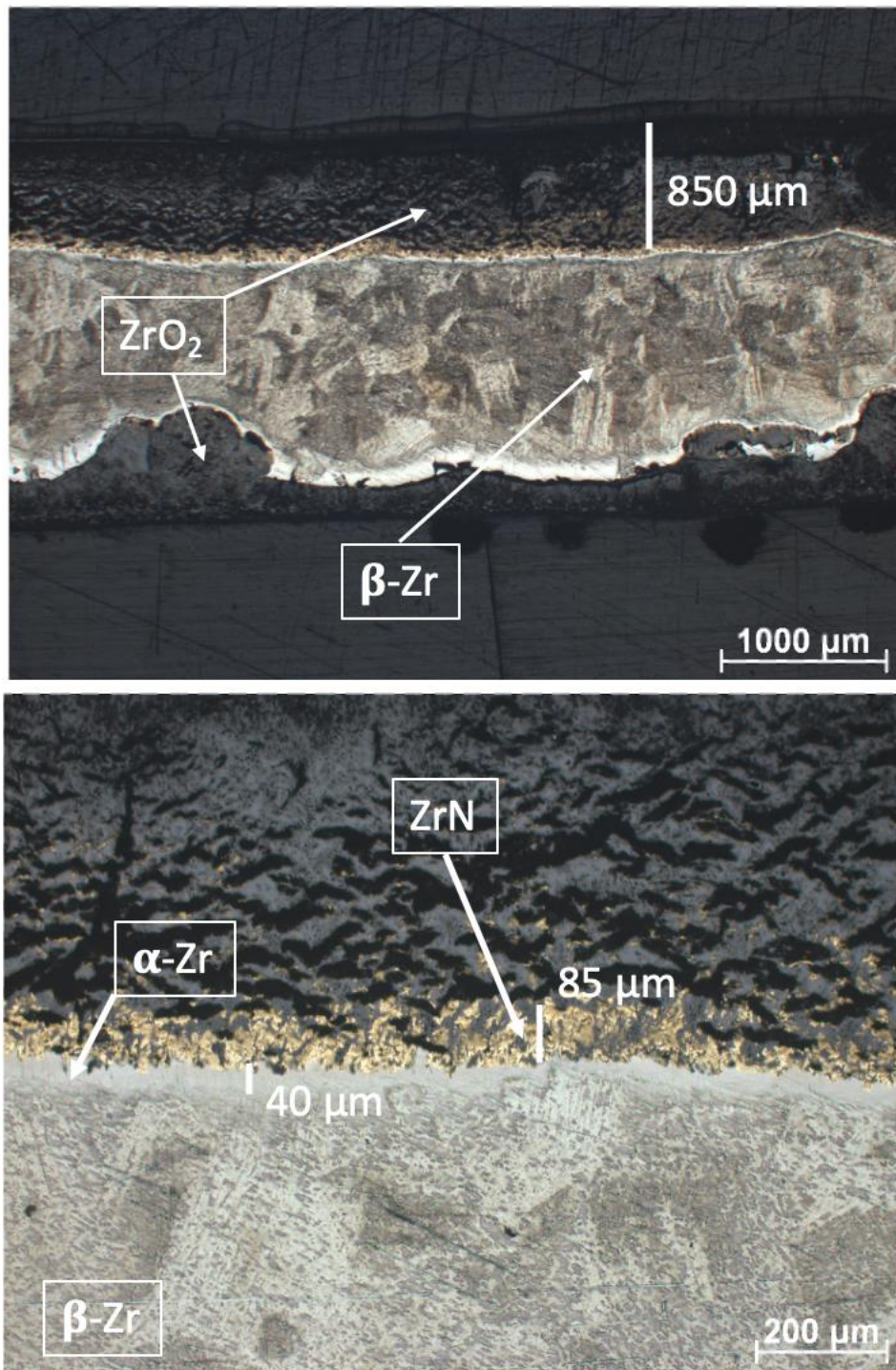
Figure 54. Optical microscopy images of uncoated Zr-1Nb sample after oxidation in atmosphere.

An important observation is that the SEM image of cross-section of magnetron coating Cr-62 (**Figure 56**) shows a well separated layers structures: starting from the top, the notable layers are Cr_2O_3, metallic Cr, Cr_2Zr and β-Zr. Differently from magnetron, the galvanic coating has been destroyed

during the test, there is no possibility to distinguish the layered structure. There is no presence of black ZrO_2, while the presence of α-Zr is visible in **Figure 94**. It is possible that the gravimetry test of electrodeposited sample has been influenced by such spalling.
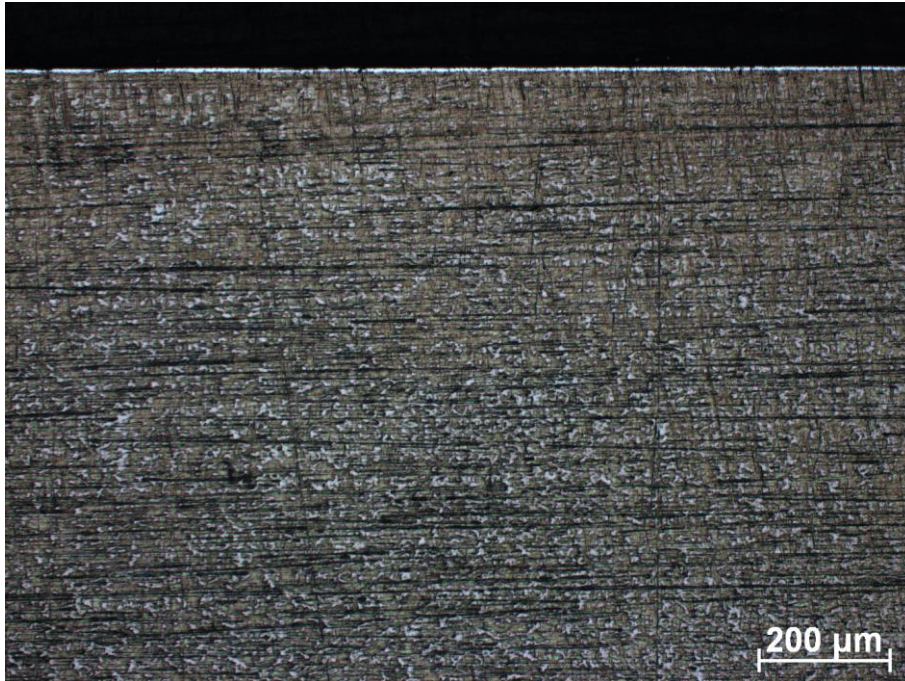
Figure 55. Optical microscopy image of magnetron-deposited sample (Cr-62 – 8.2 µm) after oxidation test in atmosphere.
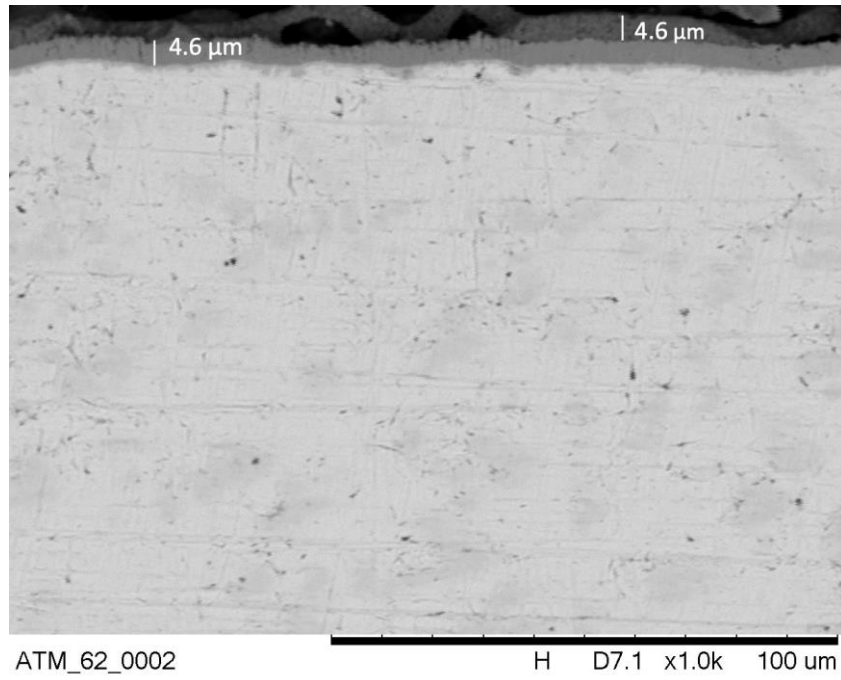
Figure 56. SEM image of magnetron-deposited sample (Cr-62 – 8.2 μm) after oxidation test in atmosphere environment.
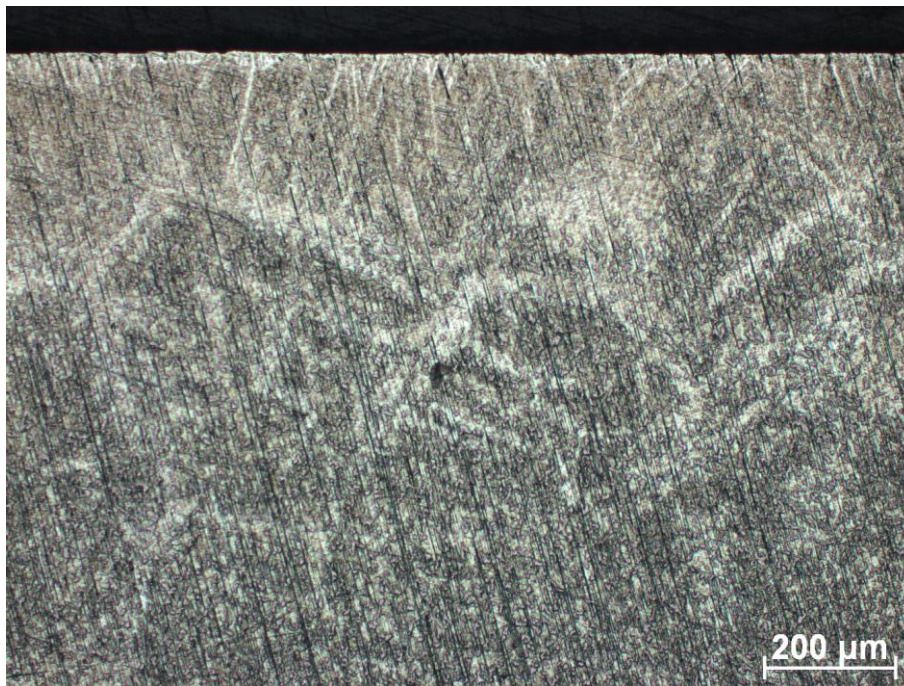
Figure 57. Optical microscopy image of electrodeposited sample (#81 – 11 μm) after oxidation test in atmosphere.
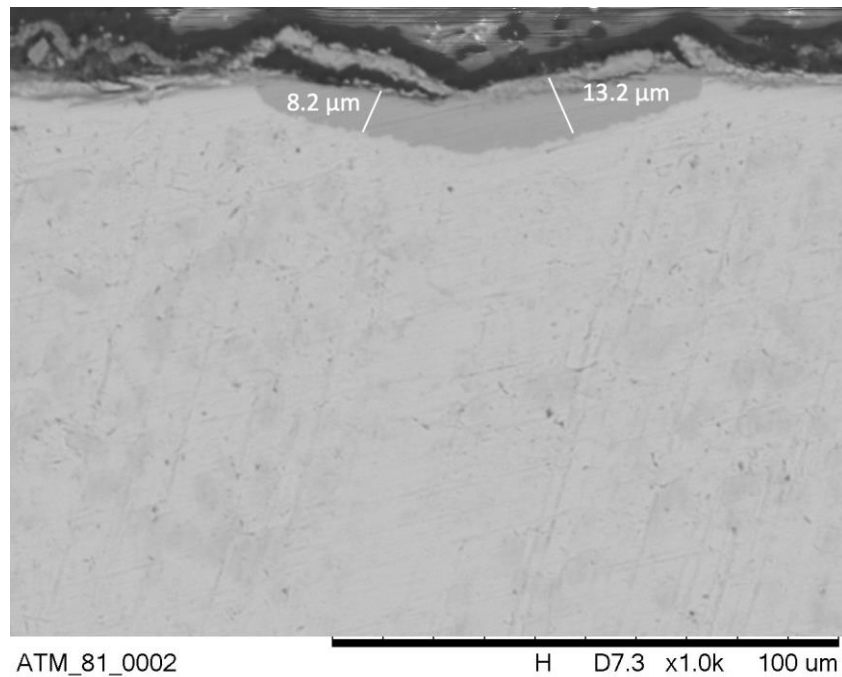
Figure 58. SEM image of electroplated sample (#81- 11 μm) after oxidation test in atmosphere environment.

High temperature LOCA (loss-of-coolant accident) oxidation test

Fifteen samples have been subjected to oxidation test in steam (LOCA) environment. The tests had two with durations (5 and 20 min). Such exposure time was chosen to evaluate the role of the deposition method and coating thickness onto the protective scale into LOCA conditions. In details, the parameters of LOCA test are shown in **Table 5**:

Table 5. The parameters of LOCA experiments. *For LOCA 2, two uncoated samples have been tested, one for 15 minutes (additionally) and the other for 20 minutes.

Test	Number of samples			Temperature (°C)	Time (min)
	Electrodeposited	Magnetron	Uncoated		
LOCA 1	3	3	1	1200	5
LOCA 2	3	3	2*	1200	20

For these tests, experiments have been carried out on uncoated Zr-1Nb samples with the same conditions but at three different times. It is possible to evaluate the oxidation kinetics of uncoated Zr-1Nb alloy.
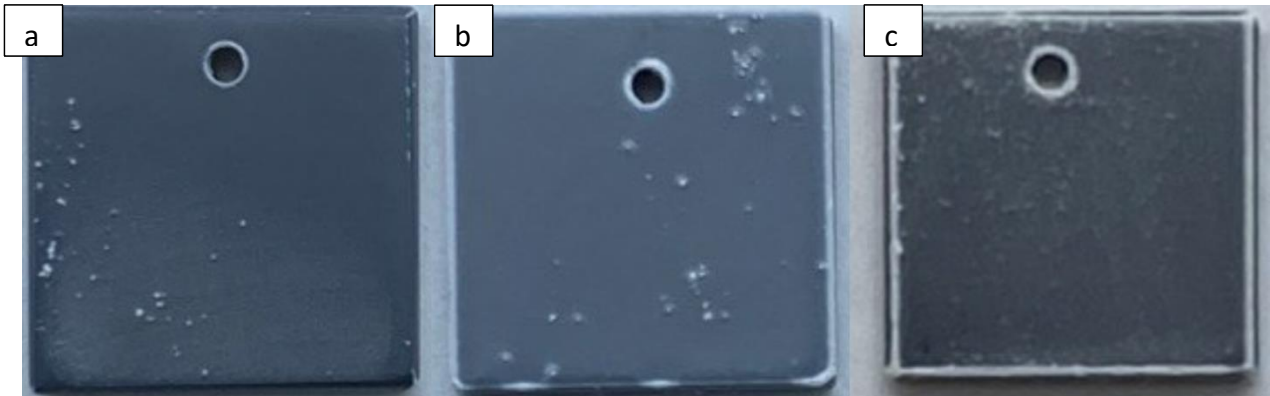
Figure 59. Outer view results of LOCA oxidation test of uncoated Zr-1Nb alloy at different time of exposure. (a) 5 minutes; (b) 15 minutes; (c) 20 minutes.

It is good to see from **Figure 59** that ZrO_2 layers were rapidly grown on the corners and in the hole of the sample. When the exposure time was increased, more pronounced formation of oxides was observed on the defect zones (hole, corners, etc.).
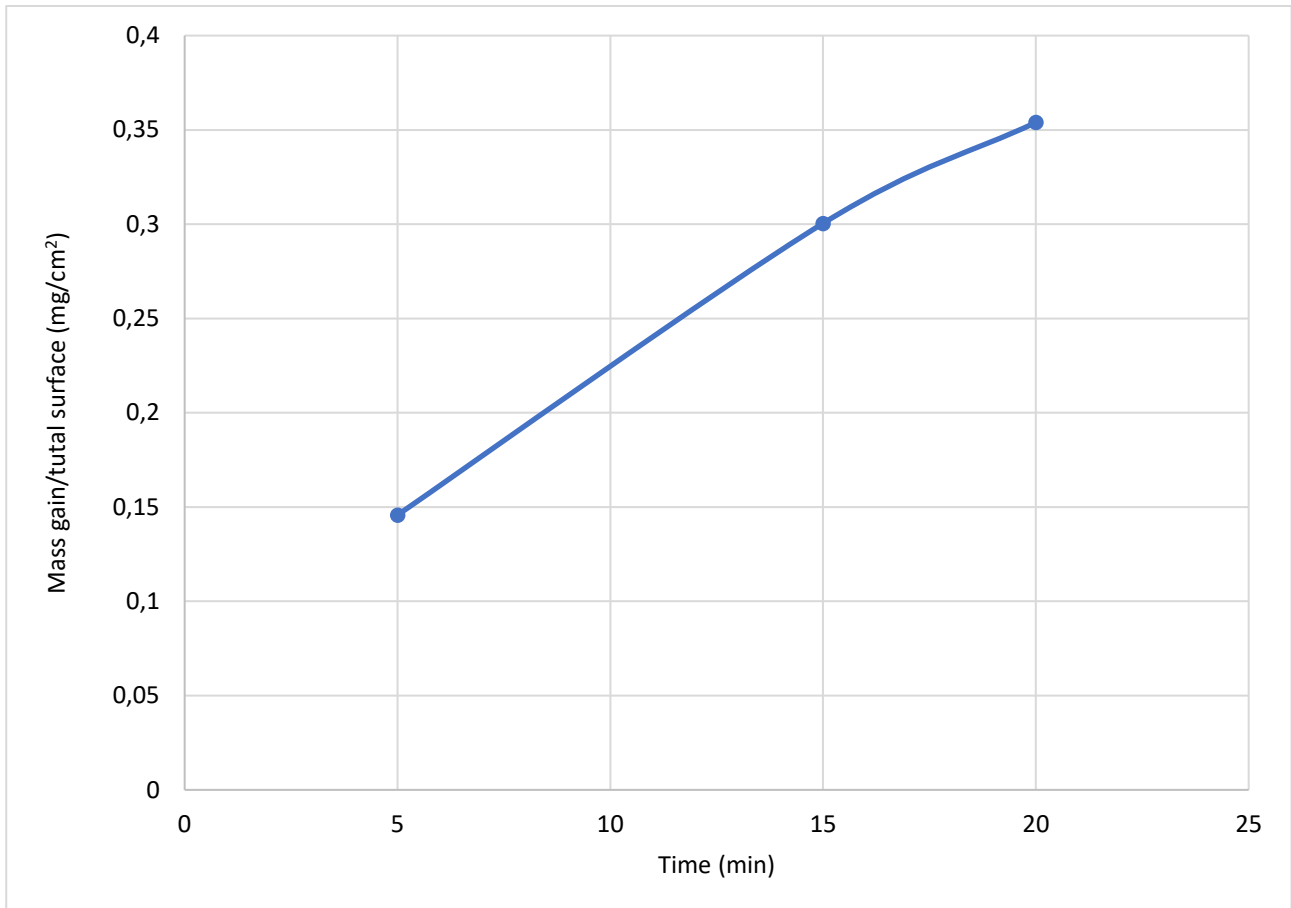
Figure 60. Time dependence of the weight gain of uncoated Zr-1Nb alloy under LOCA conditions

Figure 60 represents the behavior of the mass gain onto uncoated Zr-1Nb sample in function of the time of exposure under LOCA condition. The oxidation has practically a linear behavior for this range od oxidation time. However, for literature Zr have a parabolic oxidation kinetic that can be observed for longer oxidation processes.
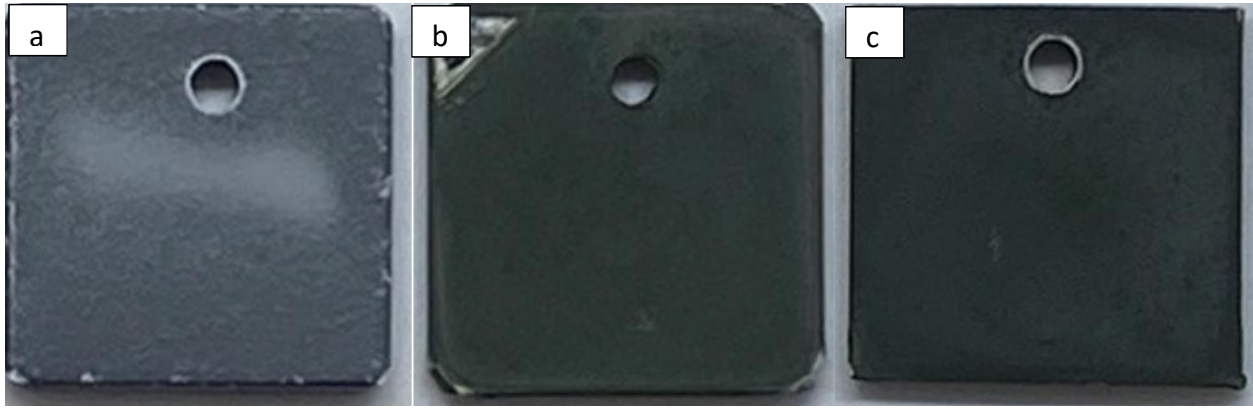
Figure 61. Outer view results of oxidation test in steam environment for 5 minutes. (a) Uncoated; (b) Magnetron-deposited; (c) Electrodeposited.
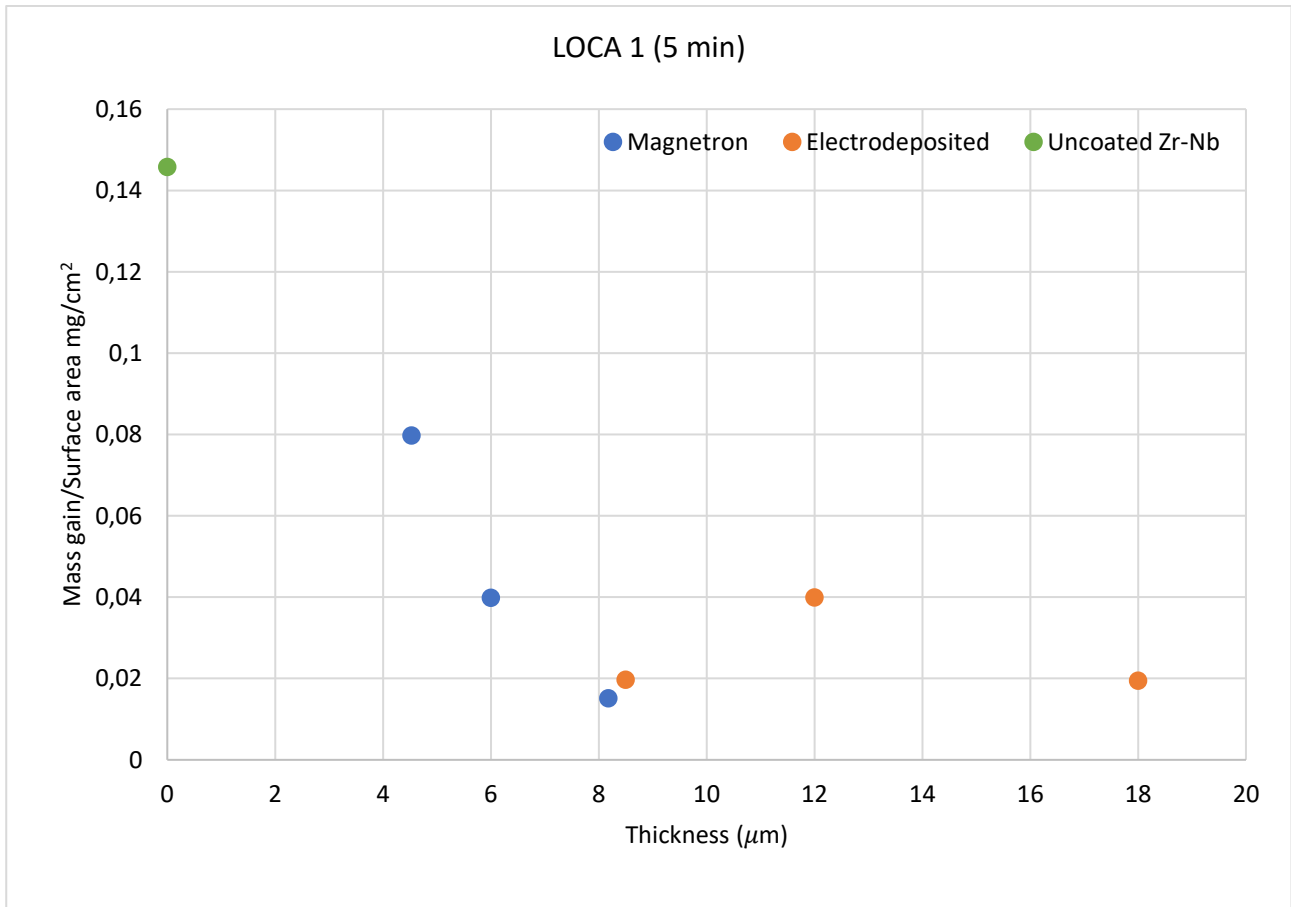
Figure 62. Gravimetry results for LOCA oxidation test for 5 minutes

The result of the gravimetry test after 5-minutes oxidation (**Figure 62**) is that both deposited Cr coatings are protective if compared with the uncoated Zr-1Nb. By increasing the coating thickness,

102

the protection properties were also increased. It is more pronounced for magnetron coatings. The lowest mass gain was found for Cr-62 sample with 8.2 μm thickness. While higher values of the mass gains were found for electroplated Cr samples. Unfortunately, the dependence of the mass gain versus thickness of galvanic coatings is not clear. A non-uniform deposition of Cr onto the corners can be the reason for such behavior.

Figure 63 and **Figure 64** show the results of 20 min-oxidation of the samples in LOCA conditions. It is shown that for longer oxidation test, the difference of the mass gains of coated and pure Zr-1Nb strongly decreases. At these conditions, the mass gain of uncoated Zr-1Nb is in 1.7 times higher (minimally) in comparison with the coated samples. Moreover, the role of the thickness and deposition technique is similar to the results of 5 min-oxidation test in LOCA conditions. The Cr coatings with higher thickness and deposited are more protective.
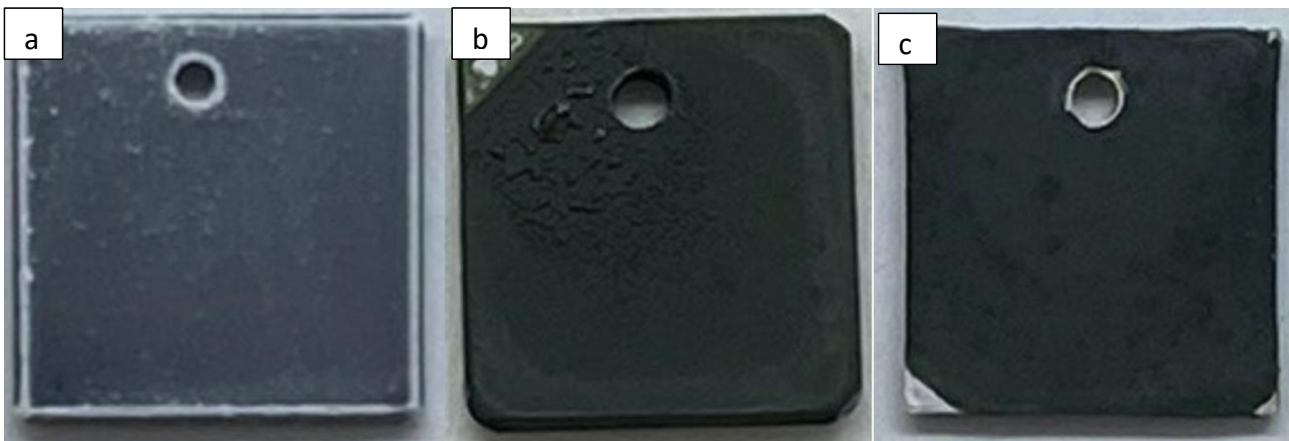
Figure 63. Outer view of samples after oxidation test in steam for 20 minutes. (a) Uncoated; (b) Magnetron-deposited; (c) Electrodeposited.
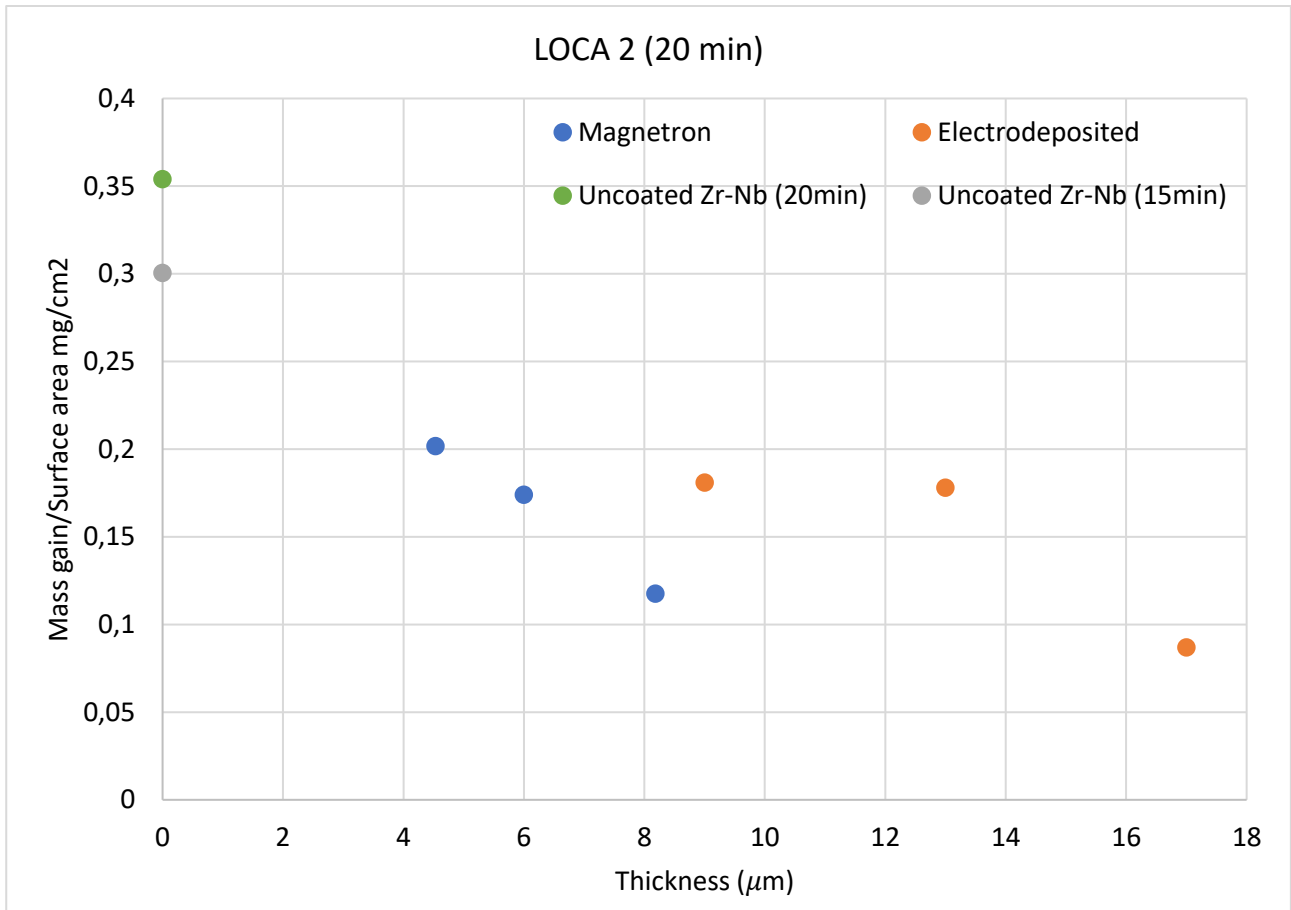
Figure 64. Gravimetry results for LOCA oxidation test for 20 minutes.

For the analysis of behavior of coated samples (by magnetron sputtering) and uncoated Zr-1Nb sheets in the LOCA conditions, all mass gains obtained for 5 and 20 minutes oxidation were plotted in **Figure 65**.
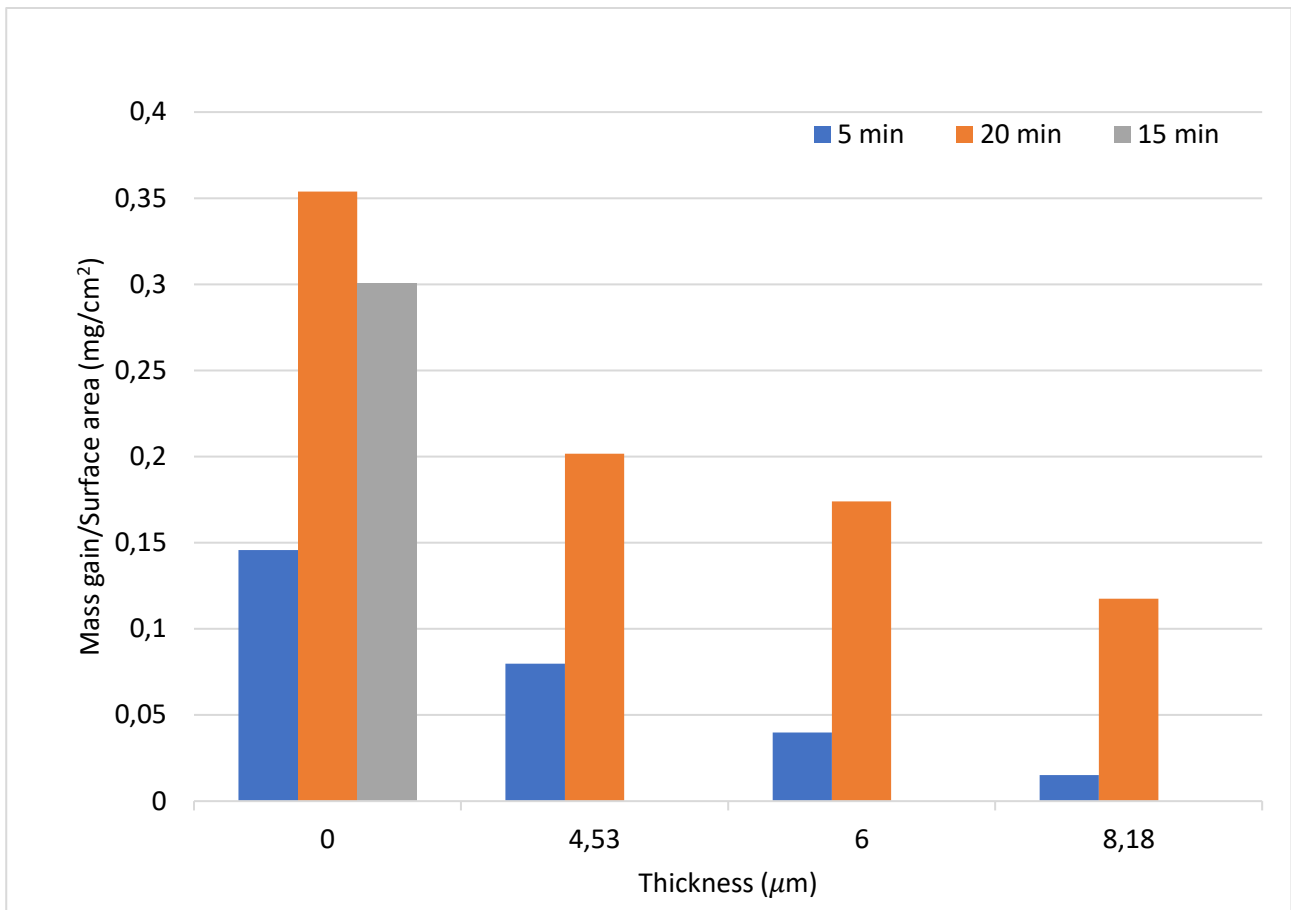
Figure 65. Comparison of Cr coatings deposited by magnetron sputtering and uncoated samples in LOCA conditions for different time of exposure.

In **Figure 65** is resumed the role of the thickness of the Cr coating deposited by magnetron sputtering on the weight gain. A clear result is that increasing the thickness, the weight gains due to the oxidation decreases. In conclusion, it means that as the thickness of the Cr coating increases, the time of protection condition will be longer.

Crystal structure

The XRD spectra from **Figure 66** to **Figure 72** show the crystal structure of Zr-1Nb sheets with and without Cr coatings in as-deposited state and, after LOCA oxidation (5 and 20 min).

XRD data (**Figure 67**)of the uncoated Zr-1Nb shows a fully oxidized surface after 5 min oxidation test, strong intensities of ZrO_2 phase are observed. Another situation is found for coated samples: according to **Figure 68** and **Figure 69**, these coated samples are protective for 5 min oxidation test. The presence of Cr_2O_3, BCC Cr and Cr_2Zr phases are shown in the XRD patterns. No ZrO_2 phase is observed even for the thinnest coatings (both magnetron and galvanic). For thicker coatings we have similar trend (**Figure 118**, **Figure 121**, **Figure 123**, **Figure 124**, in **APPENDIX**).
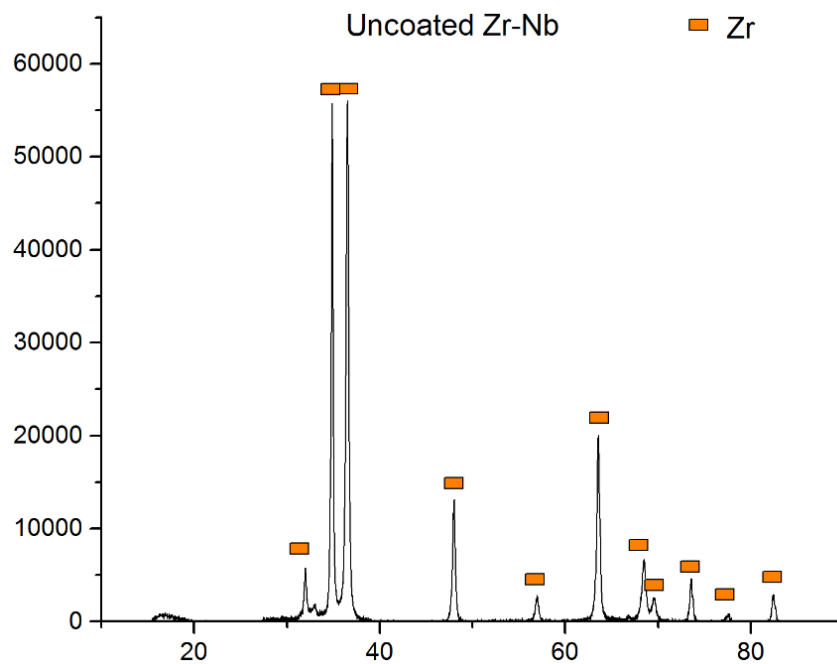
Figure 66. XRD spectrum of uncoated Zr-1Nb sample before oxidation test.
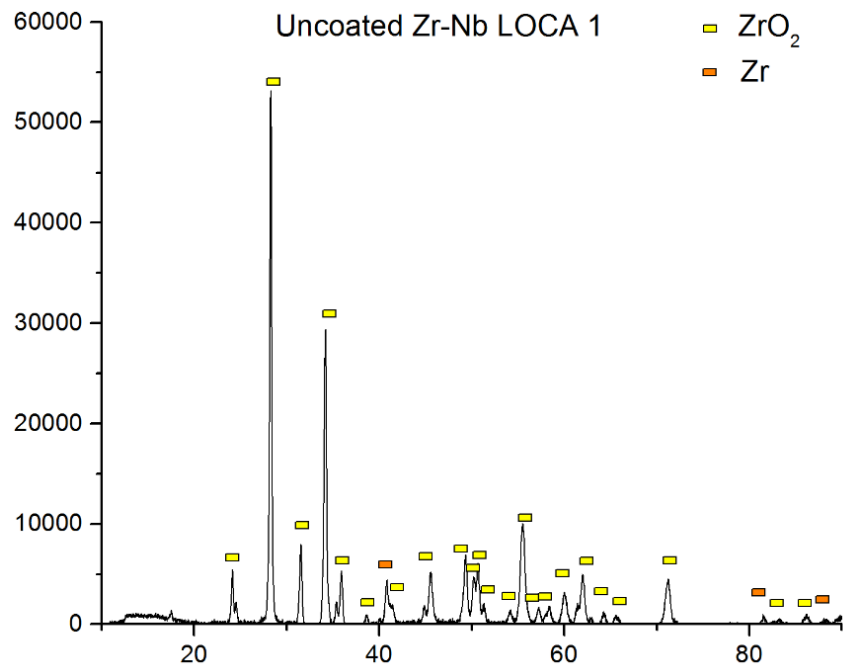
Figure 67. XRD spectrum of oxidized uncoated Zr-1Nb sample in steam environment for 5 min.
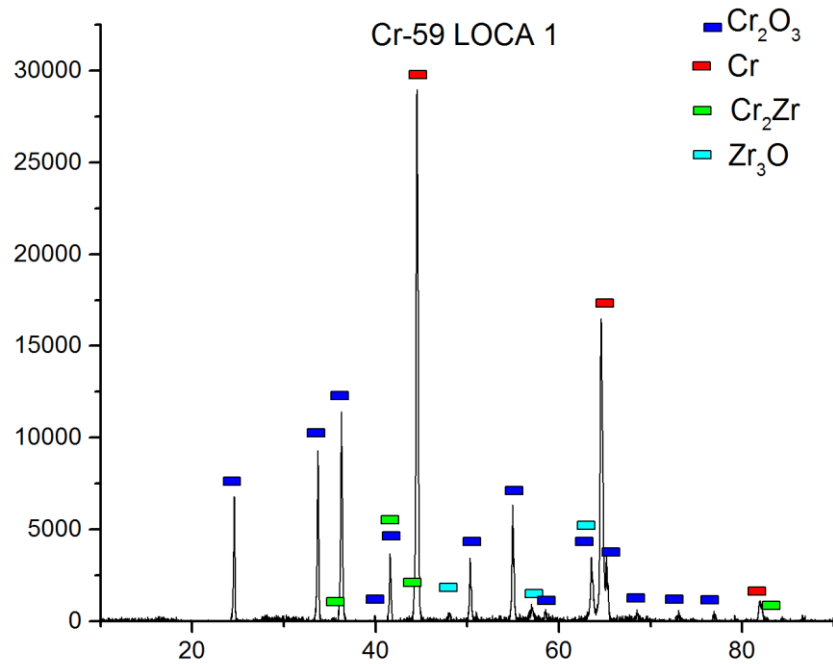
Figure 68. XRD spectrum of oxidized Cr coating (Cr-59 – 4.5 μm) deposited by magnetron sputtering in steam environment for 5 min.
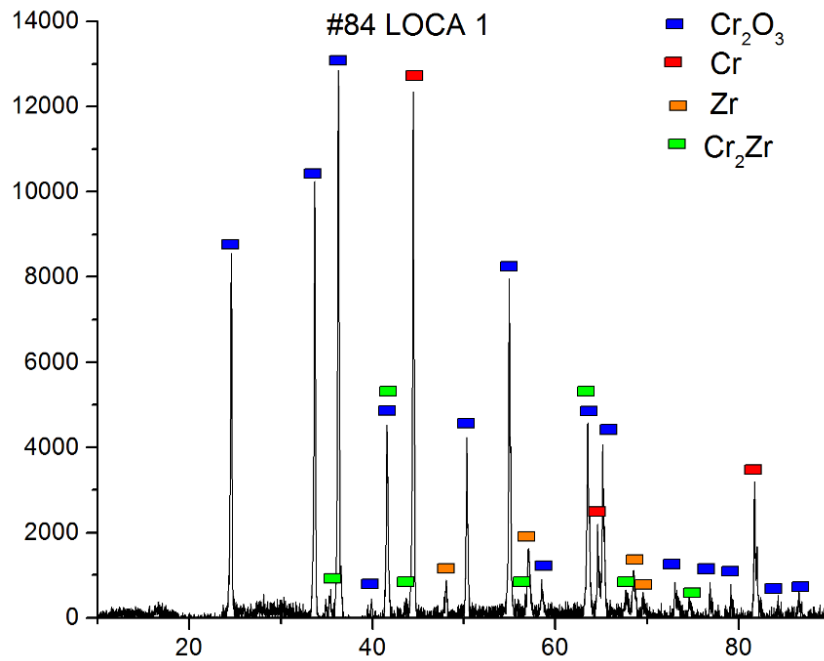
Figure 69. XRD spectrum of oxidized Cr coating (#84 – 8 μm) deposited by electroplating in steam environment for 5 min.

The formation of Cr_2O_3 phase is related to oxidation of coating during the oxidation test. The residual part of the as-deposited Cr coating has still BCC structure. The growth of Cr_2Zr interlayer is related to the high diffusion coefficient of Cr and Zr for considered temperature conditions. According to the literature, thickness of Cr_2Zr interlayer can be up to 2 μm.

LOCA 2 oxidation test

Figure 70 - **Figure 72** show the XRD patterns of oxidized samples during 20 min in LOCA condition. There is also observed that uncoated Zr alloy is fully oxidized. The crystal structure of the coated sample after 20 min oxidation is different in comparison with 5 min test.
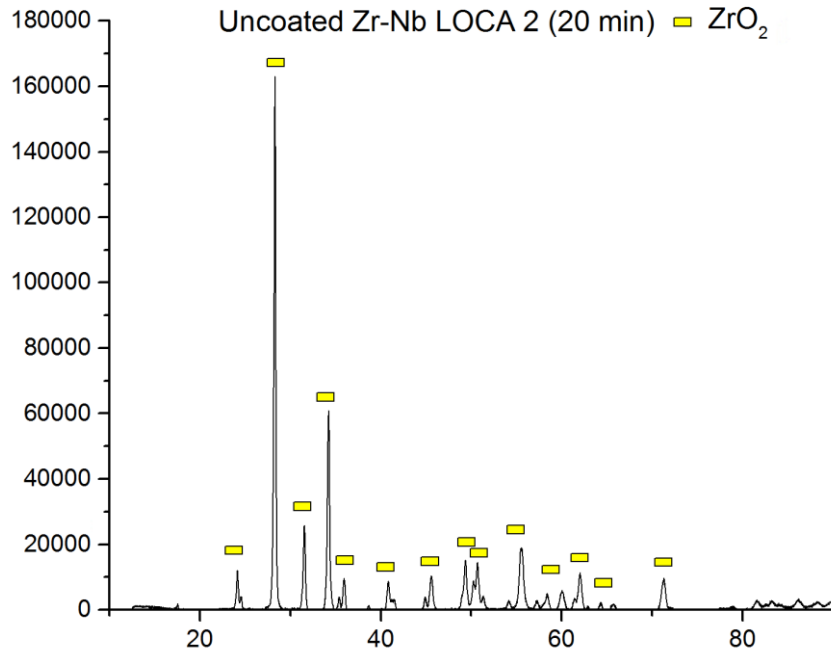
Figure 70. XRD spectrum of oxidized uncoated Zr-1Nb sample in steam environment for 20 min.
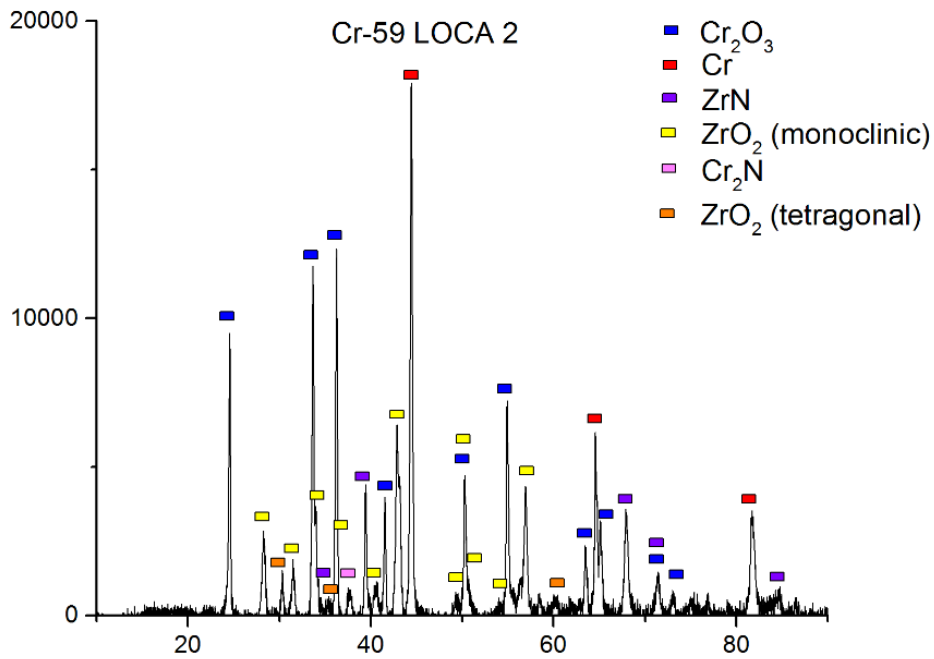
Figure 71. XRD spectrum of oxidized Cr coating (sample Cr-59 – 4.5 μm) deposited by magnetron sputtering in steam environment for 20 min.
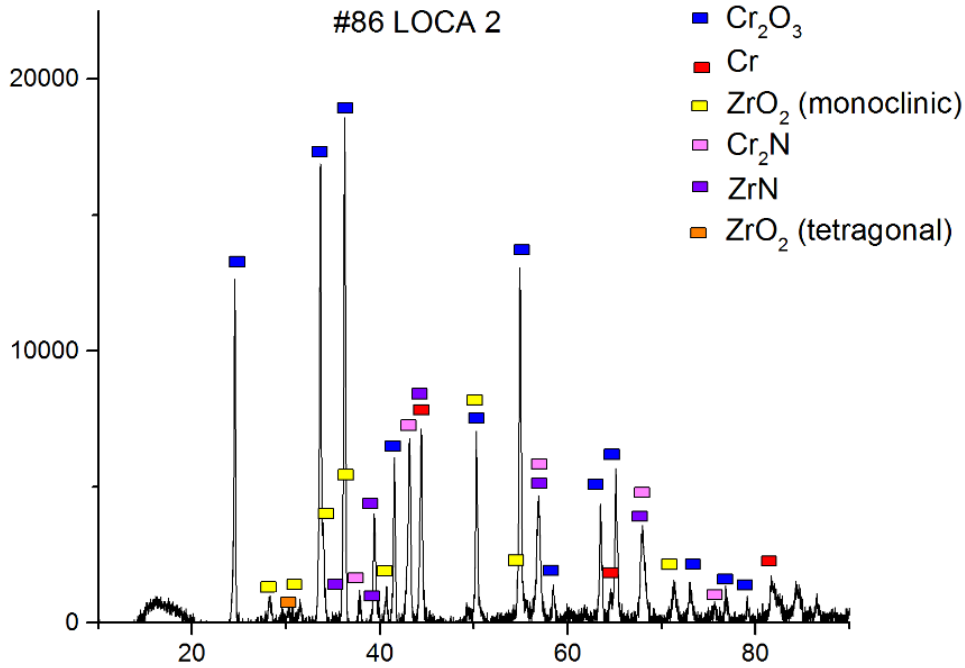
Figure 72. XRD spectrum of oxidized Cr coating (#86 – 9 μm) deposited by electroplating in steam environment for 20 min.

On the coated samples, it was found Cr_2O_3 phase and residual BCC Cr phase similar to previous results (5 min oxidation test). Cr_2Zr phase was not detected, but ZrO_2 (monoclinic), and ZrO_2(tetragonal), ZrN and Cr_2N phases are found in all coated samples independently from their thickness and deposition technique.

There is the presence of chromium and zirconium nitrides, it can be caused by the presence of nitrogen in the steam atmosphere (e.g., non-optimal condition for the experiment) or by the exposure to the atmosphere immediately after the LOCA test. The possible mechanism of nitrides formation will be done in the next section.

GDOES after oxidation in steam environment

The GDOES test were performed to investigate the structure and elemental distribution over the depth of the sample and to find the position of nitrides in the samples. The intensities of O, H, N were increased in 5 times onto GDOES graphs for clear analysis of the samples.

Figure 73 - **Figure 75** show the elemental distribution of samples after LOCA 1 oxidation test. The uncoated Zr-1Nb samples show only Zr and oxygen through the sputtering depth. It is a good confirmed with XRD data and means that only ZrO_2 layer is present on the sample surface. The coated samples have another structure. There is found strong oxygen signal on the sample surface and Cr. This means that Cr_2O_3 is the upper layer. Then, Cr intensity is observed which is related to residual BCC Cr. At higher depths, the signal of Zr is found. There are no oxygen or nitrogen signals. It means that no oxidation of Zr alloy is occurred. However, the profile of Cr-Zr interface is not sharp, it can be due to interdiffusion of Cr and Zr and formation of Cr_2Zr phase. Such trend is also observed for all samples, both magnetron and galvanic.
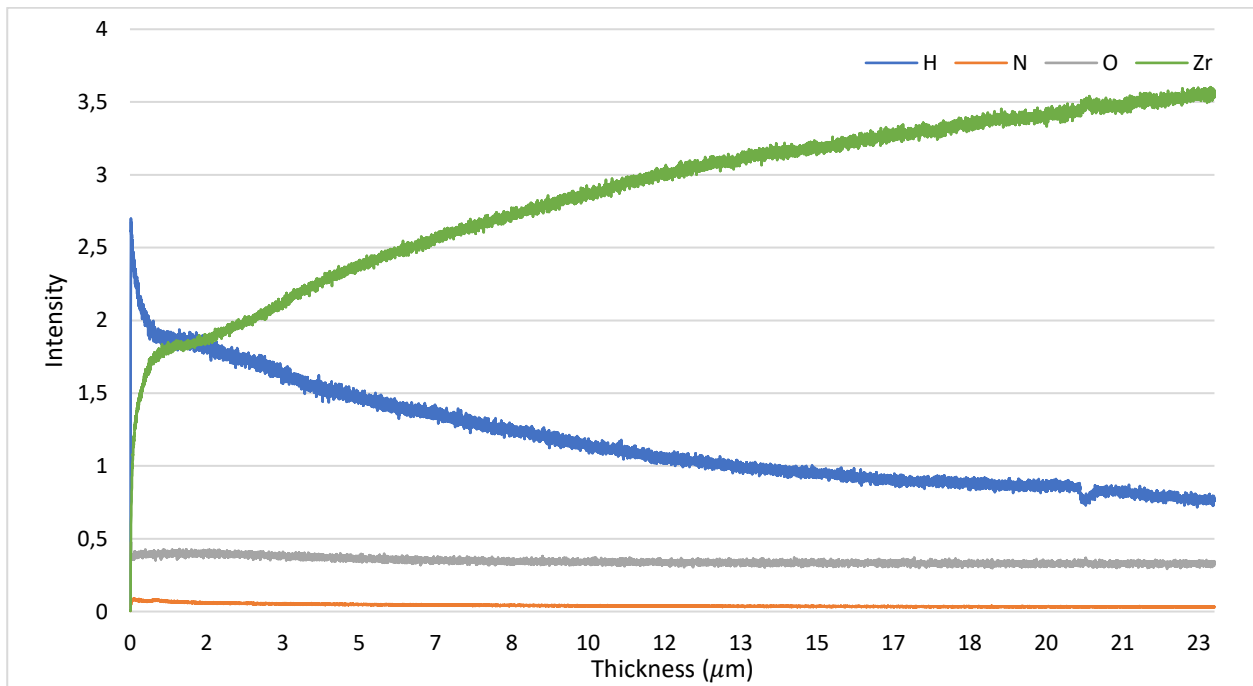
Figure 73. GDOES profile of uncoated Zr-1Nb after oxidation test in steam environment for 5 min.
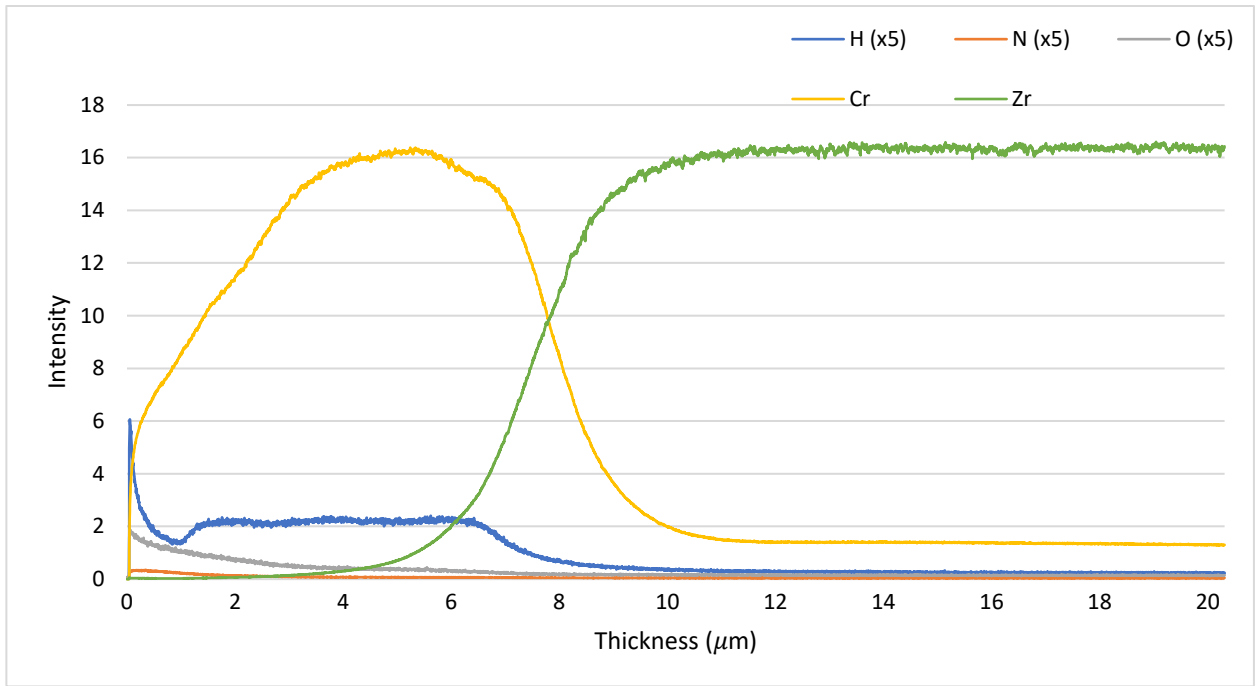
Figure 74. GDOES profile of magnetron-deposited sample (Cr-61 – 6 μm) after oxidation test in steam environment for 5 min.
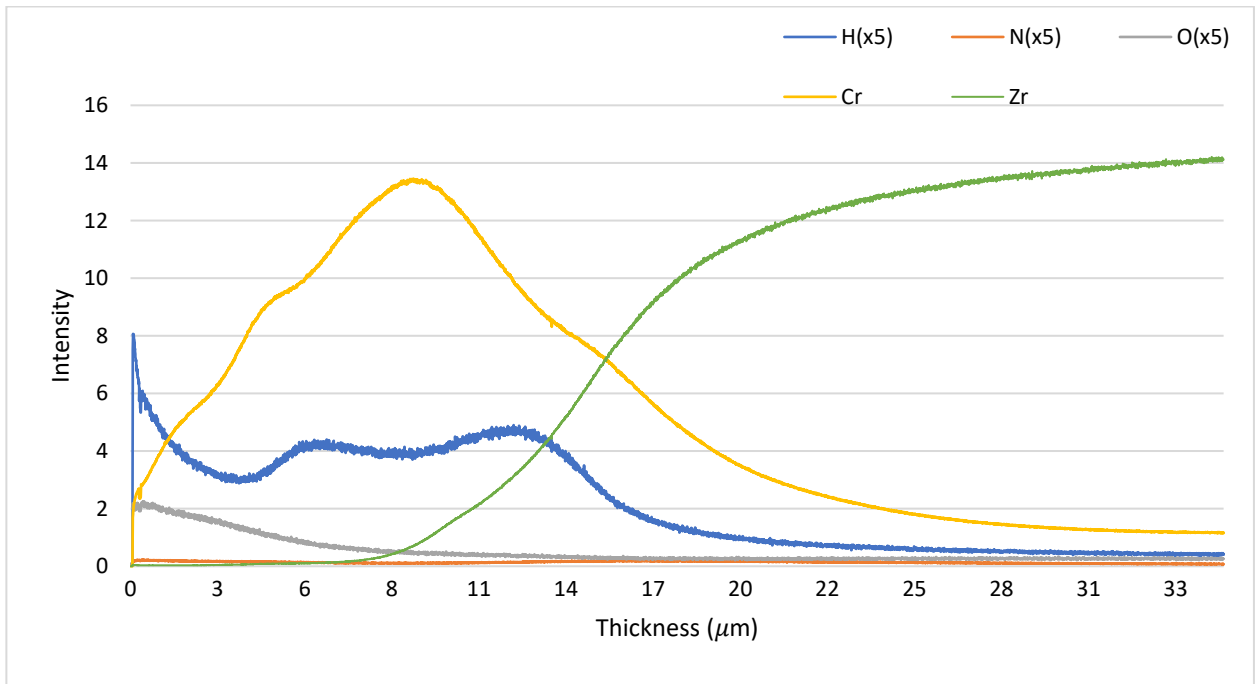
Figure 75. GDOES profile of electrodeposited sample (#77 – 12 μm) after oxidation test in steam environment for 5 min.

Figure 76 - **Figure 78** show the elemental distribution over depth for the uncoated and Cr coated Zr-1Nb samples. The uncoated Zr-1Nb sample has only signals from Zr and oxygen, that is related to ZrO_2 layer on the sample surface. The coated samples have a different structure in comparison with the samples after 5 min oxidation test. Cr_2O_3 and Cr layers are still present at the sample surface. There is obviously shown the presence of nitrogen and oxygen at the Cr - Zr interface.
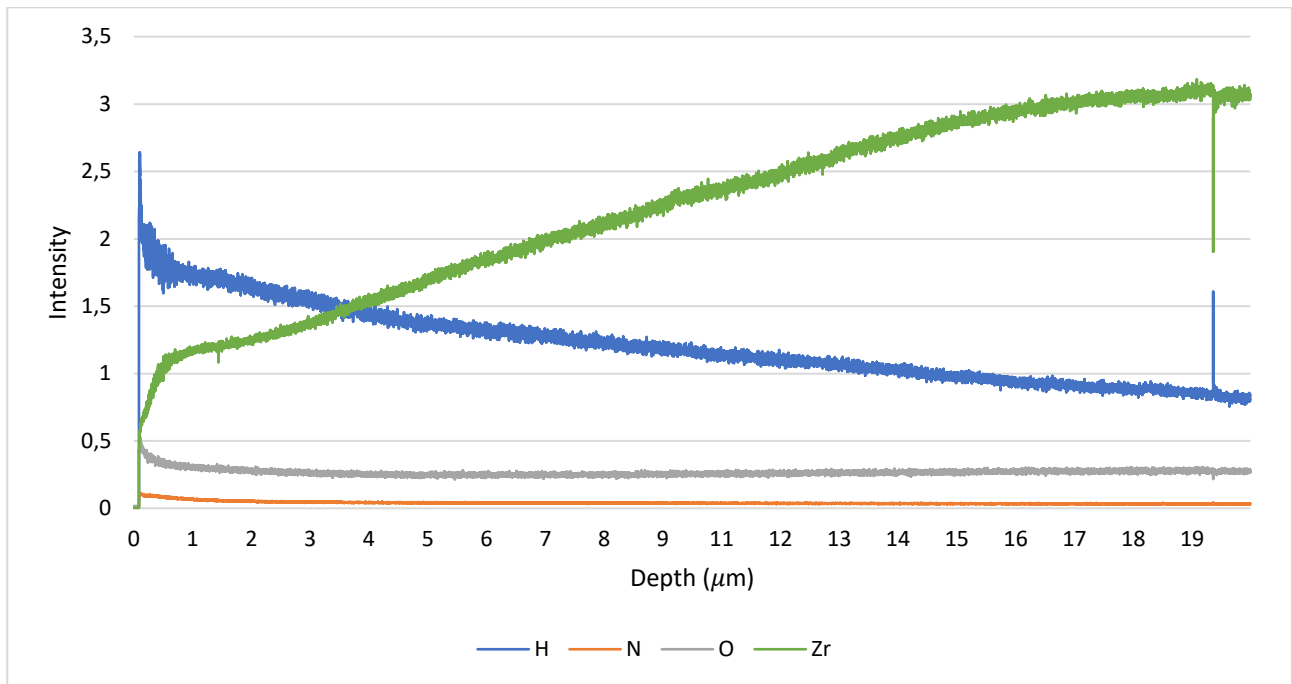
Figure 76. GDOES profile of uncoated Zr-1Nb sample after 20 min in LOCA.
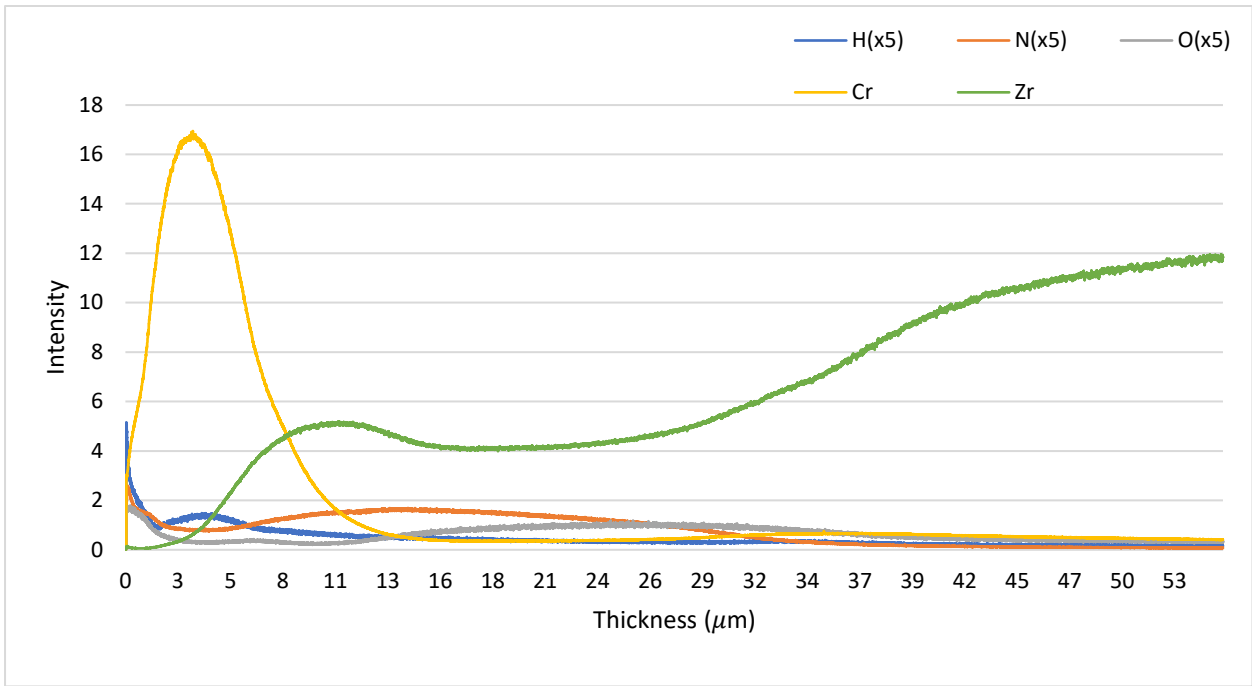
Figure 77. GDOES profile of magnetron deposited sample (Cr-61 – 6 µm) after oxidation test in steam environment for 20 min.
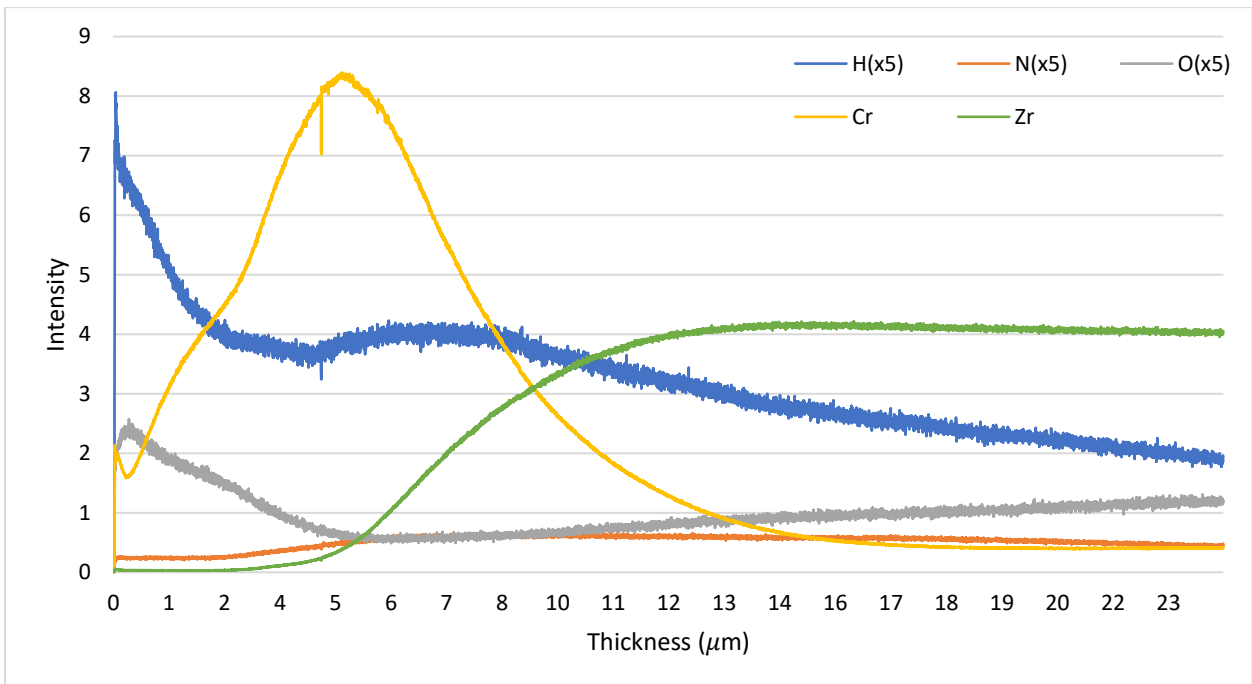
Figure 78. GDOES profile of electrodeposited sample (#87 - 12 µm) after oxidation test in steam environment for 20 min.

According to the XRD data and obtained results by GDOES, the distribution of oxygen and nitrogen in the samples shows the possible oxidation mechanism of Cr coated samples.

1. If the Cr coating is protective during the oxidation test (e.g., for 5 min test), the sample can save its integrity even for extraction procedures. Then the sample are subjected to thermal shock (the sample is extracted from the quartz tube and immersed in room temperature water). In this case the sample has protective Cr layer on the sample surface and no oxygen into the Zr samples.

2. If the coating is not protective (oxidized during the test or with low thickness), the oxide layer can be cracked leading to nitrogen and oxygen interaction with α-Zr(O) phase. In this case, a rapid growth of ZrN phase, next ZrO_2 phase can happen. Such behavior is more pronounced for thin coating and for coating with initial bad adhesion between Cr and Zr. It is obviously shown in GDOES graphs and XRD patterns.

In conclusion, XRD and GDOES data of oxidized samples in LOCA conditions show that the corrosion behavior is higher for coatings deposited by magnetron sputtering and for higher thickness. This is due to the higher adhesion, more compact structure and higher uniformity of the coatings.

LECO after oxidation in steam environment

The uncoated Zr-1Nb samples for LECO experiments could not be prepared in an appropriate way for the test because they have a brittle behavior (predominantly due to form α-Zr(O) phase and spallation of ZrO_2 layers from the sample even during the oxidation tests).

Table 6. Hydrogen content measured by LECO equipment of oxidized samples after 5 minutes under LOCA conditions.

LOCA 1 (5 minutes)			
Deposition techniques	sample	Thickness of protective Cr coating (μm)	Hydrogen content (ppm)
Magnetron sputtering	Cr-59	4.5	85.5
	Cr-61	6	47.4

	Cr-62	8.2	25.5
Electrodeposition	#84	8	23.7
	#77	12	55.9
	#76	18	46.2
Uncoated Zr-1Nb	Zr	0	12.5

For 5 minutes LOCA test, the hydrogen content of magnetron samples significantly decreases by increasing the thickness of the protective Cr coating. It is well known that Cr coatings have low hydrogen permeability even for high temperatures, thus it is good confirmed by our results. For galvanic coatings, the dependence of hydrogen permeability versus coating thickness is not simple. Most likely that is related to their initial microstructure (porous and non-compact). So, the hydrogen penetration into the samples can be various due to their non-uniform microstructure. Nevertheless, there is presented that dense and compact Cr coatings deposited by magnetron sputtering have better effectiveness for preventing hydrogen absorption by Zr based samples. **Table 7** shows the hydrogen content in the samples after 20 min LOCA oxidation test. A strong increase of hydrogen content has been found.

Table 7. Hydrogen content measured by LECO equipment of oxidized samples after 20 minutes under LOCA conditions.

LOCA 2 (20 minutes)			
Deposition technique	Sample	Thickness of protective Cr coating(μm)	Hydrogen content (ppm)
Magnetron sputtering	Cr-59	4.5	135.9
	Cr-61	6	142.9
	Cr-62	8.2	131.6
Electrodeposition	#86	9	178
	#87	12	164.4
	#82	17	139
Uncoated Zr-1Nb	Zr 15min	0	20.4
	Zr 20min	0	20.9

For 20 minutes LOCA test, the magnetron samples have similar quantities of hydrogen content, while for electrodeposited samples it decreases as increasing the thickness of the Cr coating.

This different behavior of magnetron-deposited and electrodeposited coating may be due to the significant difference in variability of thicknesses. While for sample coated by magnetron sputtering the difference in thickness (between the thinnest and the thickest samples) is about 4 μm, the electroplated samples have higher variability of coating thicknesses (from 6 up to 18 μm). These features may justify the different hydrogen content behavior of 20 minutes test in function of the coating thicknesses for the two different depositions techniques. Nevertheless, it can be found again that the Cr coatings deposited by magnetron sputtering have better effectiveness for preventing hydrogen absorption by Zr based samples. The hydrogen content in the samples of Cr-59, Cr-61 and Cr-62 is similar to the thickest galvanic sample (#82) with 18 μm-thick of Cr coating.

CONCLUSIONS

This study is devoted to the deposition of Cr coating onto Zr alloys both by electrodeposition and magnetron sputtering. The Cr coatings with different thickness have been deposited onto Zr-1Nb (E110) to protect Zr alloy from high temperature oxidation.

Firstly, the procedure of electroplating of Cr coating onto Zr was developed. Initially, the samples are treated with sandpaper (grit 100) and subsequently etched in aqueous solution containing 10% HF (38%) and 10% vol. HNO_3 (65%) for 3 minutes at room temperature. Then, activation step is done in fluorides solution composed by 18 g $NaHF_2$ with 2 ml H_2SO_4 (96%) per liter, at room temperature for 1 min to dissolve the tenacious oxide on the metal surface and to form a protective layer. Immediately after the activation step, the electroplating process must be carried out as soon as possible. The electroplating is carried out in an electrolyte containing 250 g/l CrO_3, 2,5 g H_2SO_4 and 1,75 g HF (38%), with a current density of 0,21 A/cm^2 and it must follow a temperature profile during the electrodeposition process. It should start from room temperature for few minutes (8-10 min), in order to deposit a gray layer, which is adherent to the substrate. Then, by increasing the temperature up to 50°C during the electroplating process, a brighter and smoother Cr is deposited. For 1-hour deposition, the expected thickness is about 15 μm with an overall cathodic current efficiency of 15%.

With this procedure, several samples with different thickness have been deposited:

Table 8. Samples prepared by electroplating and relative thickness.

Sample (#)	Thickness (μm)
67	20
68	15
69	15
70	35
71	15
73	22
74	17
75	11
76	18
77	12
78	12
79	14
80	15
81	11
82	17
84	8
85	10
86	9
87	12
88	6
89	20

For magnetron sputtering, multi-cathode plasma source was used to deposit Cr coatings (each magnetron worked with I=4.6A and U=750V). A chemical pretreatment of the samples was used. Then, the samples were plasma etched by Ar ions (2500 V, 46 mA, 0.15 Pa, Ar 7-8, U_{bias} 600 V, I_{bias} 0.04-0.05 A f_{bias} 100 kHz, duty cycle 70%). After it, long-term processes (3-5 hours to deposit 4.5-6 μm) were performed for magnetron sputtering of Cr onto Zr-1Nb samples.

4 sets of deposition (Cr-59, Cr-60, Cr-61, Cr-62) were done with different thickness:

Table 9. Set of deposition carried out by magnetron sputtering and relative thickness.

Sample	Thickness (µm)
Cr-59	4.5
Cr-60	1.3
Cr-61	6
Cr-62	8.2

After the depositions, the crystal structure, microstructure and adhesion of the coating were investigated. Subsequently coated and uncoated samples have been tested in atmosphere (ramp from 500°C to 1100°C in 29 min, steady state for 40 min and cooling to 500°C in 37 min) and LOCA (1200°C for 5 and 20 min) oxidation tests. Then post-analyses of the samples were done by XRD, SEM, optical microscopy, GDOES and LECO.

The obtained results show that electrodeposited and magnetron coatings can be protective in high-temperature oxidation in air. Gravimetry test shows a drastically decrease (at least 4 times lower) in weight gain of Cr-coated samples compared to uncoated Zr alloy. Moreover, the thickness of the as-deposited Cr coating influences the high-temperature oxidation resistance. The samples deposited by magnetron sputtering show lower weight gain by increasing the thickness. For electrodeposited samples, this trend is not clear as it was affected by non-uniform deposition on the corners. Microscopy showed that the uncoated Zr-1Nb, after oxidation test in atmosphere, has a thickness of ZrO_2 greater than 800 µm, while zirconium oxides were not observed Cr coated samples, both for magnetron sputtered and electrodeposited.

In LOCA conditions (5 and 20 min) the magnetron-deposited samples show a lower weight gain with increase of coating thickness. The weight gain was reduced by 10 times for the thickest sample. These corrosion experiments confirmed the high role of thickness onto corrosion resistance of Cr coated Zr-1Nb alloy. The galvanic samples also had significant lower weight gains in comparison with the uncoated sample in the same oxidation conditions (7 times less for LOCA 1 and 4 times less for LOCA 2).

The presence of ZrO_2 in XRD pattern may be due to the uncoated part on corners (of both galvanic and magnetron) since oxygen in GDOES profile is visible only at the surface. According to GDOES, nitrogen is also observed. This is confirmed by XRD where ZrN peaks are present. This is more pronounced for low thicknesses, and it means that the coating is not protective. Since the Cr oxide layer is cracked within or during the extraction from the chamber, N interacts with the exposed Zr forming ZrN.

In conclusion, XRD and GDOES data of oxidized samples in LOCA conditions show that the corrosion resistance is higher for coatings deposited by magnetron sputtering and for higher thickness. This is due to the better adhesion, more compact structure and higher uniformity of the coatings.

The comparison of deposition techniques, according to gravimetric tests, the magnetron deposited coatings have similar oxidation resistance as thick galvanic Cr coatings. The coatings are dense, compact and well adherent. Although the gravimetry tests are not fully conclusive, in particular for galvanic coatings, the corrosion behavior of 20 μm electrodeposited Cr is comparable to that of magnetron sputtered of 8 μm thickness.

The two techniques gave very interesting results. In both cases, the Cr coatings have demonstrated a protection to oxidation in air and steam. It has to be taken into account the intrinsic differences in the microstructure of the coatings obtained by electrodeposition and magnetron sputtering. In particular, there is the need to investigate the effect of the hydrogen produced during the electroplating process on the behavior of Zr alloys.

Once the technical feasibility of the deposition of Cr, both for electrodeposition and magnetron sputtering, has been verified onto Zr tubes, an economical sustainability of the two processes must be evaluated.

AKNOWLEDGMENT

This thesis, such as it is, would not have been possible without the help of the following people, to whom I am incredibly grateful.

Professor Massimiliano Bestetti and Professor Dmitrii V. Sidelev. They gave me the opportunity to develop this work under their supervisions and to make this great experience in Tomsk. They have been both extremely patient, knowledgeable, and helpful throughout.
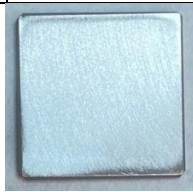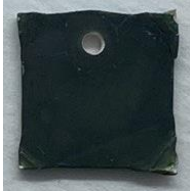
Professor Luca Andena, Federico Morini and Professor Sergey K. Pavlov, who dedicated much of their time to my experiments.
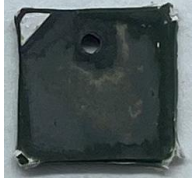
And finally, I would say *"Спасибо большое за всё"* to my international Siberian friends who accompanied me during this path.

APPENDIX

Photo of samples before and after oxidation tests

Table 10. Outer view of results before and after at high temperature oxidation tests.

Test	Deposition technique	Samples		
Initial	Electrodeposited	#88 - 6μm	#87 - 12μm	#82 - 17μm
	Corner deposited by magnetron on electrodeposited	#88 - 6μm	#87 - 6μm	#82 - 6μm
	Magnetron	Cr-59 - 4,5μm	Cr-61 - 6μm	Cr-62 - 8,2μm
	Uncoated Zr-Nb			
Atmos-phere	Electrodeposited			

		#88 - 6μm	#81 - 11μm	#80 - 15μm
	Magnetron	Cr-59 - 4,5μm	Cr-61 - 6μm	Cr-62 - 8,2μm
	Uncoated Zr-Nb			
LOCA 1	Electrodeposited	#84 - 8μm	#77 - 12μm	#76 - 18μm
	Magnetron	Cr-59 - 4,5μm	Cr-61 - 6μm	Cr-62 - 8,2μm
	Uncoated Zr-Nb			
LOCA 2	Electrodeposited	#86 9μm	#87 12μm	#82 17μm

	Magnetron	Cr-59 - 4,5µm	Cr-61 - 6µm	Cr-62 - 8,2µm
	Uncoated Zr-Nb	15 min	20 min	

Inventor sample holder for electroplating
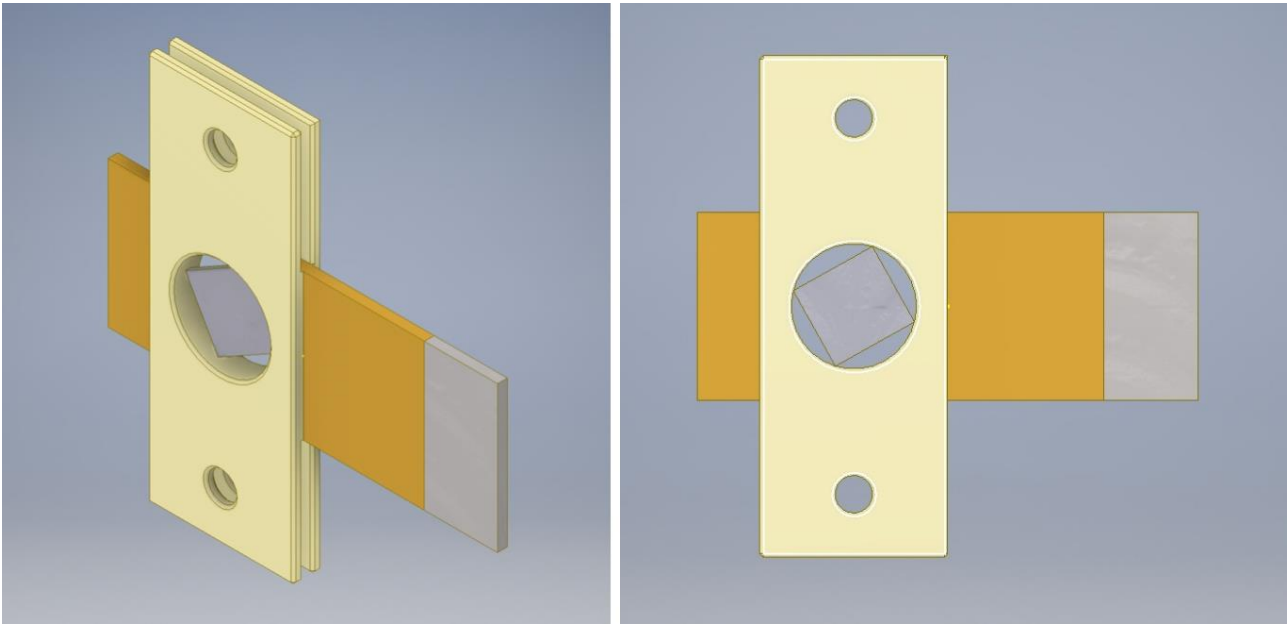
Figure 79. Sample holder for electroplating Zr-Nb sample. It has been used to obtain a more uniform current density lines distribution. (drawing not in scale; mask thickness 8 mm, Zr-Nb 2 mm).

Inventor sample holder for magnetron
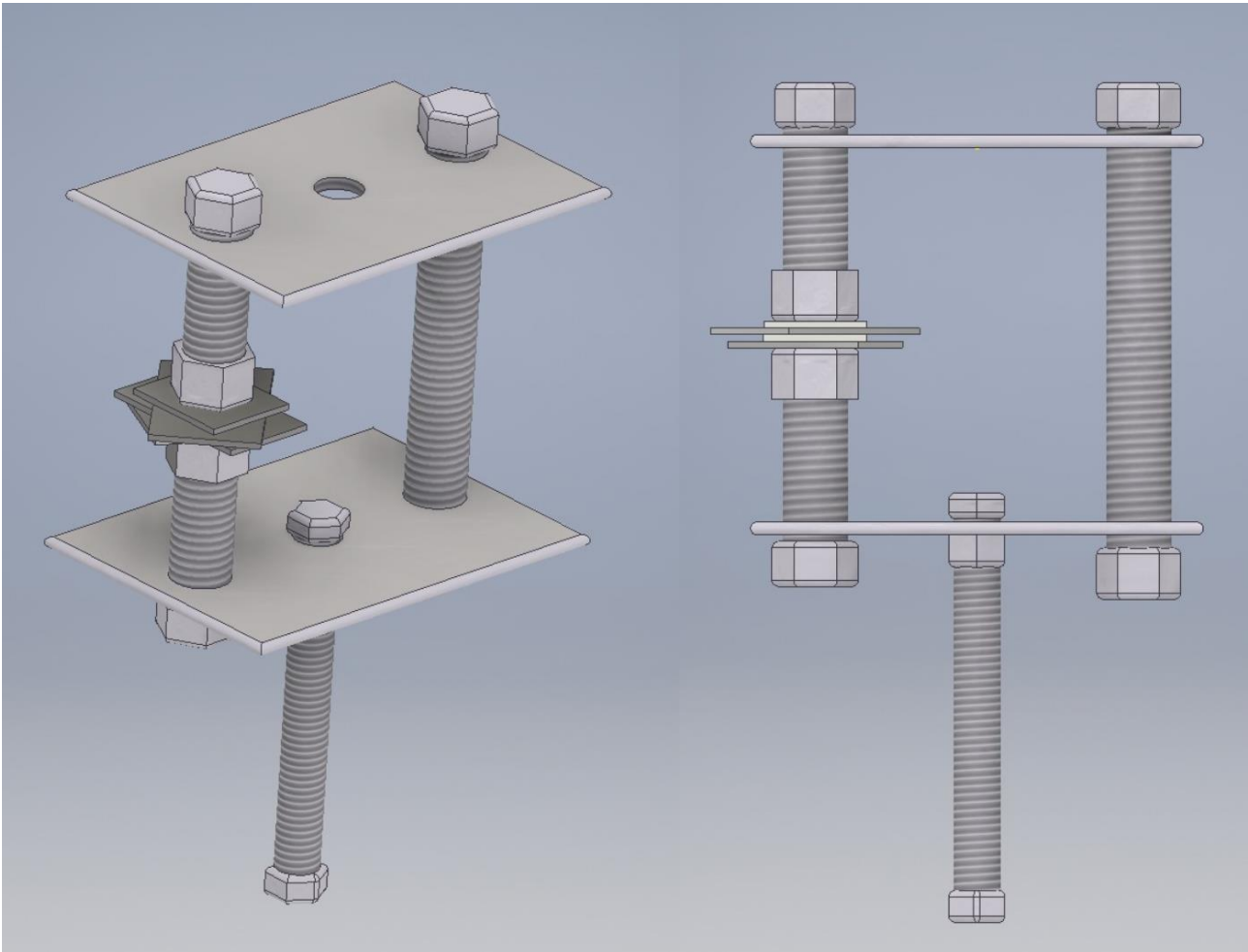
Figure 80. Sample holder used in magnetron sputtering to deposit the Cr coating on the corners of electro-plated samples.

Scratch tests as deposited samples
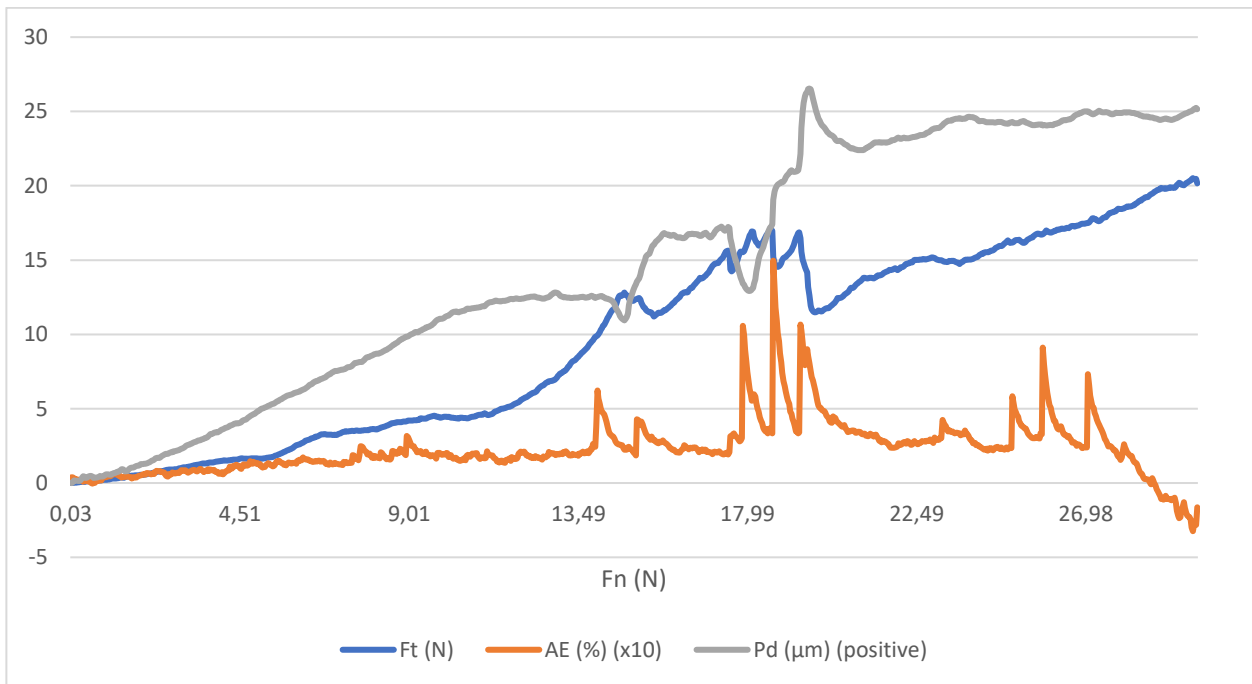
Figure 81. Scratch test on magnetron deposited sample (Cr-61 - 6 µm).
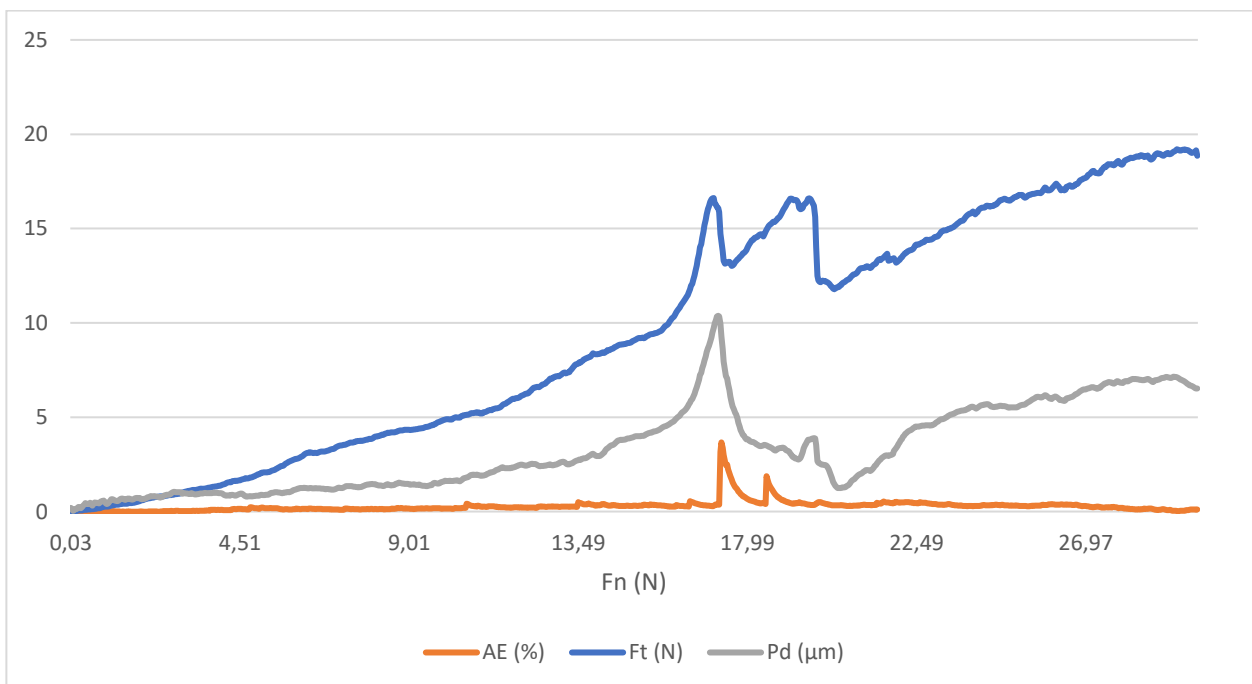
Figure 82. Scratch test on magnetron deposited sample (Cr-62 – 6 µm).
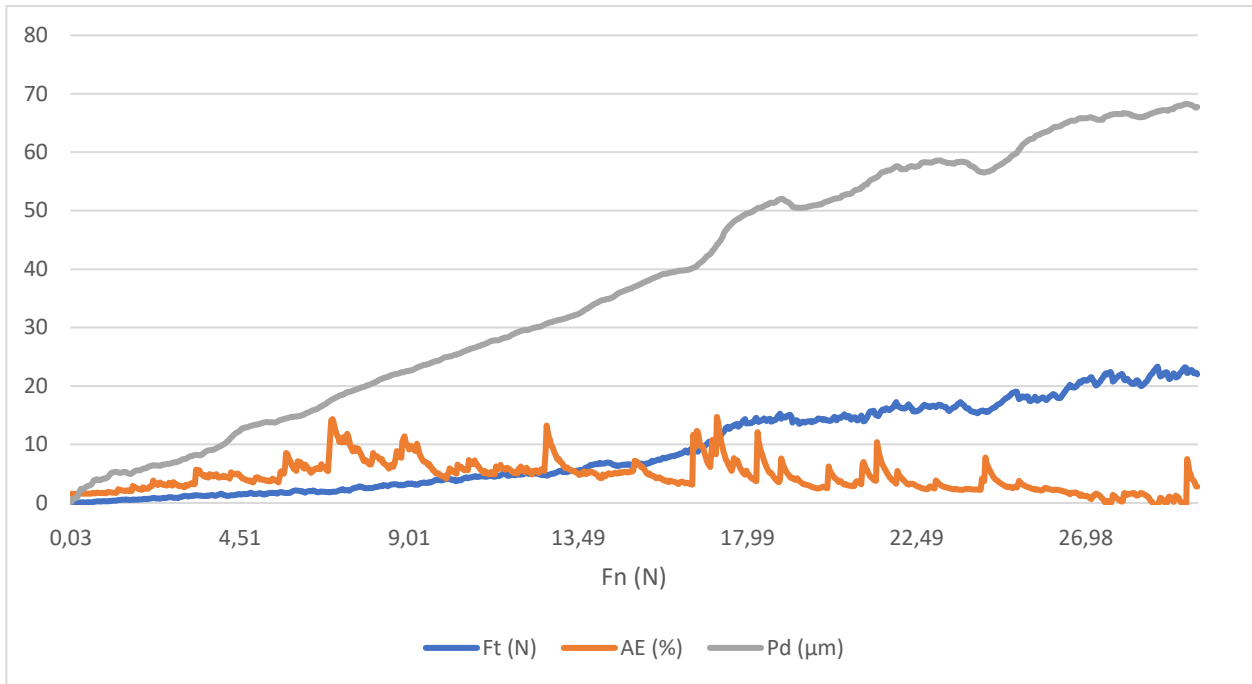
Figure 83. Scratch test on electrodeposited sample (#71 - 15 μm).
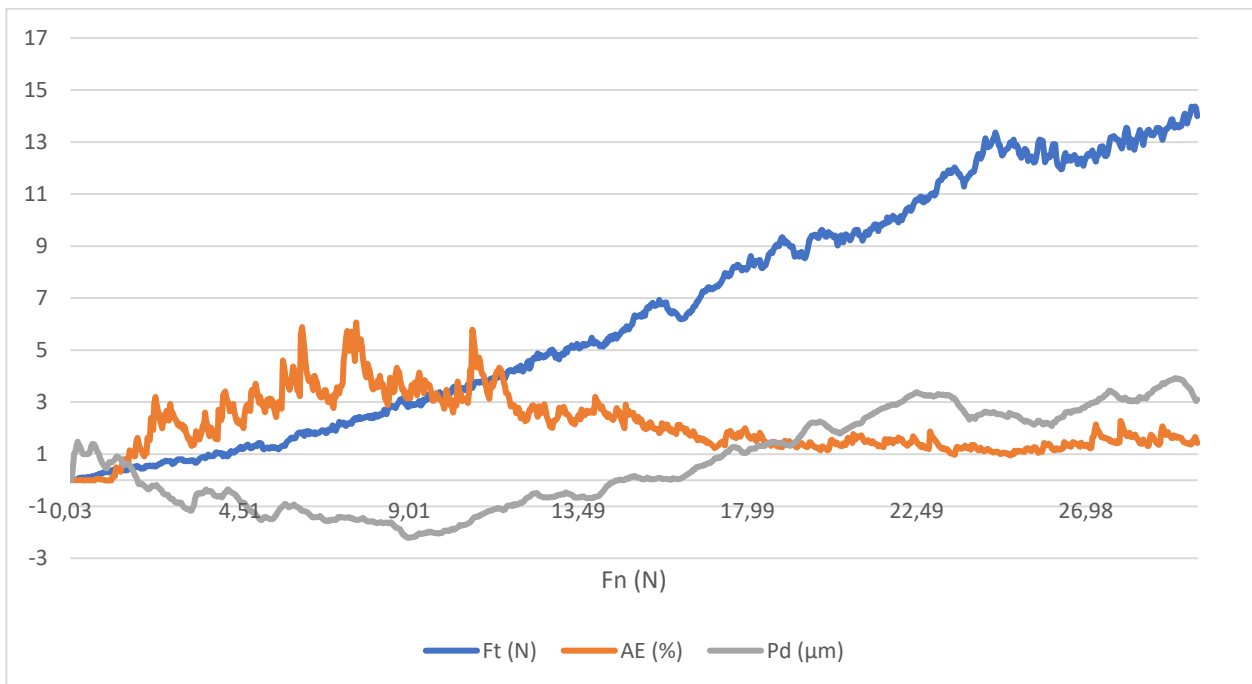
Figure 84. Scratch test on electrodeposited sample (#73 - 22 μm).
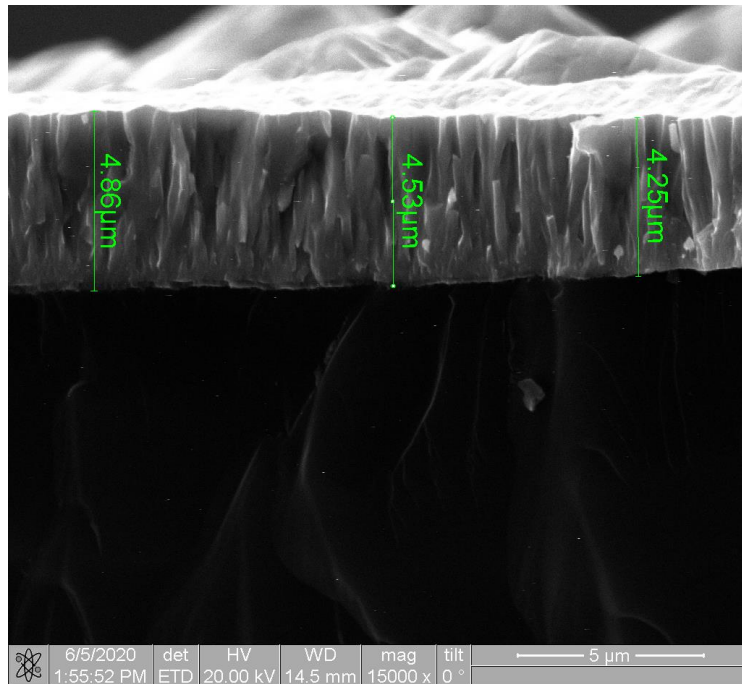
Figure 85. SEM image of magneton deposited Cr-59 result on monocrystal Si substrate.
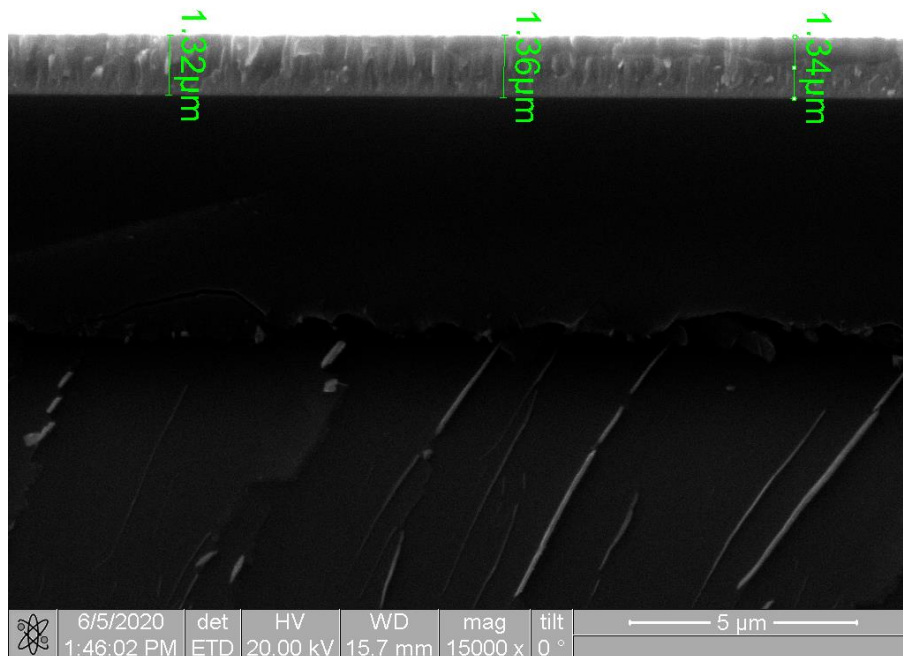
Figure 86. SEM image of magneton deposited Cr-60 (deposition on corners of electroplated samples) result on monocrystal Si substrate.

130
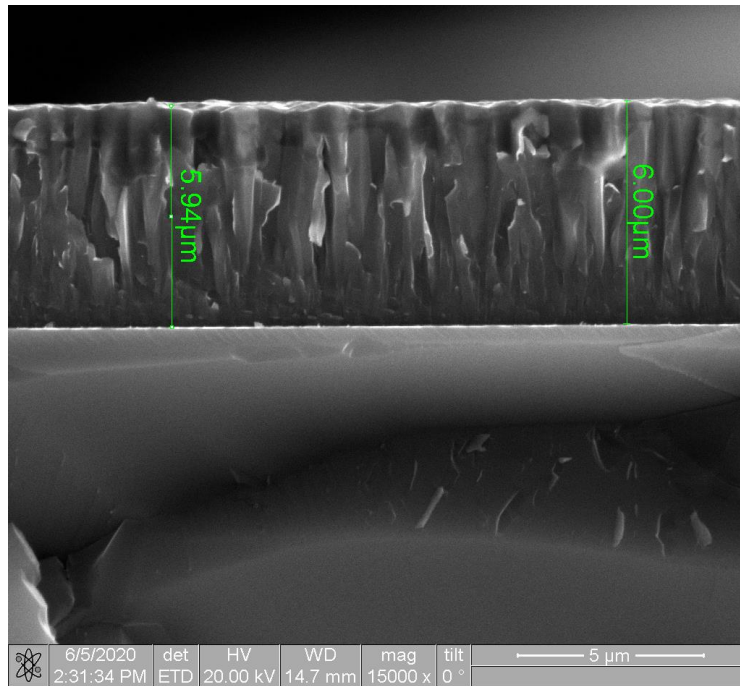
Figure 87. SEM image of magneton deposited Cr-61 result on monocrystal Si substrate.
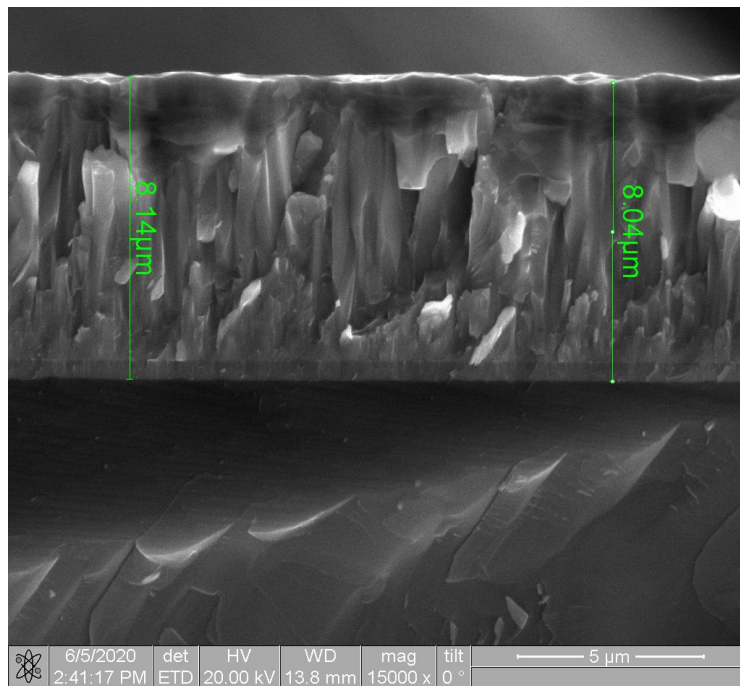
Figure 88. SEM image of magneton deposited Cr-62 result on monocrystal Si substrate.

Cr-71_0000   H   D11.1 x1.0k   100 um
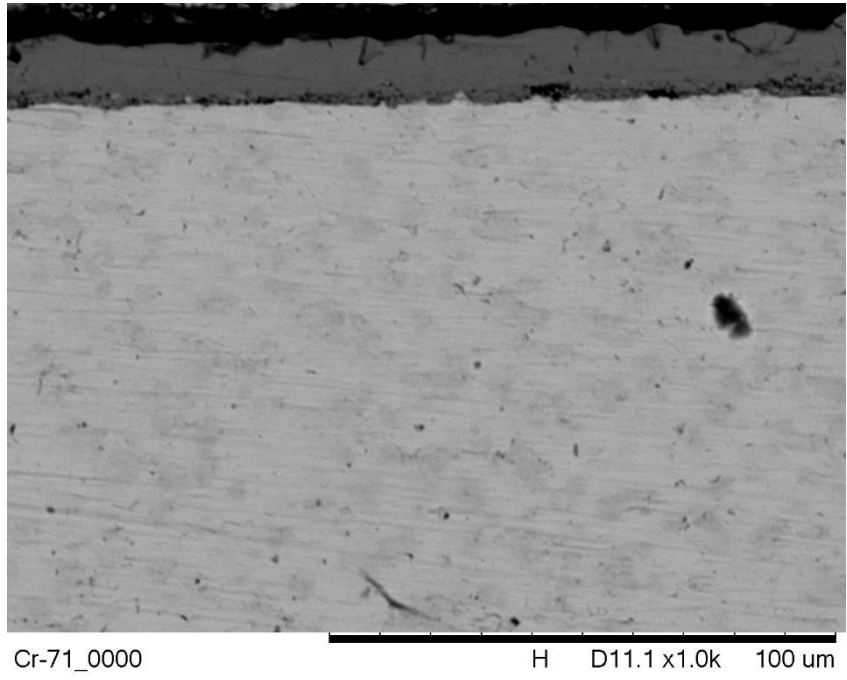
Figure 89. SEM image of electrodeposited sample (#71 - 15 μm) before oxidation test.

Cr-73_0001   H   D12.4 x5.0k   20 um
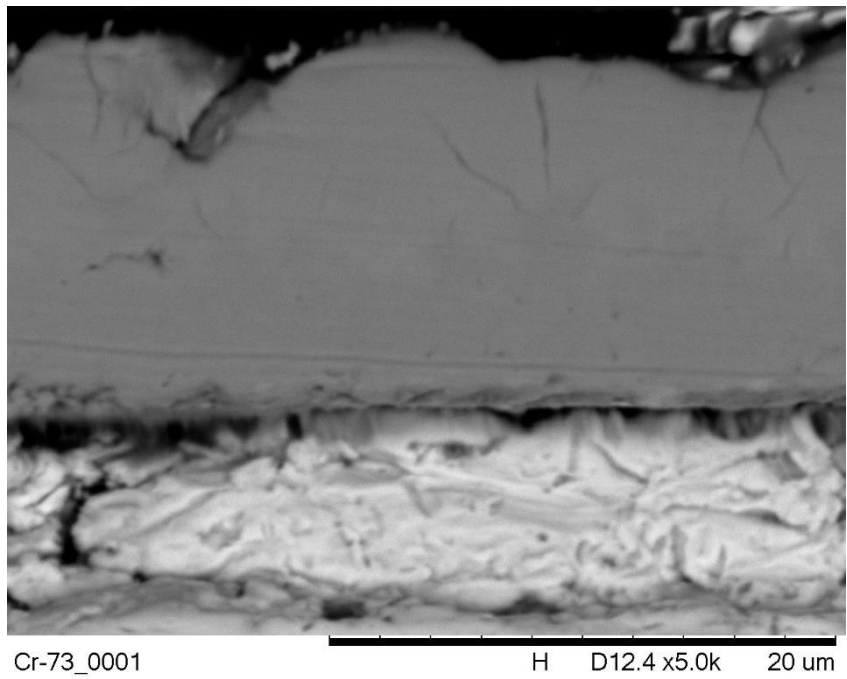
Figure 90. SEM image of electrodeposited sample (#73 - 22 μm) before oxidation test.
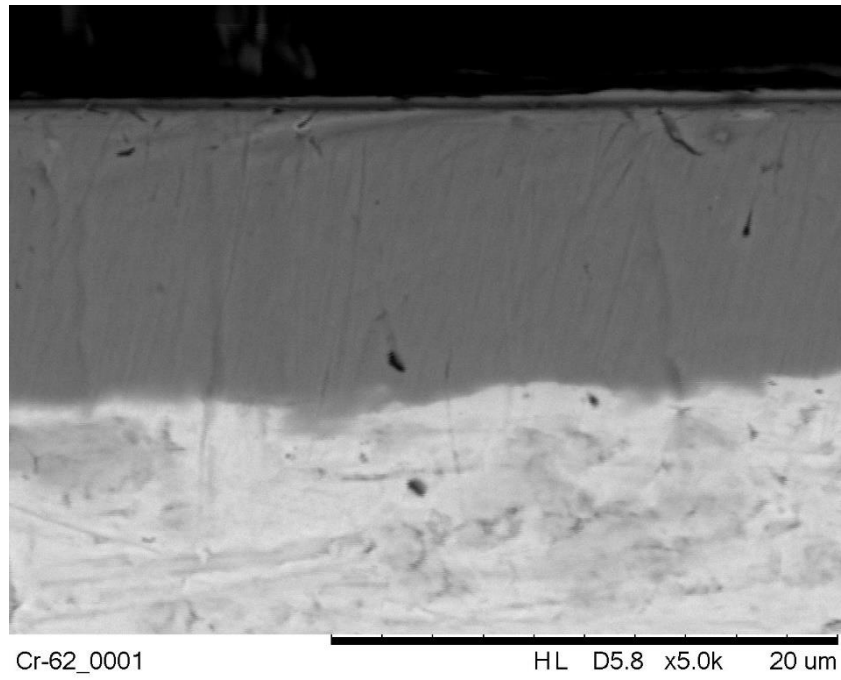
Figure 91. SEM image of magnetron-deposited sample (Cr-62 – 8.2 μm) before oxidation test.
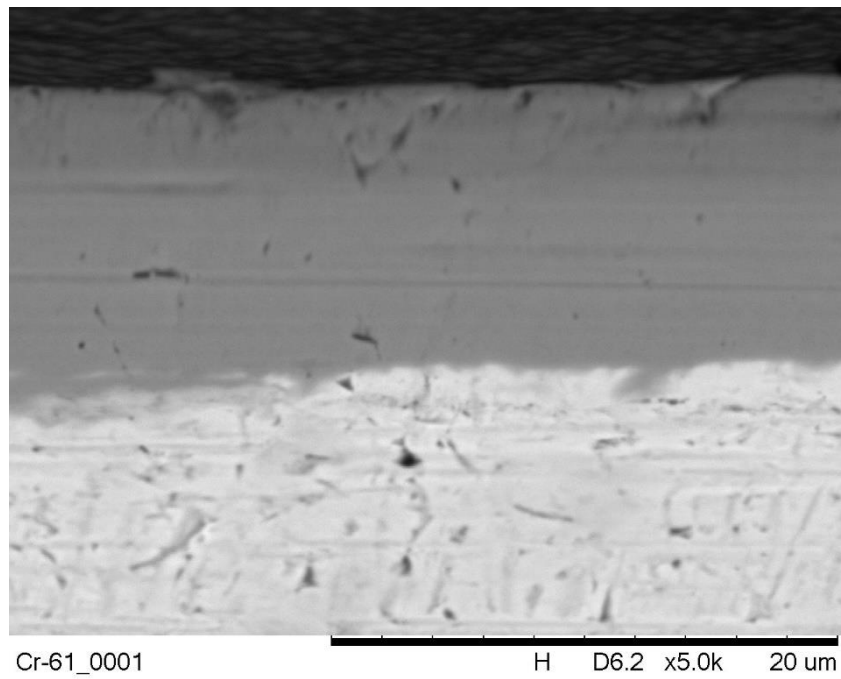
Figure 92. SEM image of magnetron-deposited sample (Cr-61 – 6 μm) before oxidation test.
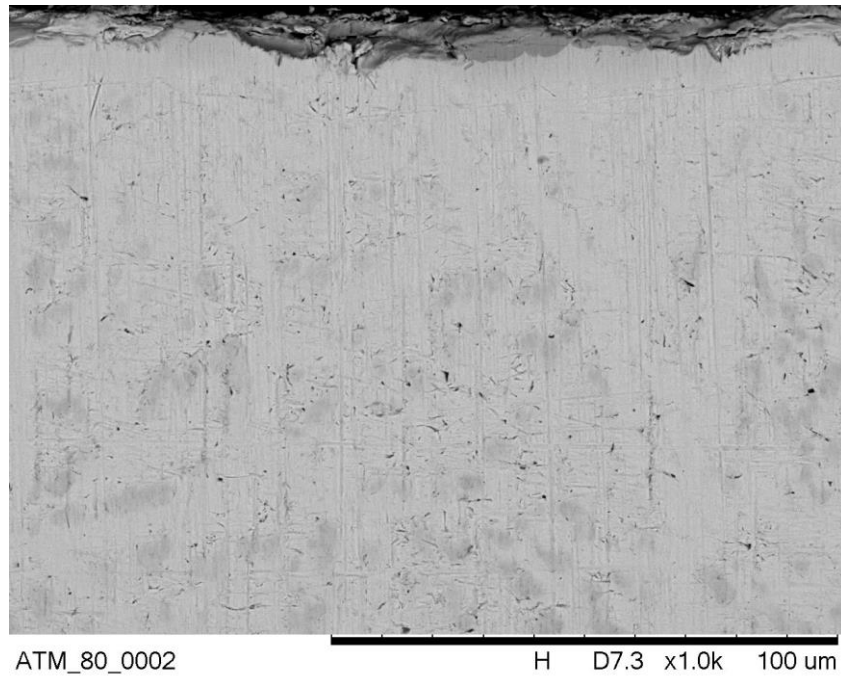
Figure 93. SEM image of electrodeposited sample (#80 - 15 µm) after oxidation test in atmosphere.
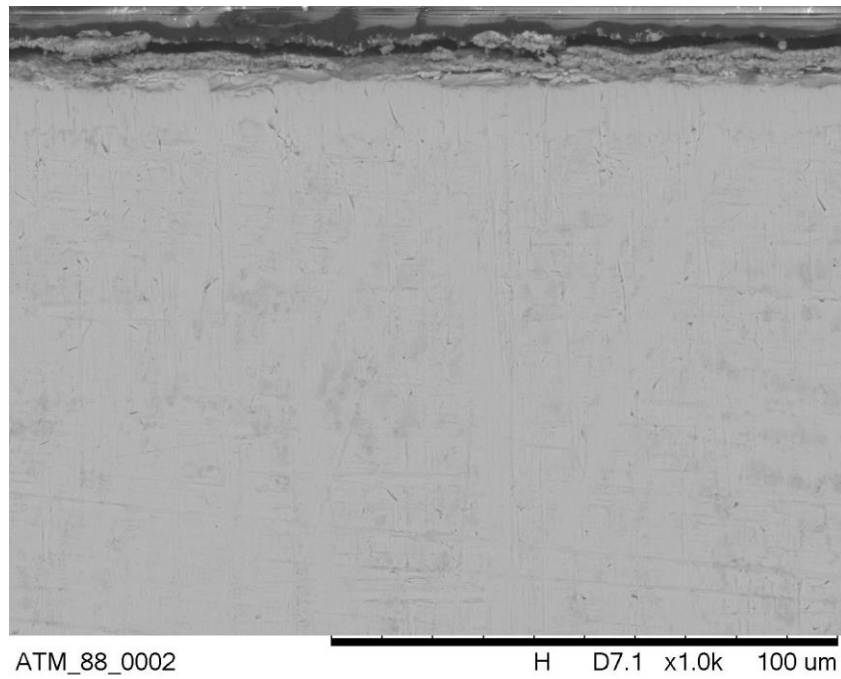
Figure 94. SEM image of electrodeposited sample (#88 – 6 µm) after oxidation test in atmosphere.
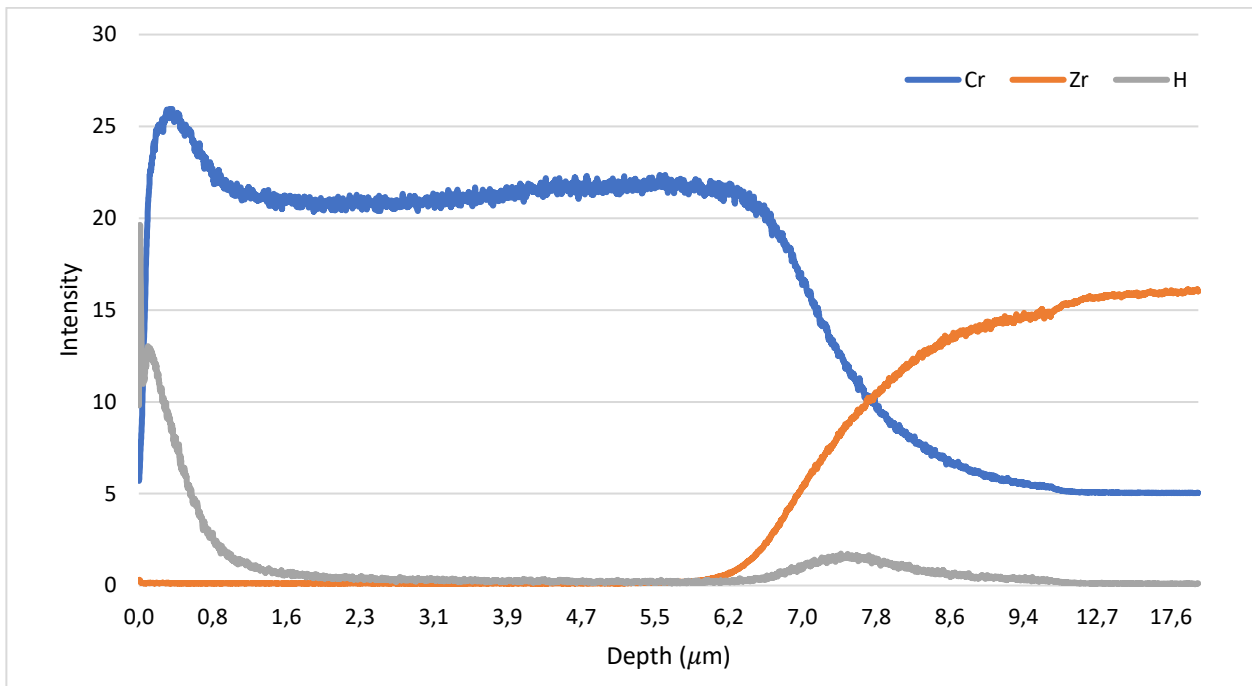
Figure 95. GDOES profile of as deposited galvanic coating (#64 - 8 µm).

e
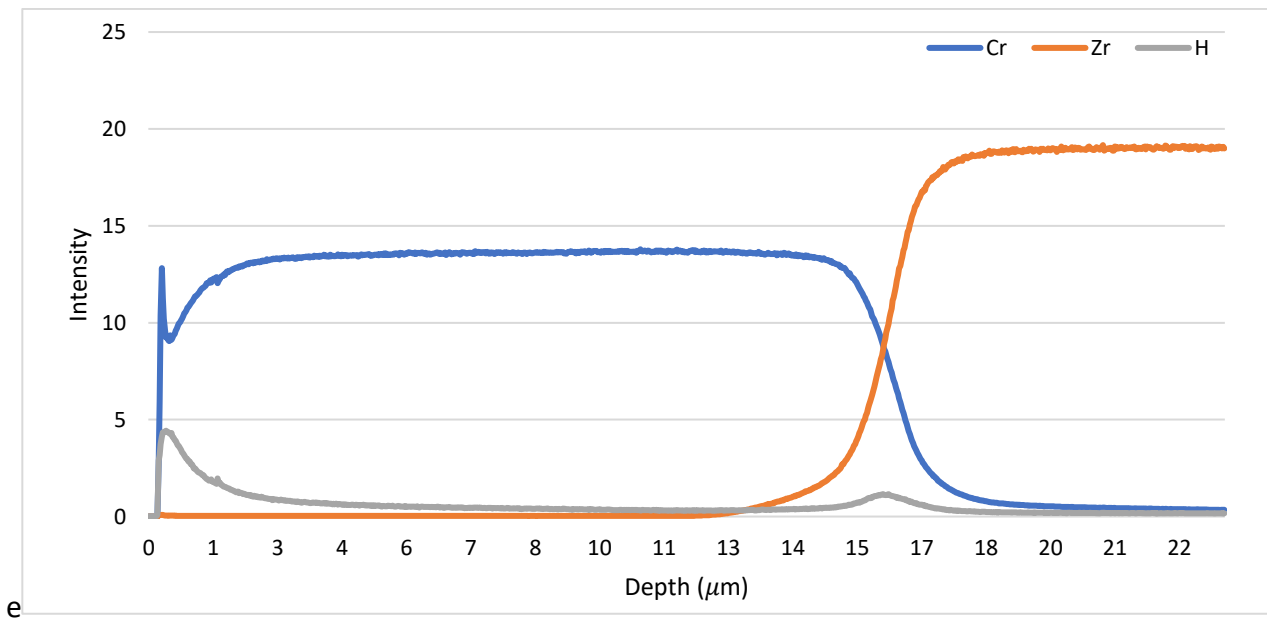
Figure 96. GDOES profile of as deposited galvanic coating (#74 – 17 µm)
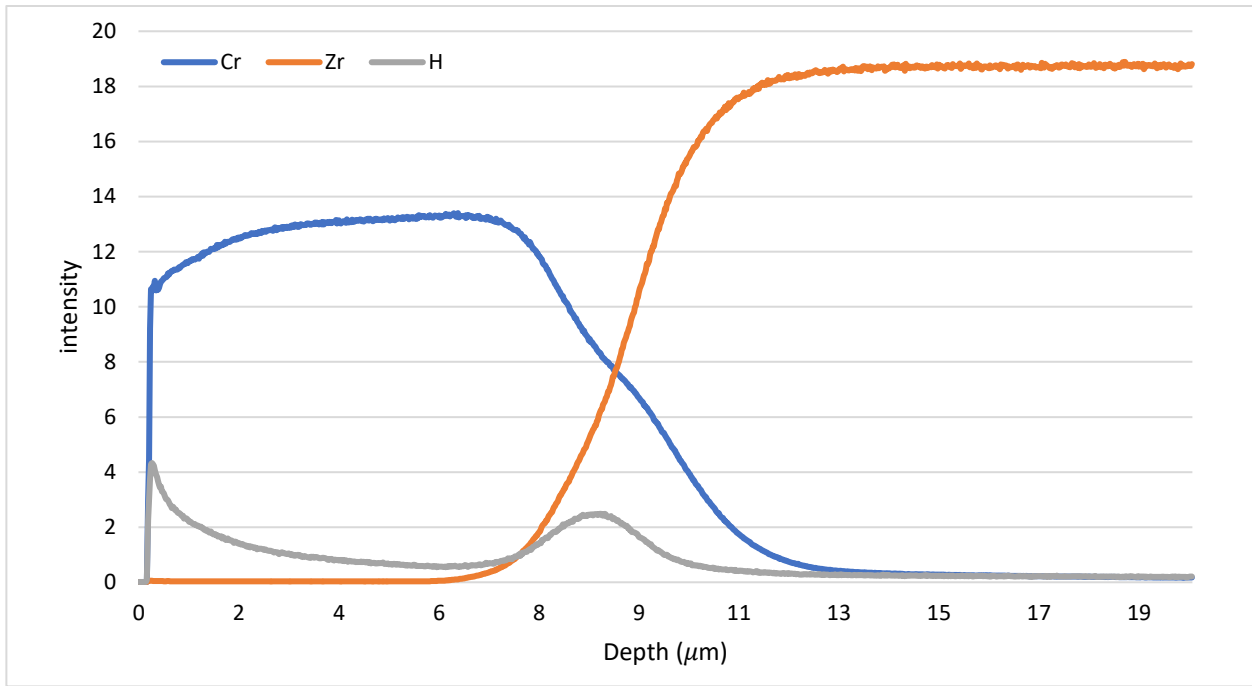
Figure 97. GDOES profile of as deposited galvanic coating (#68 – 15 μm).

GDOES after oxidation
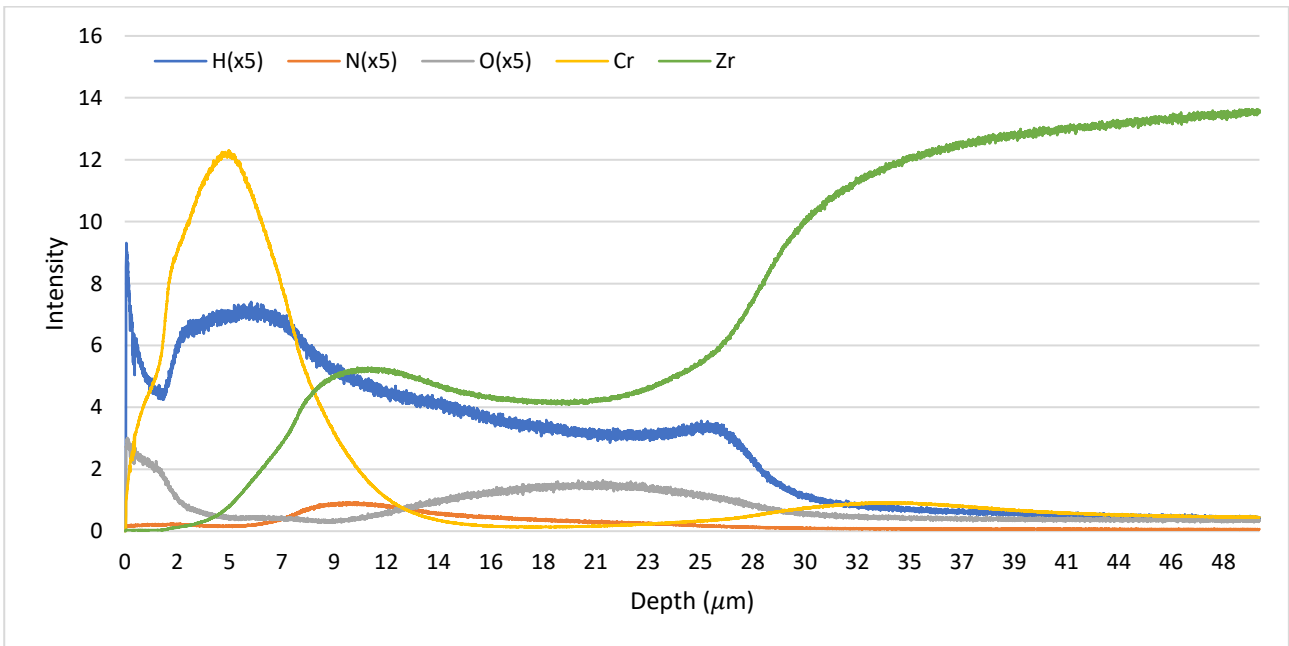
Figure 98. GDOES profile of magnetron-deposited sample (Cr-59 – 4.5 μm) after 5 min LOCA.
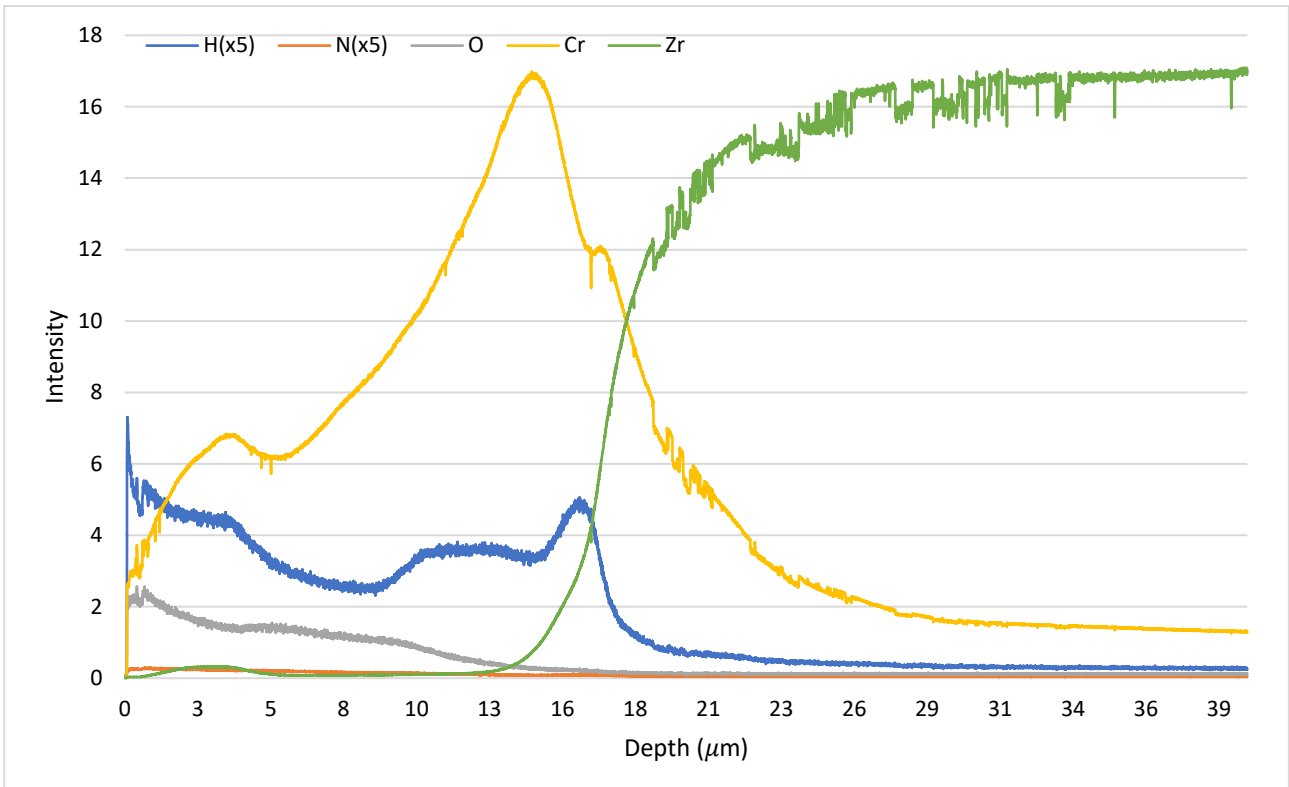
Figure 99. GDOES profile of electrodeposited sample (#76 – 18 μm) after 5 min LOCA.
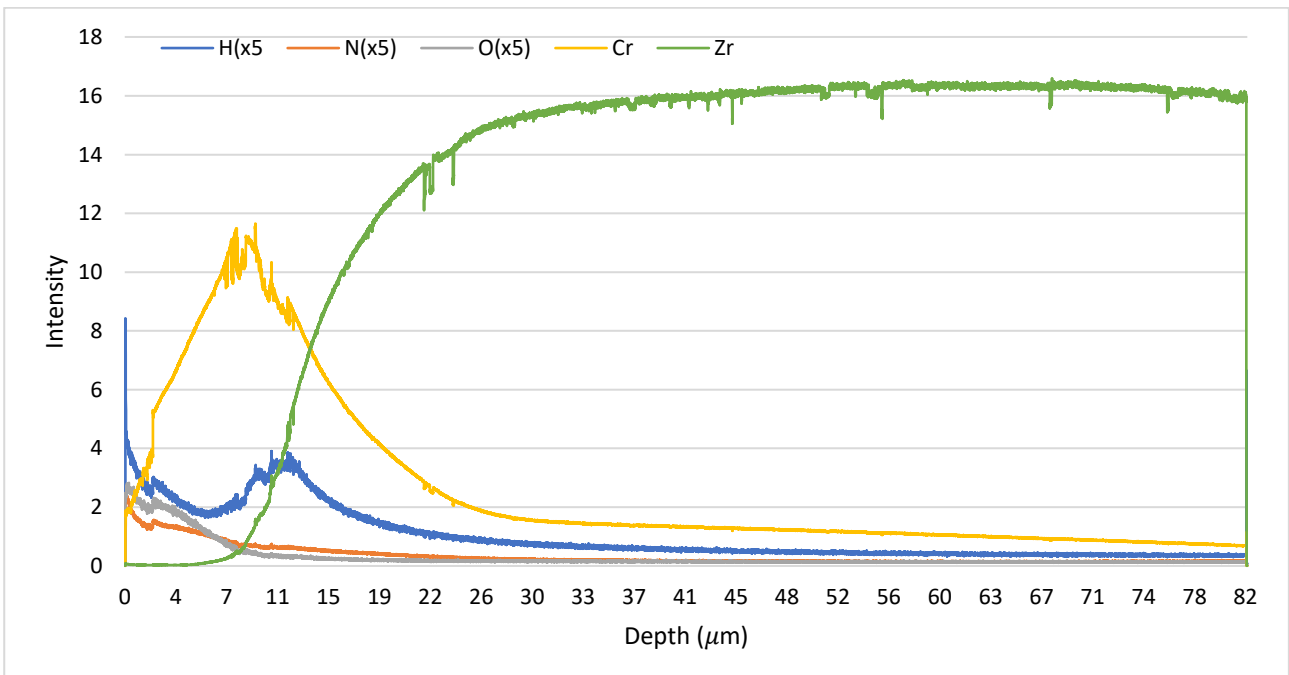
Figure 100. GDOES profile of electrodeposited sample (#84 – 8 μm) after 5 min LOCA.
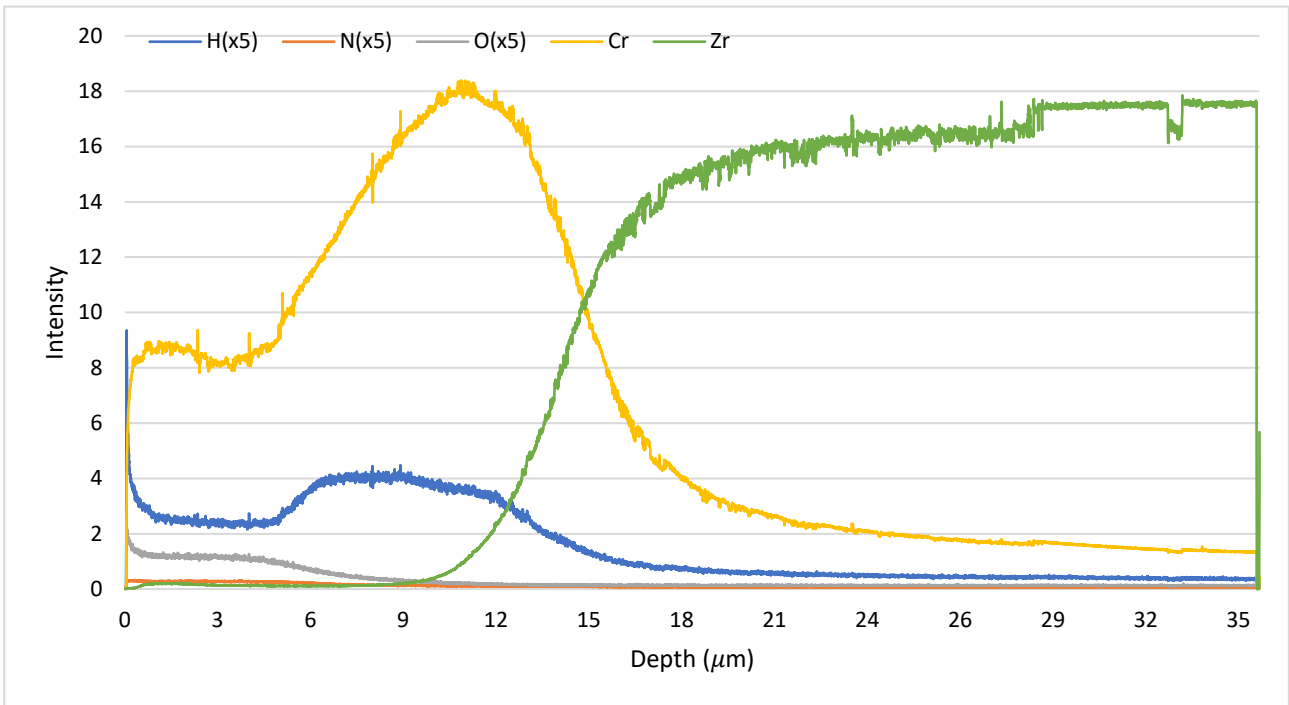
Figure 101. GDOES profile of magnetron-deposited sample (Cr-62 – 8.2 μm) after 5 min LOCA.
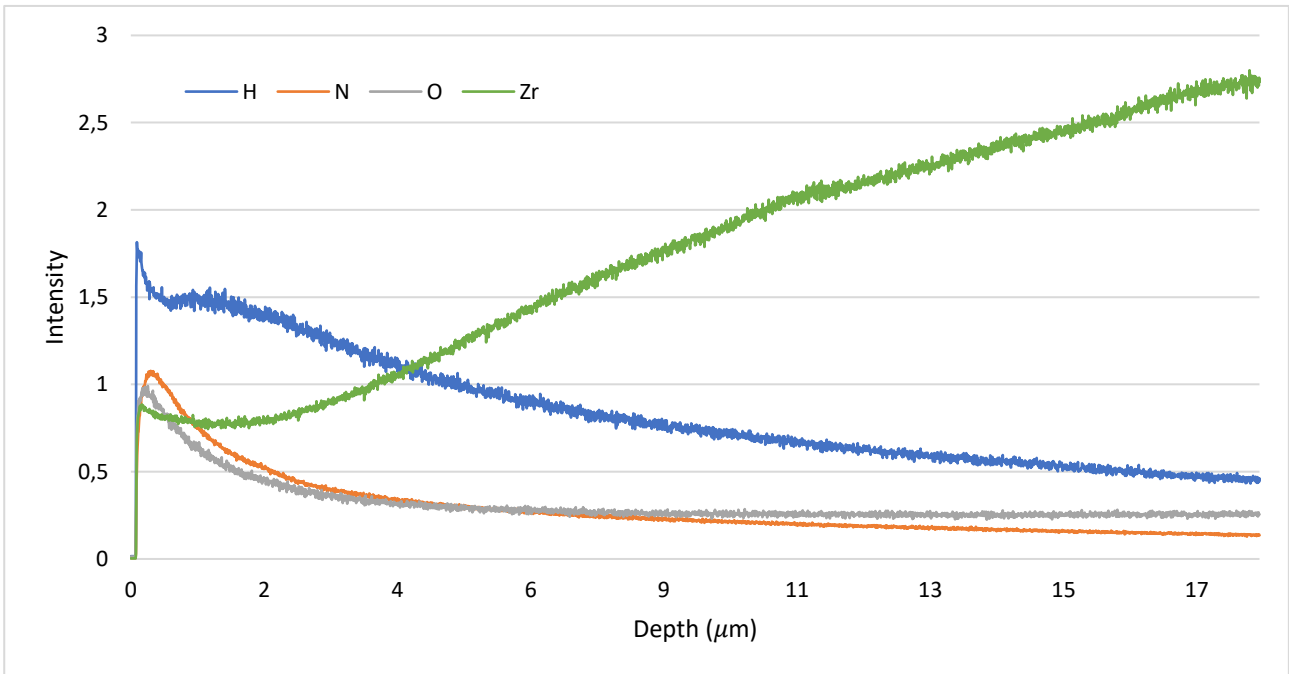
Figure 102. GDOES profile of uncoated Zr-1Nb sample after 15 min in LOCA,
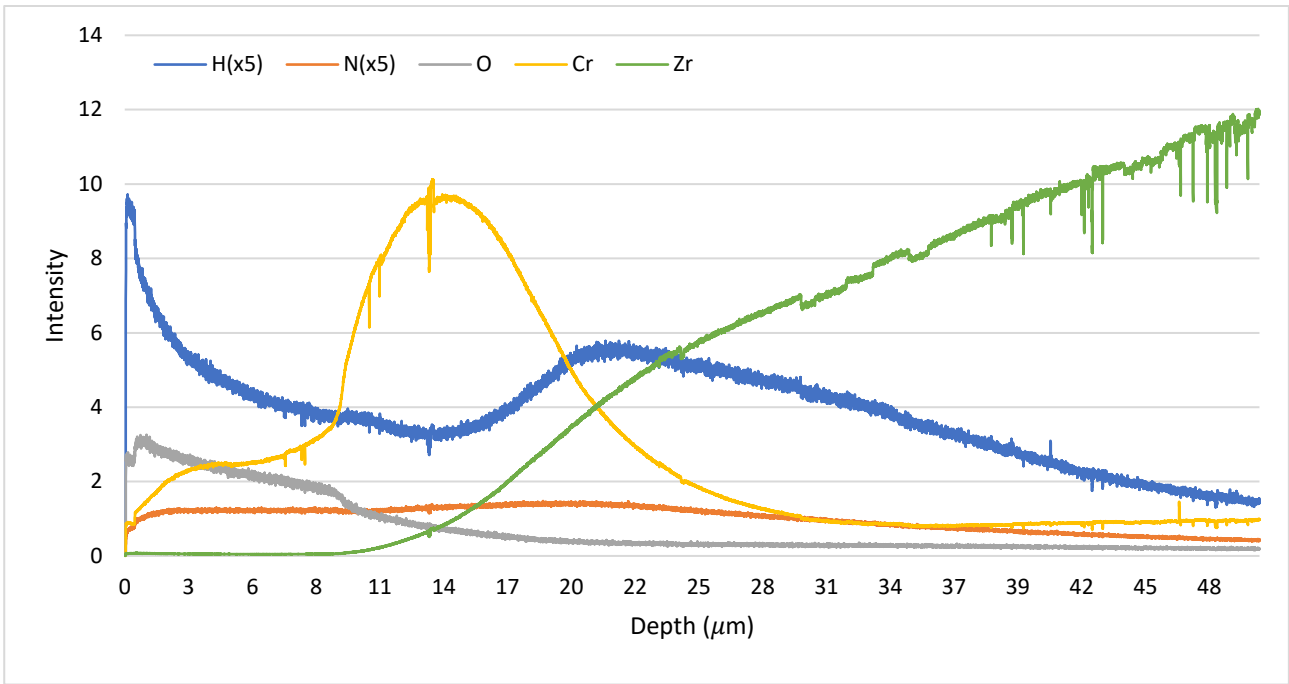
Figure 103. GDOES profile of electrodeposited sample (#82 – 17 μm) after 20 min LOCA.
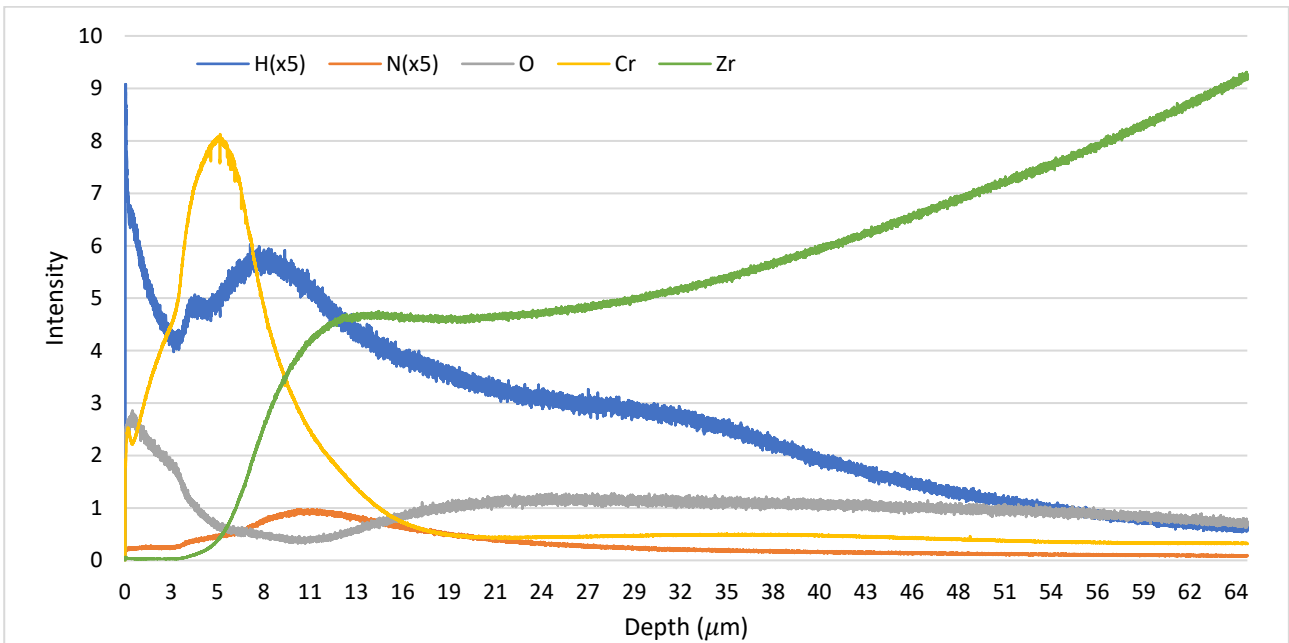
Figure 104. GDOES profile of electrodeposited sample (#86 – 9 μm) after 20 min LOCA.
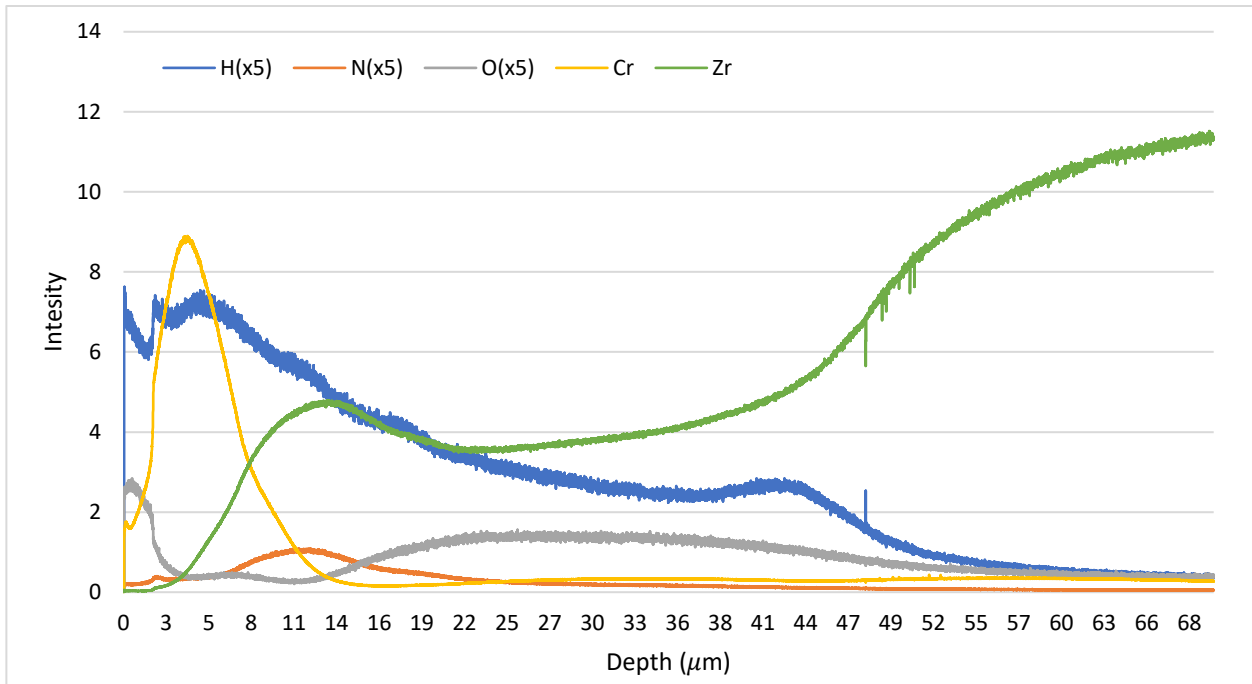
Figure 105. GDOES profile of magnetron-deposited sample (Cr-59 – 4.5 μm) after 20 min LOCA.
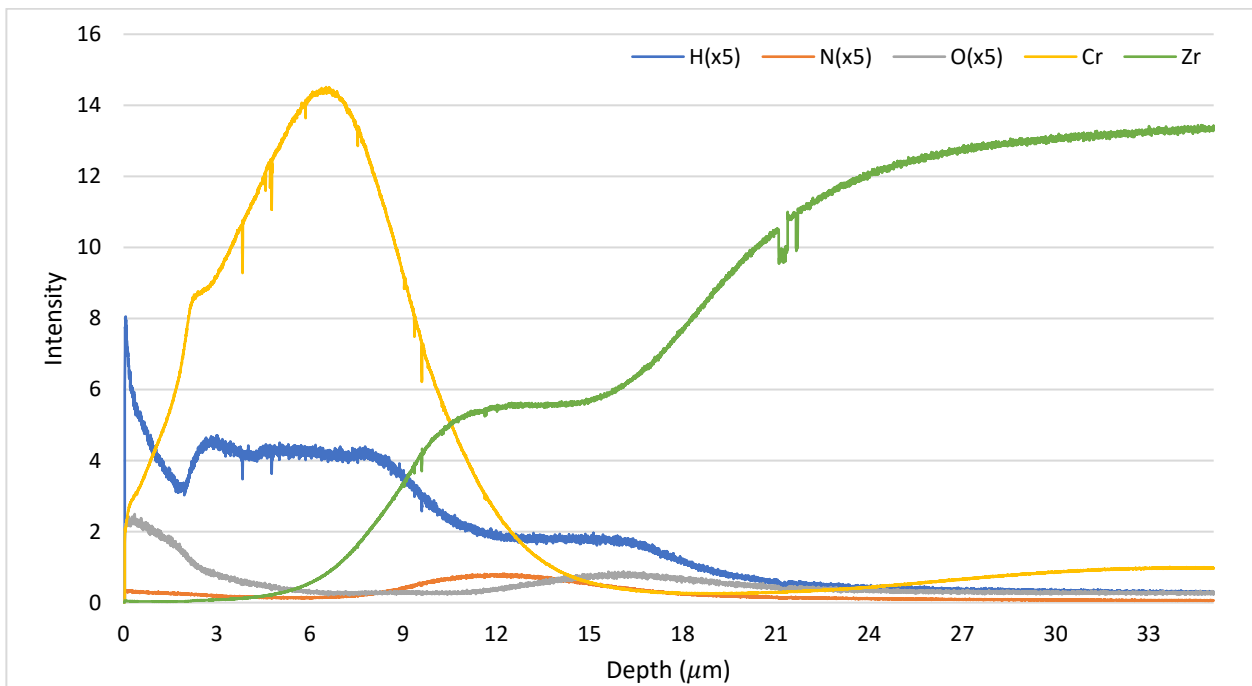
Figure 106. GDOES profile of magnetron-deposited sample (Cr-62 – 8.2 μm) after 20 min LOCA

Optical microscopy
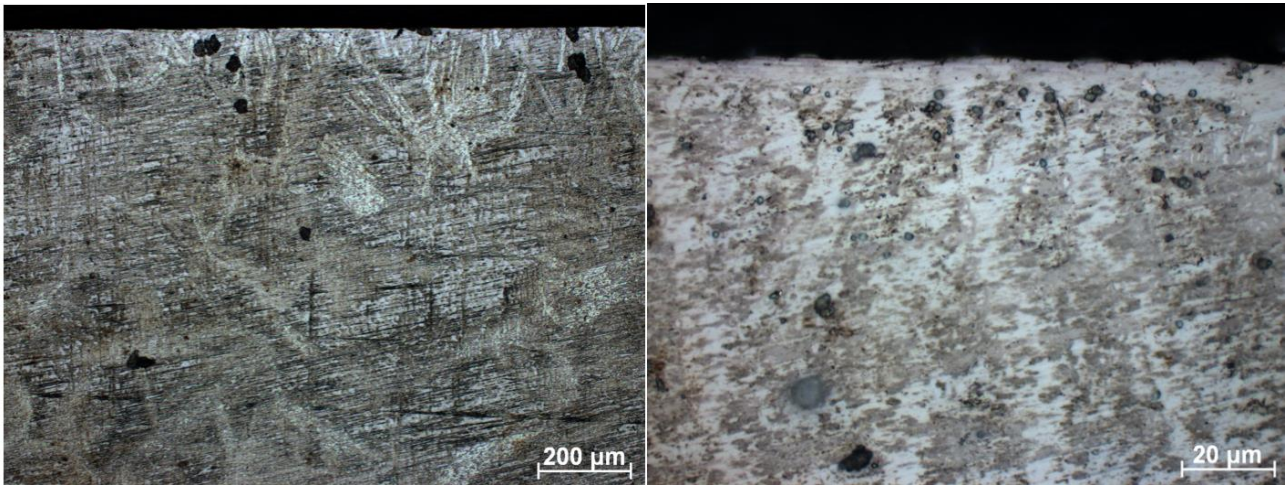
Figure 107. Optical microscopy images of magnetron-deposited sample Cr-59 – 4,5 μm after atmosphere test.
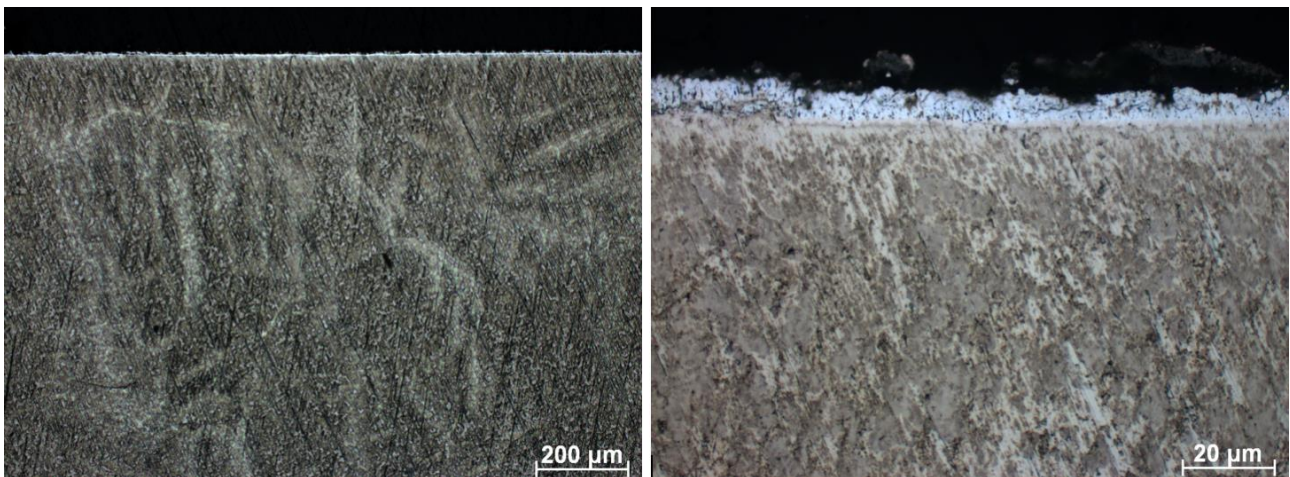
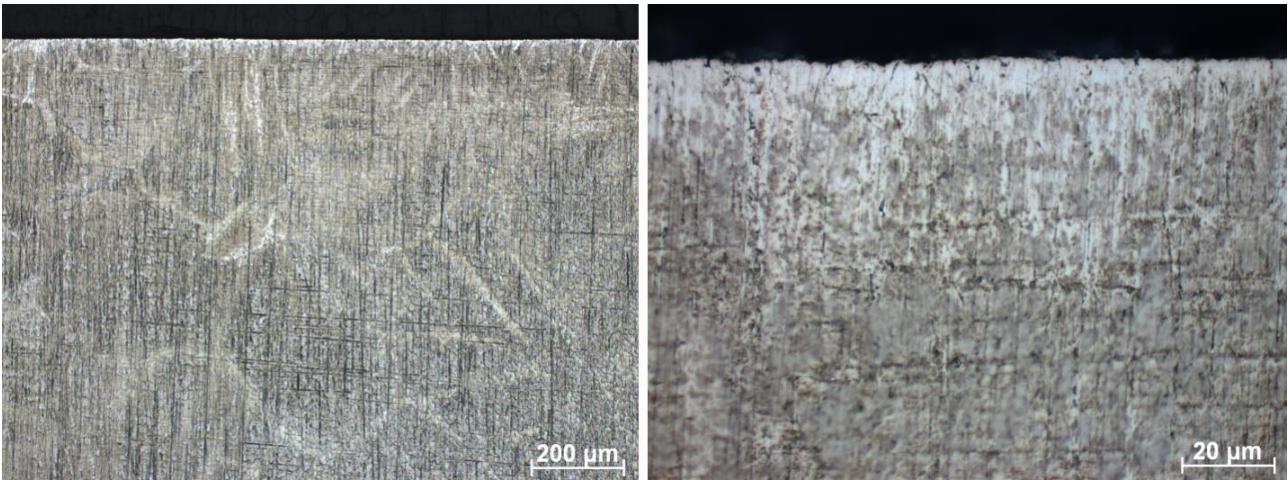**Figure 108.** Optical microscopy images for magnetron-deposited sample Cr-61 - 6 μm after atmosphere test.
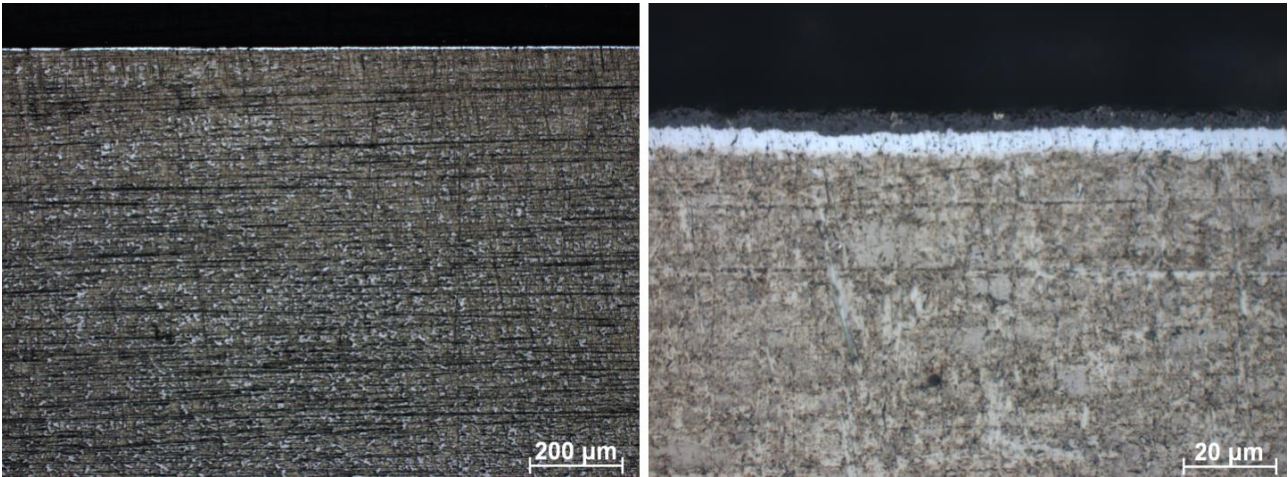
Figure 109. Optical microscopy images for magnetron-deposited sample Cr-62 – 8.2 μm after atmosphere test.

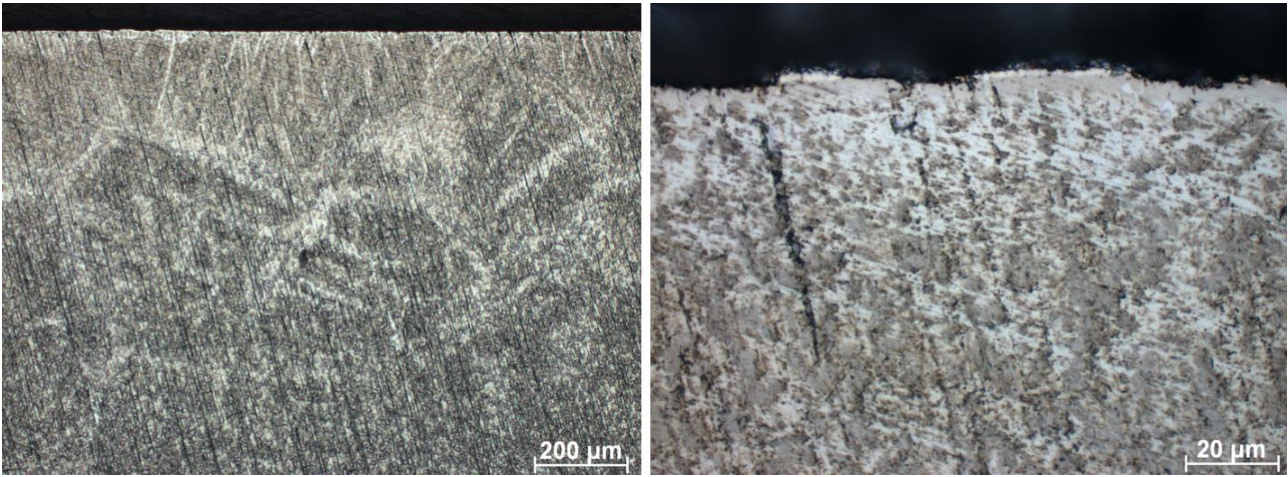**Figure 110.** Optical microscopy images for electrodeposited sample #88 - 6 μm after atmosphere test.

Figure 111. Optical microscopy images for electrodeposited sample #81 - 11 μm after atmosphere test.
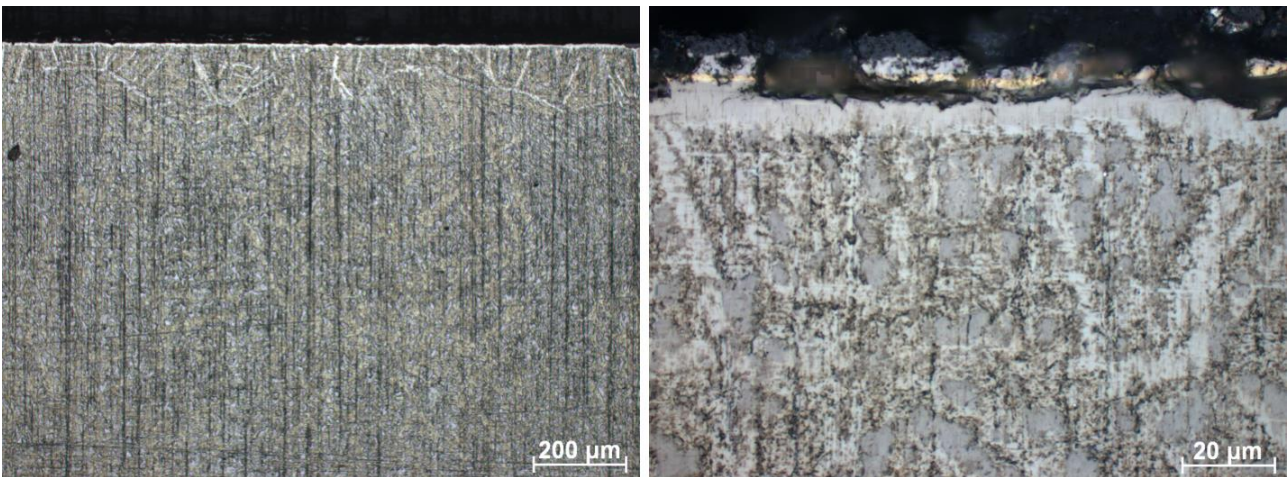

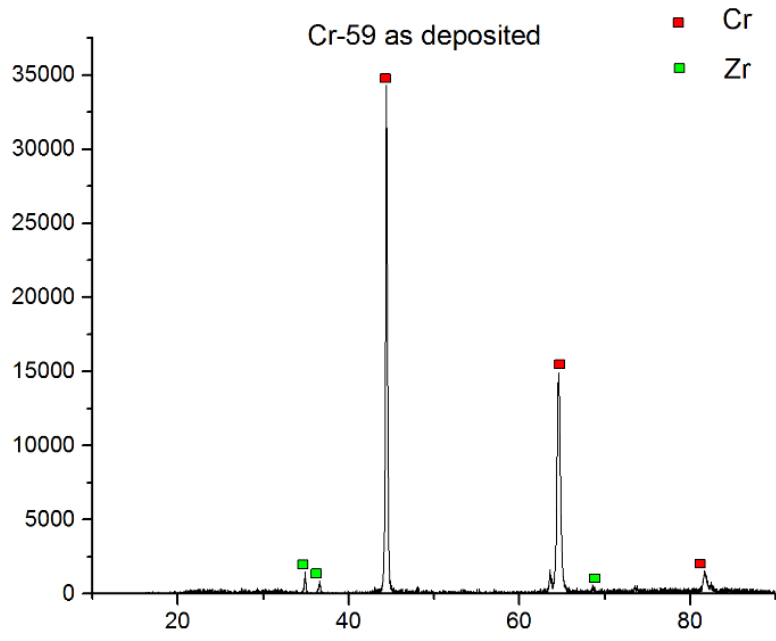**Figure 112.** Optical microscopy images for electrodeposited sample #80 - 15 μm after atmosphere test.

Figure 113. XRD pattern of magnetron-deposited sample (Cr-59 – 4.5μm).
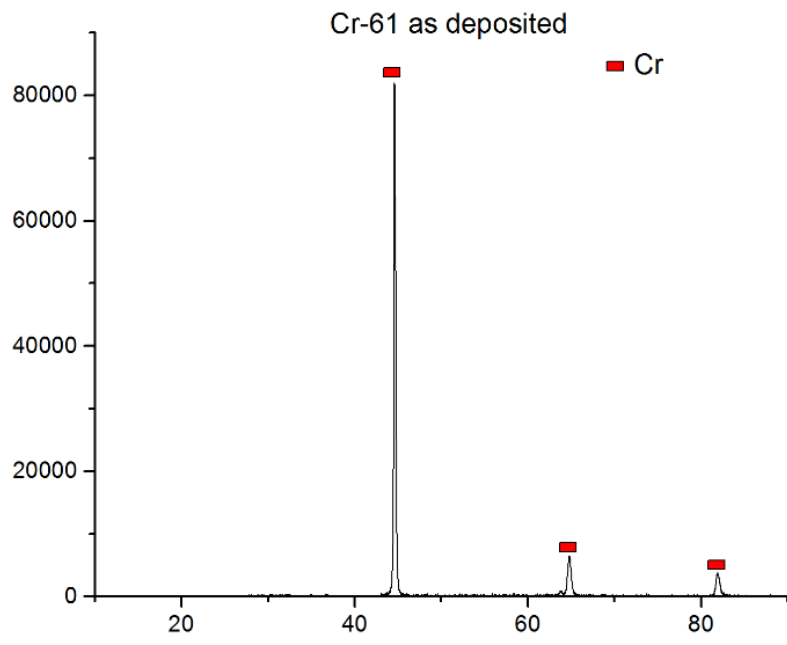

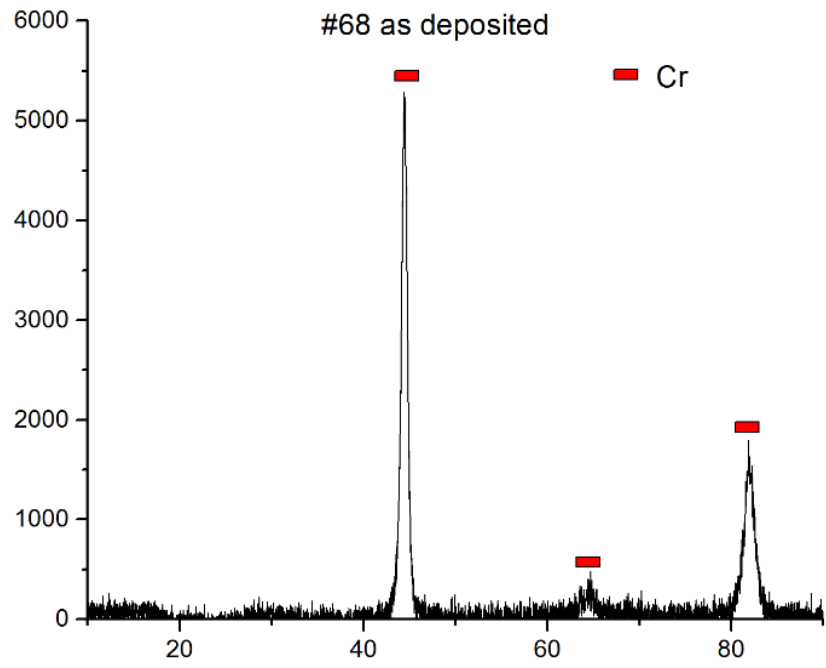**Figure 114.** XRD pattern of magnetron-deposited sample (Cr-61 – 6 μm).

144

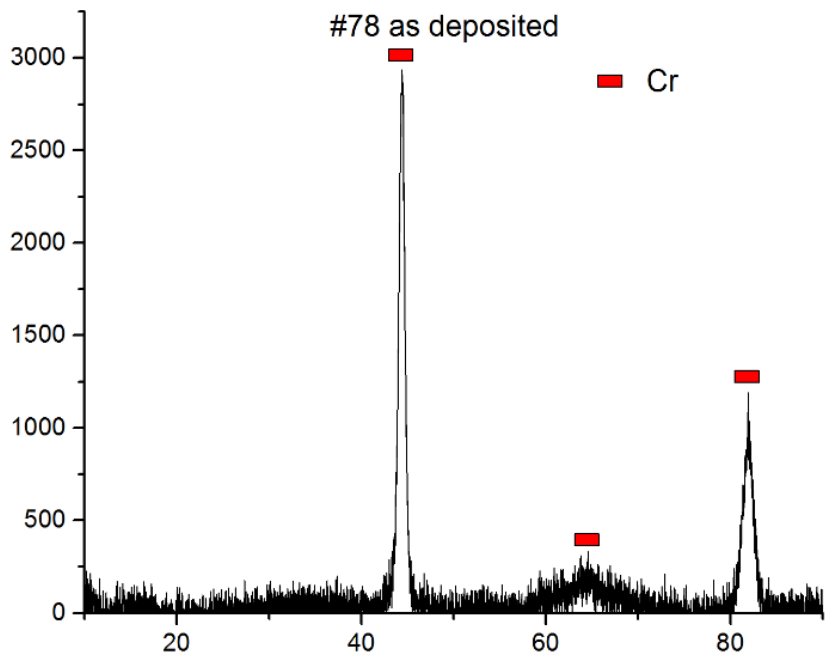**Figure 115.** XRD pattern of electrodeposited sample (#68 – 14 μm).

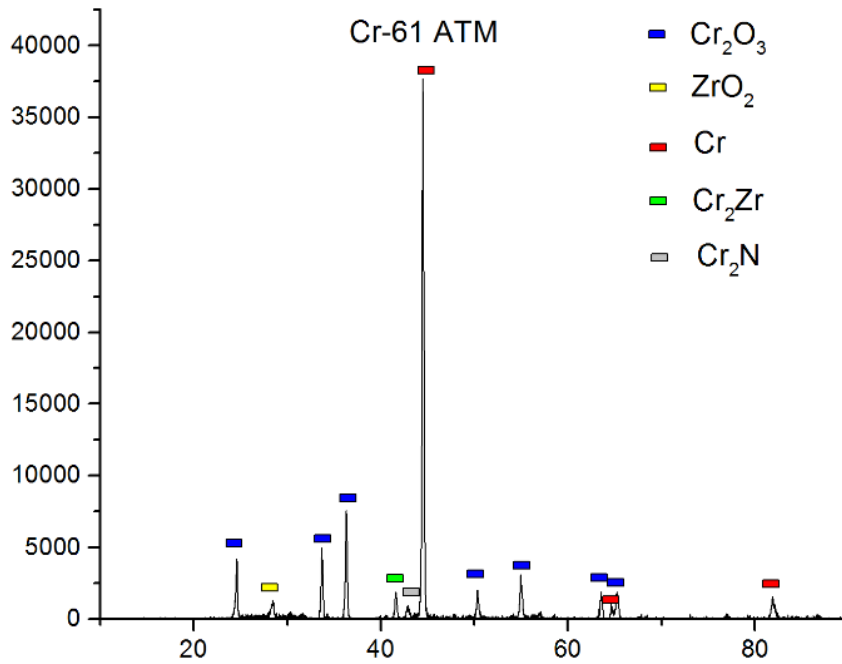**Figure 116.** XRD pattern of electrodeposited sample (#78 – 12 μm).

Figure 117. XRD pattern of magnetron-deposited sample (Cr-61 - 6 um) after atmospheric oxidation.
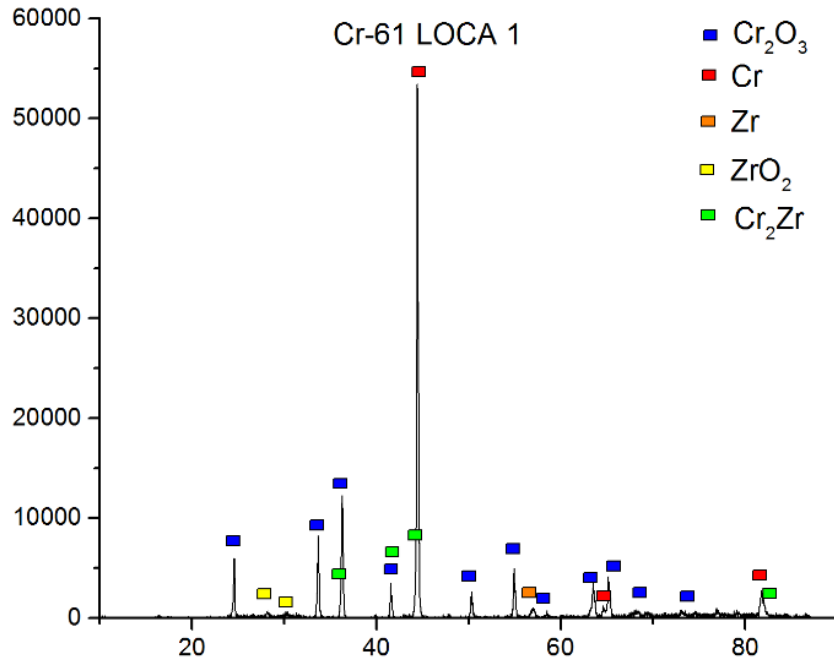

Figure 118. XRD pattern of magnetron-deposited sample (Cr-61 - 6 um) after 5 min in LOCA.
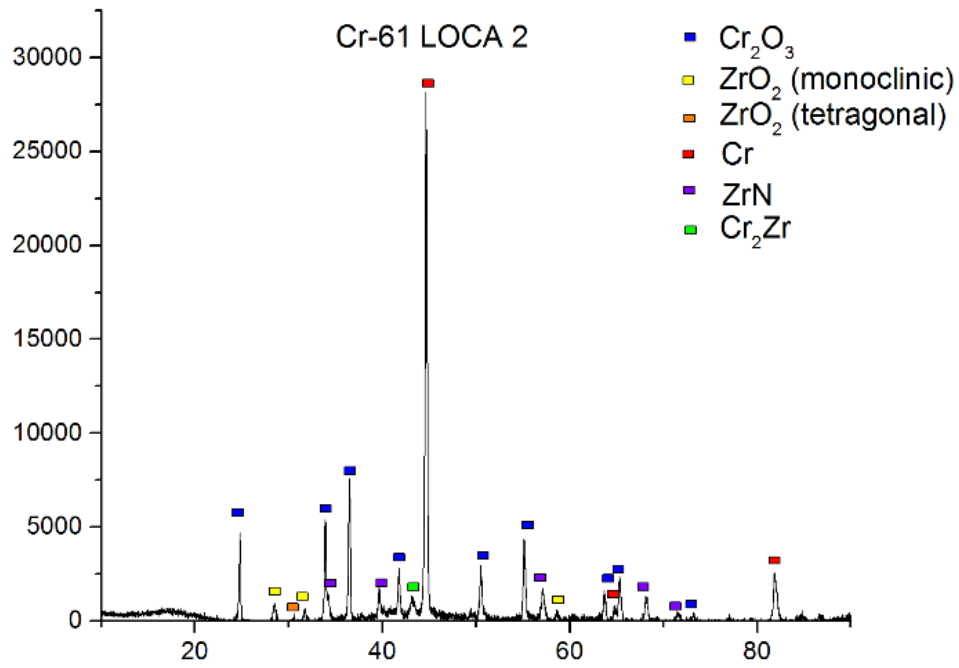
Figure 119. XRD pattern of magnetron-deposited sample (Cr-61 - 6 um) after 20 min in LOCA.
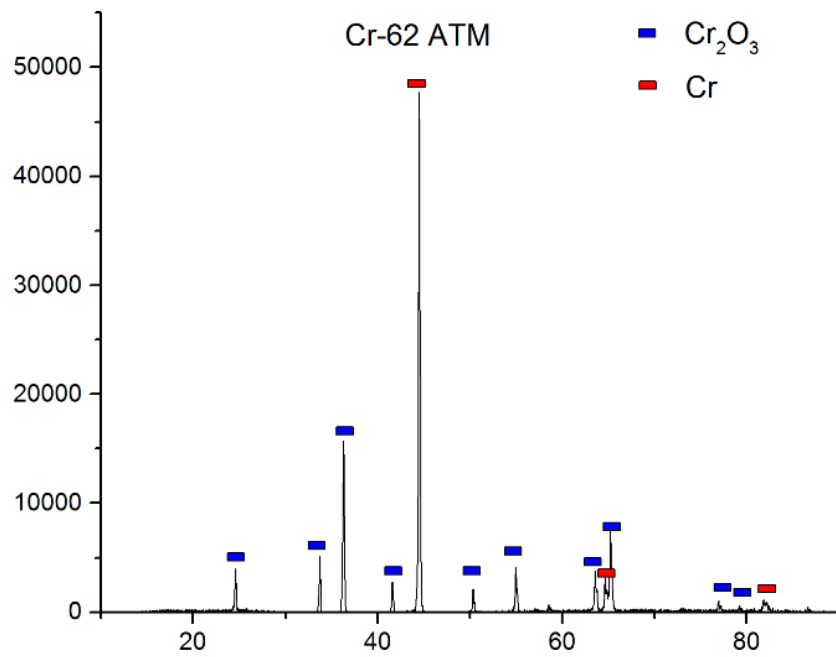

Figure 120. XRD pattern of magnetron-deposited sample (Cr-62 – 8.2 um) after atmospheric oxidation.
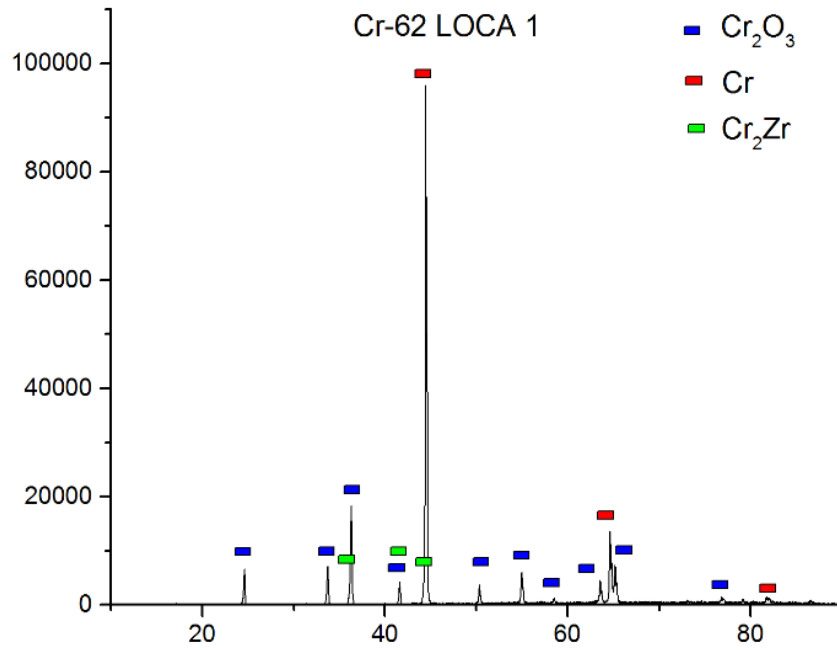
Figure 121. XRD pattern of magnetron-deposited sample (Cr-62 – 8.2 um) after 5 min in LOCA.

Figure 122. XRD pattern of magnetron-deposited sample (Cr-62 – 8.2 um) after 20 min in LOCA.

Figure 123. XRD pattern of electrodeposited sample (#76 - 18 um) after 5 min in LOCA.

Figure 124. XRD pattern of electrodeposited sample (#77 - 12 μm) after 5 min in LOCA.

Figure 125. XRD pattern of electrodeposited sample (#80 - 15 μm) after atmospheric oxidation.

Figure 126. XRD pattern of electrodeposited sample (#81 - 11 μm) after atmospheric oxidation.
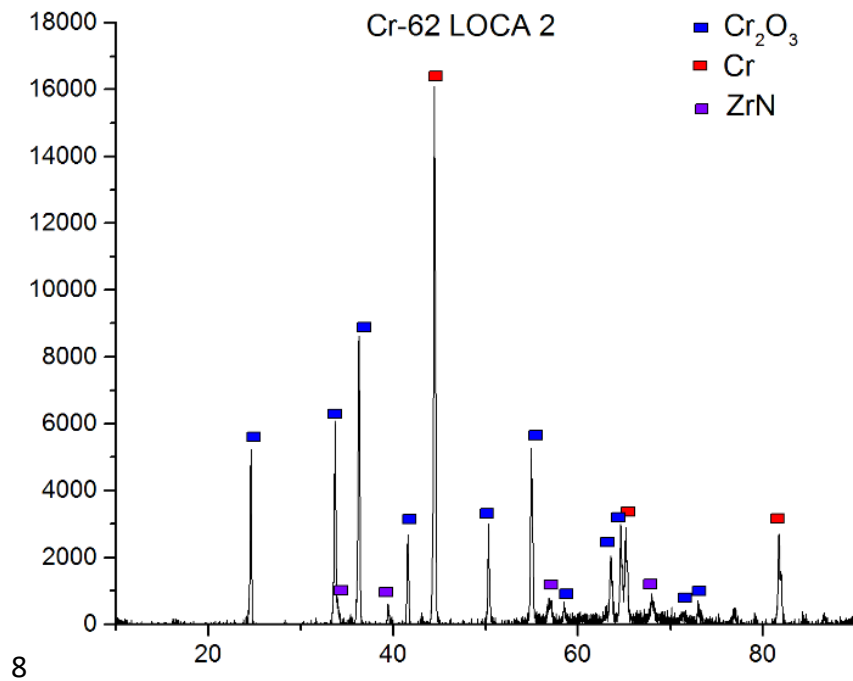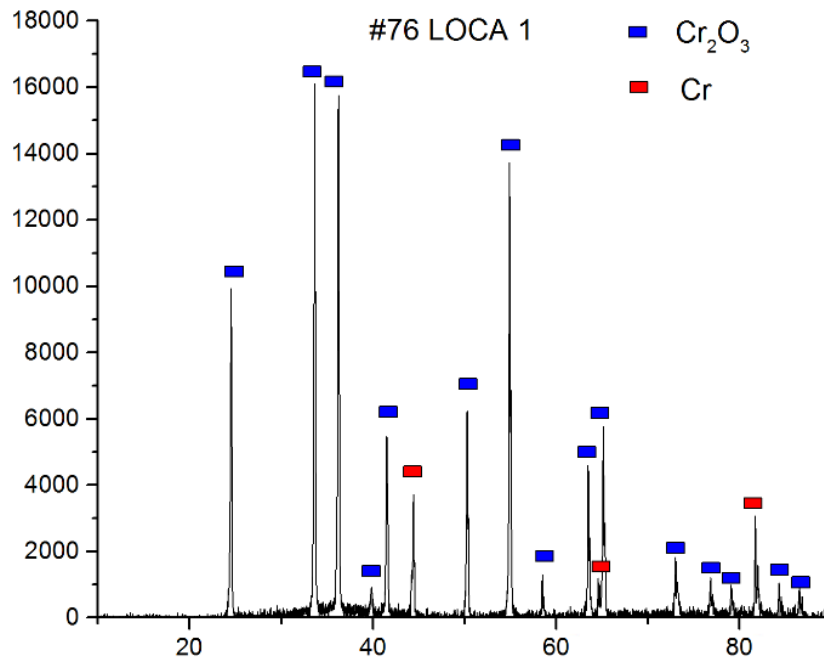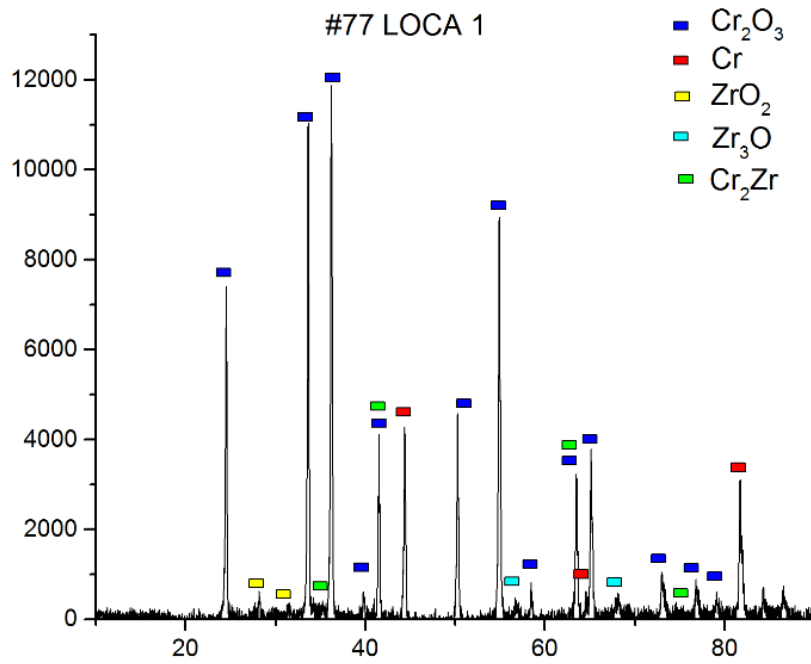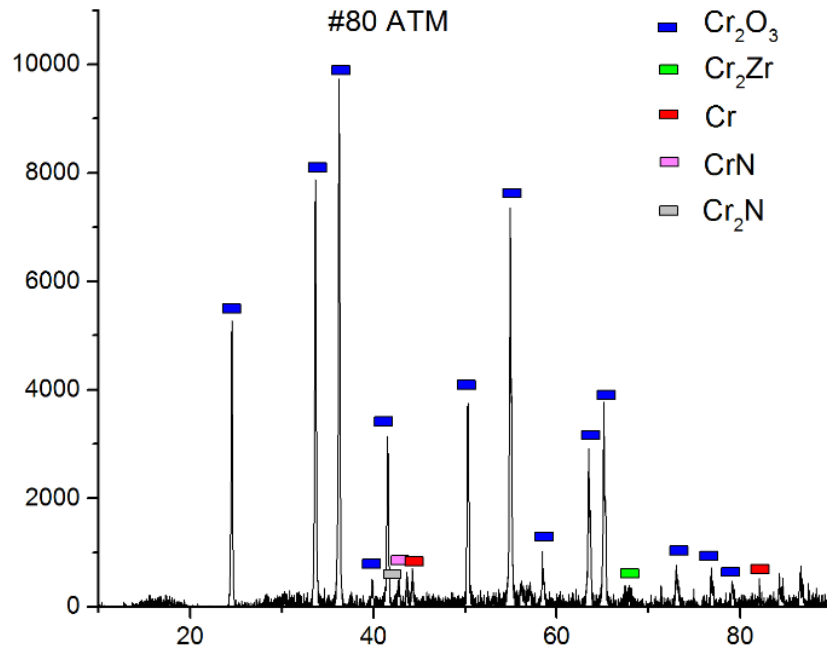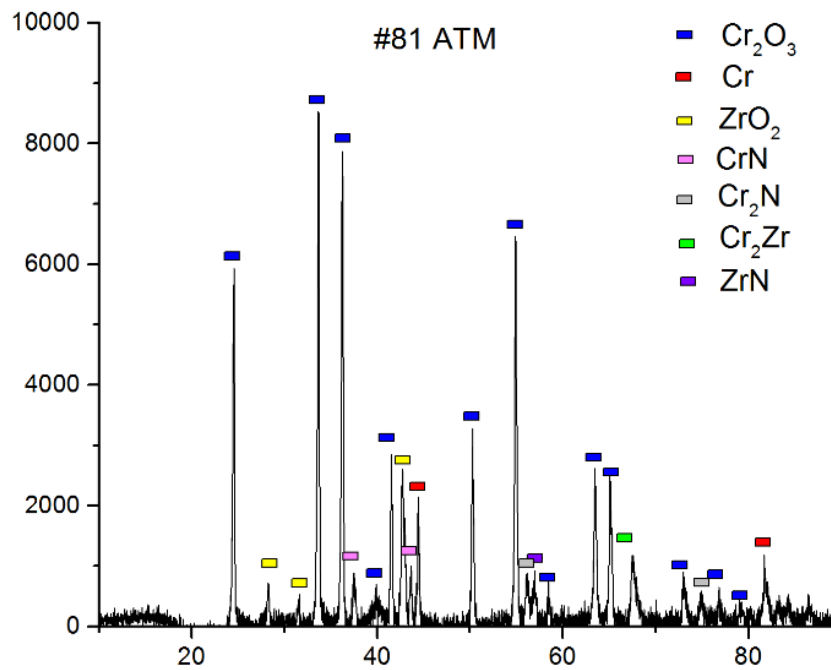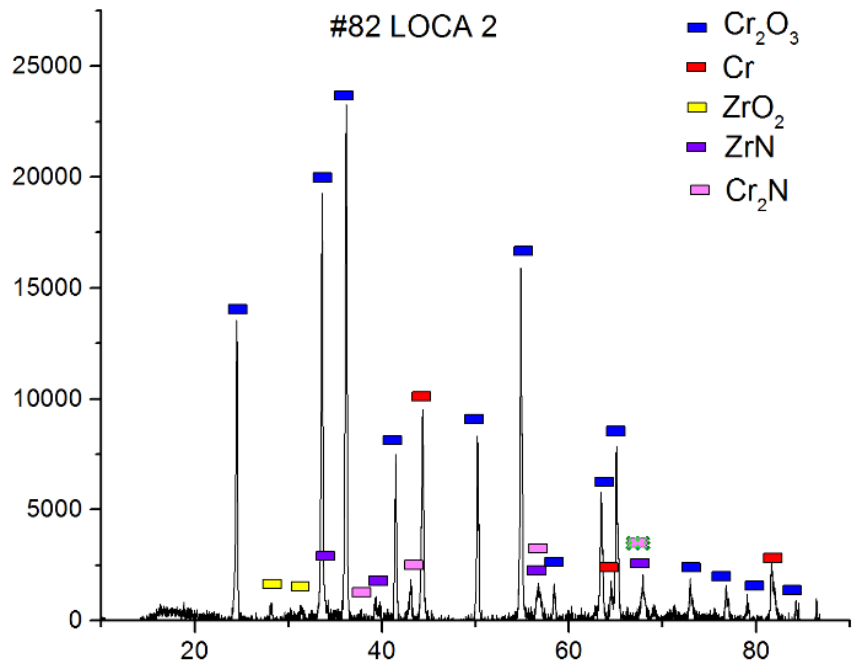
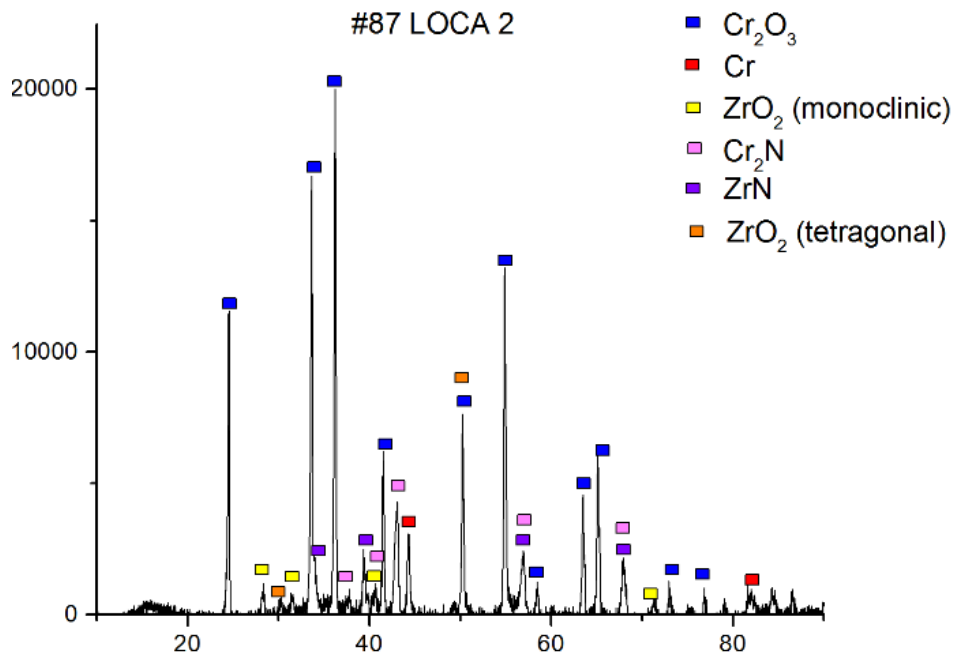**Figure 127.** XRD pattern of electrodeposited sample (#82 - 17 μm) after 20 min in LOCA.

Figure 128. XRD pattern of electrodeposited sample (#87 - 12 μm) after 20 min in LOCA.

BIBLIOGRAPHY

[1] C. Tang, M. Stueber, H. J. Seifert, M. Steinbrueck, Protective coatings on zirconium-based alloys as accident-tolerant fuel (ATF) claddings, Corros Rev (2017) 1-25.

[2] *Statista*. Retrieved march 24, 2020, from https://www.statista.com/statistics/267158/number-of-nuclear-reactors-in-operation-by-country/.

[3] V. Kortov, Y. Ustyantsev, Chernobyl accident: Causes, consequences and problems of radiation measurements, Radiation Measurements (2016) 12-16.

[4] C. Tang, M. Stueber, H. J. Seifert, M. Steinbrueck, Protective coatings on zirconium-based alloys as accident-tolerant fuel (ATF) claddings, Corros Rev (2017) 1-25.

[5] T.R. Allen, R.J.M. Konings, A.T. Motta, Corrosion of zirconium alloys, Elsevier (2012).

[6] S.J. Zinkle, K.A. Terrani, J.C. Gehin, L.J. Ott, L.L. Snead, Accident tolerant fuels for LWRs: A perspective, Journal of Nuclear Materials (2014) 374-379.

[7] R. McCullum, Combustibili per reattori, Le Scienze (2019) 611-612.

[8] Canadian Nuclear Safety Commission, The Science of Safety: CNSC Research Report 2016–17, (2018)

[9] A. Etchepareborda, C. A. Flury, Multivariable robust control of an integrated nuclear power reactor, Brazilian Journal of Chemical Engineering (2002).

[10] Z. Duan, H. Yang, Y. Satoh, K. Murakami, S. Kano, Z. Zhao, J. Shen, H. Abe, Current status of materials development of nuclear fuel cladding tubes for light water reactors, Nuclear Engineering and Design (2017) 131-150.

[11] K. A. Terrani, Accident tolerant fuel cladding development: Promise, status, and challenges, Journal of Nuclear Materials (2018) 13-30.

[12] R.B. Rebak, Accident-Tolerant Materials for Light Water Reactor Fuels, Elsevier (2020).

[13] J. C. Brachet, I. Idarraga-Trujillo, M. Le Flem, M. Le Saux, V. Vandenberghe, S. Urvoy, E. Rouesne, T. Guilbert, C. Tof-folon-Masclet, M. Tupin, C. Phalippou, F. Lomello, F. Schuster, A. Billard, G. Velisa,C. Ducros, F. Sanchette, Early studies on Cr-Coated Zircaloy-4 as enhanced accident tolerant nuclear fuel claddings for light water reactors, Journal of Nuclear Materials (2019) 268-285.

[14] J.C. Brachet, M. Le Saux, M. Le Flem, S. Urvoy, E. Rouesne, T. Guilbert, C. Cobac, F. Lahogue, J. Rousselot, M. Tupin, P. Billaud, C. Hossepied, On-going studies at CEA on chromium coated zirconium based nuclear fuel claddings for enhanced accident tolerant LWRs fuel, TopFuel (2015) 1-8.

[15] J. T. Gudmundsson, D. Lundinc, High Power Impulse Magnetron Sputtering, Elsevier (2020).

[16] J.C. Brachet, T. Guilbert, M. Lesaux, J. Rousselot, G. Nony, et al., Behavior of Cr-coated M5 claddings during and after high temperature steam oxidation from 800 °C up to 1500 °C, Topfuel (2018) 1-11.

[17] A. T. Motta, A. Couet, R. J. Comstock, Corrosion of Zirconium Alloys Used for Nuclear Fuel Cladding, Mater. Res. (2015) 311-345.

[18] K.G. Geelhood, W.G. Luscher, Degradation and Failure Phenomena of Accident Tolerant Fuel Concepts: Chromium Coated Zirconium Alloy Cladding, Pacific Northwest National Laboratory (2019).

[19] Z.G. Zhang, Z.H. Feng, X.J. Jiang, X.Y. Zhang, M.Z. Ma, R.P. Liu, Microstructure and tensile properties of novel Zr–Cr binary alloys processed by hot rolling, Materials Science & Engineering (2016) 77–83.

[20] X. Wenxin, Y. Shihao, Reaction Diffusion in Chromium-Zircaloy-2 System, Nuclear Power Institute of China, (2001).

[21] P. A. Dearnley, Introduction to Surface Engineering, Cambridge University Press (2017).

[22] D.E. Wax, R.L. Cowan, Process for electroplating zirconium alloys, US patent n° 4,017,368 (1977).

[23] D. Hartshorn, Plating titanium and zirconium and their alloys with nickel, chromium and other heavy metals, US patent n° 3,725,217 (1970).

[24] R. W. Ludwig, Corrosion Resistant Heavy Chromium Plating, The International Journal of Surface Engineering and Coatings (1974) 19-24.

[25] E. Svenson, DuraChrome Hard Chromium Plating, Plating Resources Inc (2006).

[26] J. Parker, D. R. Gabe, M. Ward, Chromium Electroplating Solutions as Two-Phase Fluids: The Influence on Solution Conductivity, Russian Journal of Electrochemistry (2001) 677-683

[27] H. R. Moore, W. Blum, Conductivity and density of chromic acid solutions, Bureau of Standards Journal of Research (1930) 255-263.

[28] D. R. Gabe, G.D. Wilcox, The Hull Cell, The International Journal of Surface Engineering and Coatings (1993) 71-73

[29] J. W. Dini, H. A. Johnson, A. Jonas, Plating on Zircaloy-2, Sandia Laboratories (1979).

[30] F. Brossa, F. Coen, H.W. Schleicher, G. Volta, Stability and compatibility of hydrogen barriers applied to zirconium alloys, European Atomic Energy Community – EURATOM (1969).

[31] D. V. Sidelev, E. B. Kashkarov, M. S. Syrtanov, V. P. Krivobokov, Nickel-chromium (Ni–Cr) coatings deposited by magnetron sputtering for accident tolerant nuclear fuel claddings, Surface & Coatings Technology (2019) 69-78.

[32] N. Ryan, Electrodeposition of High-Purity Chromium from Electrolytes Containing Fluoride or Fluosilicate, J. Electrochem. Soc. (1960) 397-404.

[33] J. W. Dini, K. R. Johraon, Plating on Some Difficult-to-Plate Metals and Alloys, Sandia Laboratories (1980).

[34] J. Bjerrum, L. G. Sillén, A. E. Martell, Stability Constants of Metal-ion Complexes, Chemical Society (1964).

[35] D. Satas, A. A. Tracton, Coatings Technology Handbook, Marcel Dekker (2001)

[36] E.B. Kashkarov, D.V. Sidelev, M. Rombaeva, M.S. Syrtanov, G.A. Bleykher, Chromium coatings deposited by cooled and hot target magnetron sputtering for accident tolerant nuclear fuel claddings, Surface & Coatings Technology (2020) 1-9.